広島大学学位請求論文

Observational Study of Extremely Luminous Type Ia Supernova 2009dc

広島大学理学研究科物理科学専攻
山中雅之 (Yamanaka Masayuki)

平成21年1月31日

Observational Study of Extremely Luminous Type Ia Supernova 2009dc

Masayuki YAMANAKA

2011 Jan 31

A THESIS FOR THE DEGREE OF DOCTOR OF PHILOSOPHY IN PHYSICS

Department of Physical Science, Hiroshima University

ABSTRACT

In this thesis, we examined an extremely luminous Type Ia supernova (SNe Ia) SN 2009dc. Type Ia supernovae are luminous ones among whole types of supernova and they are believed to be a result of thermonuclear explosion in a white dwarf, a degenerated compact star, of which the mass reaches near the Chandrasekhar-limit-mass, about 1.4 times solar mass. Since the luminosity of Type Ia supernovae are homogeneous, they are used as a standard candle of cosmologically distant objects. In recent years, two extremely luminous Type Ia supernovae (SNe 2003fg and 2006gz) have been discovered. They pointed a discrepancy against the explosion model; $\gtrsim 1.2$ times solar mass of ^{56}Ni (energy source) and thus over 1.4 times solar mass of total ejecta should be required. However, the observational material on them was restricted and poor, and their nature was still unclear.

Here we present new observational results of the recently-discovered SN 2009dc. This supernova is also classified as an extremely luminous Type Ia supernova. From our early-phase observation, we derived a decline rate of the light curve is $\Delta m_{15}(B) = 0.65 \pm 0.03$, which is one of the slowest decline rate among those of SNe Ia. The peak V-band absolute magnitude is estimated to be $M_V = -19.90 \pm 0.15$ mag if no host extinction is assumed. It reaches $M_V = -20.19 \pm 0.19$ mag if we assume the host extinction of $A_V = 0.29$ mag. SN 2009dc clearly belongs to the extremely luminous class both in optical and near-infrared wavelengths. We estimate the ejected ^{56}Ni mass of 1.3 ± 0.3 $M_\odot$ for the no host extinction case (and of 1.8 ± 0.4 $M_\odot$ for the host extinction of $A_V = 0.29$ mag). Using an analytic model, we successfully reproduced the (quasi-) bolometric light curve until 150 days after the B-band maximum. This indicates that the peak luminosity could be explained by ^{56}Ni dacay. The C II λ6580 absorption line remains visible until a week after the B-band maximum brightness, in contrast to its early disappearance in SN 2006gz. The line velocity of Si II λ6355 is about 8000 km s^{-1} around the B-band maximum, being considerably slower than that of SN 2006gz. The velocity of the C II line is similar to or slightly less than that of the Si II line around the maximum. The presence of the carbon line suggests that thick unburned carbon and oxygen layer remains after the explosion. Spectropolarimetric study indicates that the explosion is not aspherical but rather symmetric along the line of sight. All these observational facts suggest that the amount of the ejecta is larger than that of normal SNe Ia and the progenitor's mass is over the Chandrasekhar-limit-mass.

In addition to the early-phase observation, we obtained photometric and spectroscopic data at a year after the B-band maximum. This late-phase optical photometry shows much fainter luminosity than that expected from early-phase data. A similar result has been marginally obtained for SN 2006gz. On the other hand, the observed late-phase light curve cannot be

reproduced with the model. We suggest that the late-phase luminosity decreases due to an increase of optical opacity with dust formation in the ejected material. This model is supported by the observational facts of the presence of carbon-rich ejecta in early-phase spectra and redder color index at late-phase. We also confirm the existence of [Ni II] and [Ca II] lines whose radial velocities relative to the radial velocity of the host galaxy are -600 km s^{-1} and $+300$ km s^{-1}, respectively. This indicates that a significant amount of intermediate-mass elements like calcium exists near the explosion core together with iron-group elements. All the observational facts would be explained by super-Chandrasekhar white dwarf model, except for the possible mixing in the inner core. We propose that the progenitor's mass exceeded the Chandrasekhar-limiting mass possibly due to hyper rotation of the progenitor white dwarf.

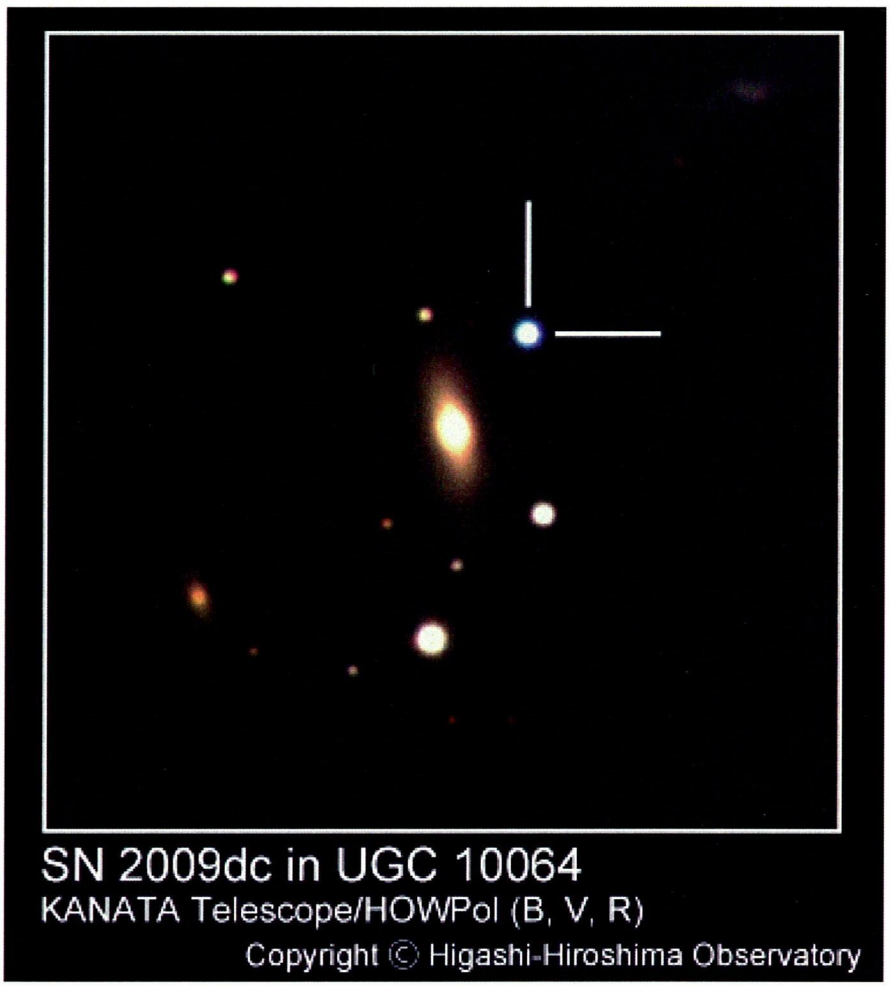
SN 2009dc in UGC 10064
KANATA Telescope/HOWPol (B, V, R)
Copyright © Higashi-Hiroshima Observatory

Contents

1 Introduction

1.1 Supernovae

1.1.1 Classification of Supernovae

Supernova explosions (SNe) is one of the most energetic astrophysical events in the universe. Their kinetic energy are calculated from the mass of ejected stellar atmosphere and its expansion velocity. If a star whose mass is ~ 1.0 $M_\odot$ expands at a velocity of 10,000 km s^{-1}, the kinetic energy of the expansion is $\approx 0.5 \times 10^{51}$ erg. This is a typical kinetic energy of SNe. Kinetic energy of some of the most powerful SNe reaches $\gtrsim 1.0 \times 10^{52}$ erg. These energetic SNe are often called as "hypernovae". Hypernova is believed to be the end of stellar evolution of a very massive star ($\gtrsim 25$ $M_\odot$).

Supernovae are classified into some groups based on the spectral features in optical wavelength (Filippenko 1997). We show sample of spectra of different types supernovae around their maximum brightness in figure 1. If the hydrogen lines are seen, it is classified as Type II SNe (SNe II). If not, it is classified as Type I. Type I SNe are further classified into Type Ia, Ib and Ic based on their spectral features. Spectra of Type Ia SN (SNe Ia) are characterized by a strong absorption of the Si II λ6355 line. This feature is usually blueshifted with respect to the systemic velocity of the host galaxy and placed around 6100 Å in the rest frame. Spectra of Type Ib SNe (SNe Ib) exhibit absorption lines, whereas those lines are not observed in the spectra of Type Ic SNe (SNe Ic). Both SNe Ia and Ic exhibit neither hydrogen absorption lines nor helium absorption lines. In this thesis, we focus on an extreme subgroup of SNe Ia (massive end of SNe Ia). We summarize the observational properties of SNe Ia in §1.2.

We show the light curves (LCs) of SNe Ia, Ic and II in figure 2. The LC of SNe Ia is similar to that of SNe Ib/c, but quite different from that of SNe II, which usually shows a long-lasting ($\gtrsim 100$ days) plateau phase. After the plateau phase, the luminosity shows a sudden decline. In contrast, SNe Ia and SNe Ib/c exhibit relatively narrow peaks (~ 30 days). After the maximum phase, SNe Ia and SNe Ib/c fade linearly in logarithmic scale (*i.e.*, exponentially in linear-scale). The decline rates of SNe Ib/c after 50 days after the maximum show relatively large variation in comparison with those of SNe Ia.

Progenitor star of Type Ia SN is widely believed to be a white dwarf in a close binary system. White dwarf has a very high density which corresponds to one solar mass for one earth size, comparing with that of a normal star. Gravitational force of a white dwarf was

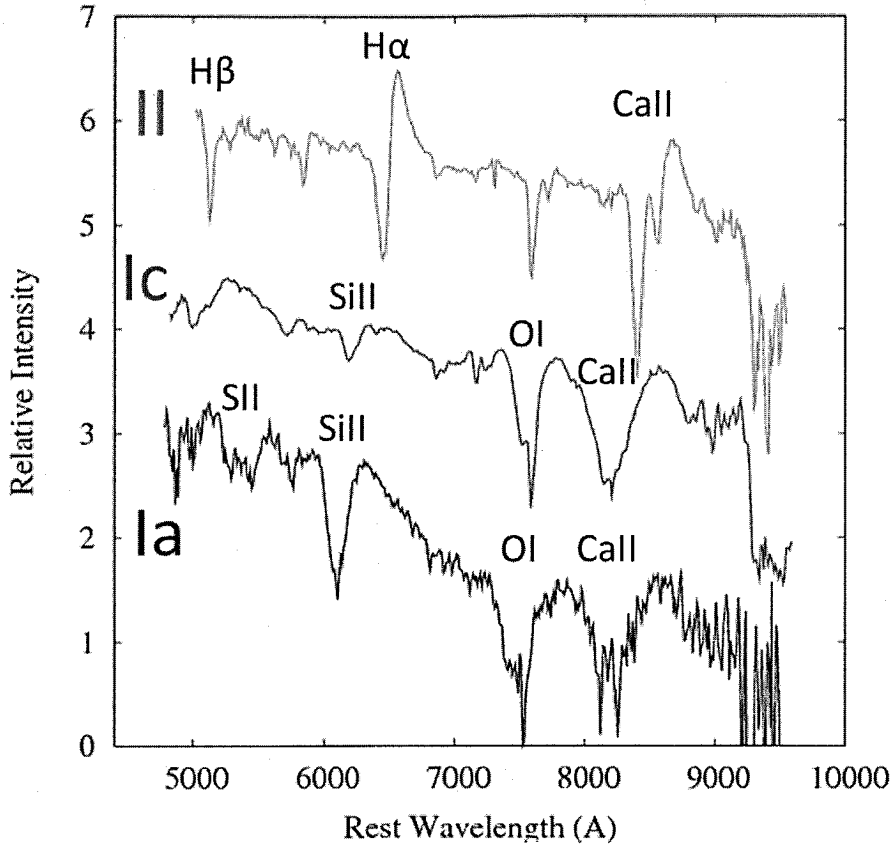

Figure 1: Typical spectra of SNe II 2008ij, Ic 2007gr and Ia 2009an around each maximum light. These spectra were obtained by 1.5-m Kanata telescope equipped with TRISPEC at Higashi-Hiroshima Observatory. The wavelength is corrected for the host galaxy recession velocity. The flux intensity is arbitrary shifted. If the hydrogen is seen, it is classified into Type II SNe (SNe II). If not, Type I. Type I SNe are divided into subtypes of Type Ia, Ib and Ic based on their spectral features. Spectrum of Type Ia SN (SN Ia) exhibits a strong absorption of Si II λ6355 line.

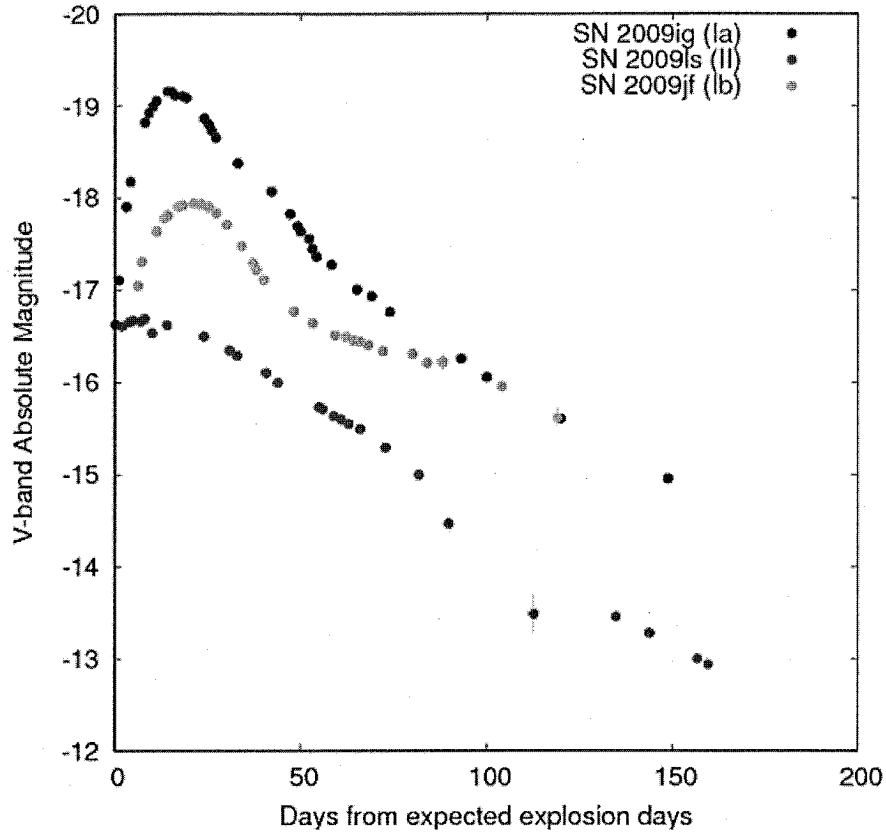

Figure 2: A V-band light curve of a typical Type Ia 2009ig compared with those of Type II and Ib SNe, denotes in blue, green and red points. These photometric data were obtained using 1.5-m Kanata telescope attached with HOWPol. For the magnitude, possible extinctions in the host galaxies host not been corrected for. These peak absolute magnitudes are roughly typical values of their types. Date of the explosion is estimated from a typical rising time of each SN.

supported by electron degenerate pressure instead of the internal pressure. If the white dwarf forms the close binary with relatively low-density secondary, the material accretes on the white dwarf. When the gravitational force become larger than force by the degenerate pressure, the white dwarf collapse and transform into neutron star or black hole. Its mass is called as "Chandrasekhar-limiting mass" (Chandrasekhar 1931). If the white dwarf does not rotate, the limiting mass is estimated to be 1.44 $M_{\odot}$ (Yoon & Langer 2003). Actually, before the mass just reach the Chandrasekhar-limiting mass, the carbon begins to ignite in the central regions and occur thermonuclear runaway. This is a SN Ia. Other types of SNe, SNe II and Ib/c, are attributed to a violent reaction to the catastrophic collapse of the ion-dominated core in an evolved massive star. We call these SNe as core-collapse supernovae (CCSNe).

The absolute magnitude of SNe Ia is relatively homogeneous. It is derived that the average absolute magnitude of SNe Ia is $M_V = 19.1$ (Folatelli et al. 2010). In contrast to SNe Ia, CCSNe show large variations in absolute magnitudes (e.g., Li et al. 2010). The distributions of the absolute magnitudes of SNe Ia and other type supernovae are shown in figure 3 (Li et al. 2010). The average magnitude of SNe Ib/c and II are roughly two magnitude fainter than that of SNe Ia.

We also show the supernova rate for various types of galaxies in figure 3. Galaxies are mainly classified into two groups based on their morphologies; elliptical (E) and spiral (S) galaxies. The elliptical galaxies are mainly comprised of old stellar population and do not contain much interstellar matter. The spiral galaxies consist of young stellar population and rich interstellar matter. SNe Ia occur in any galaxies. On the other hand, CCSNe have not been observed in elliptical galaxies (figure 3). This supports the idea that the progenitors of SNe Ia are low mass stars.

1.1.2 Luminosity Origin of Supernovae

Main source of early phase SNe radiation is the ejecta heated by interaction with gannma-ray and/or positron deposited from a chain decay of $^{56}\mathrm{Ni} \longrightarrow {}^{56}\mathrm{Co} \longrightarrow {}^{56}\mathrm{Fe}$ (Truran et al. 1967; Colgate & McKee 1969). We describe the details of the processes below. Once a supernova occurs, a large amount of radioactive material ^{56}Ni is synthesized in its explosion (Arnett 1969). The ^{56}Ni changes into ^{56}Co with emitting γ-ray photons by the following electron capture decay:

$$^{56}\mathrm{Ni} \longrightarrow {}^{56}\mathrm{Co} + \gamma + \nu_e \quad . \tag{1}$$

The emitted γ-ray energy equals to 1.75MeV against the whole decay energy of 2.14MeV (Junde et al. 1987). The remaining energy goes away in the form of neutrino emission. The decay time

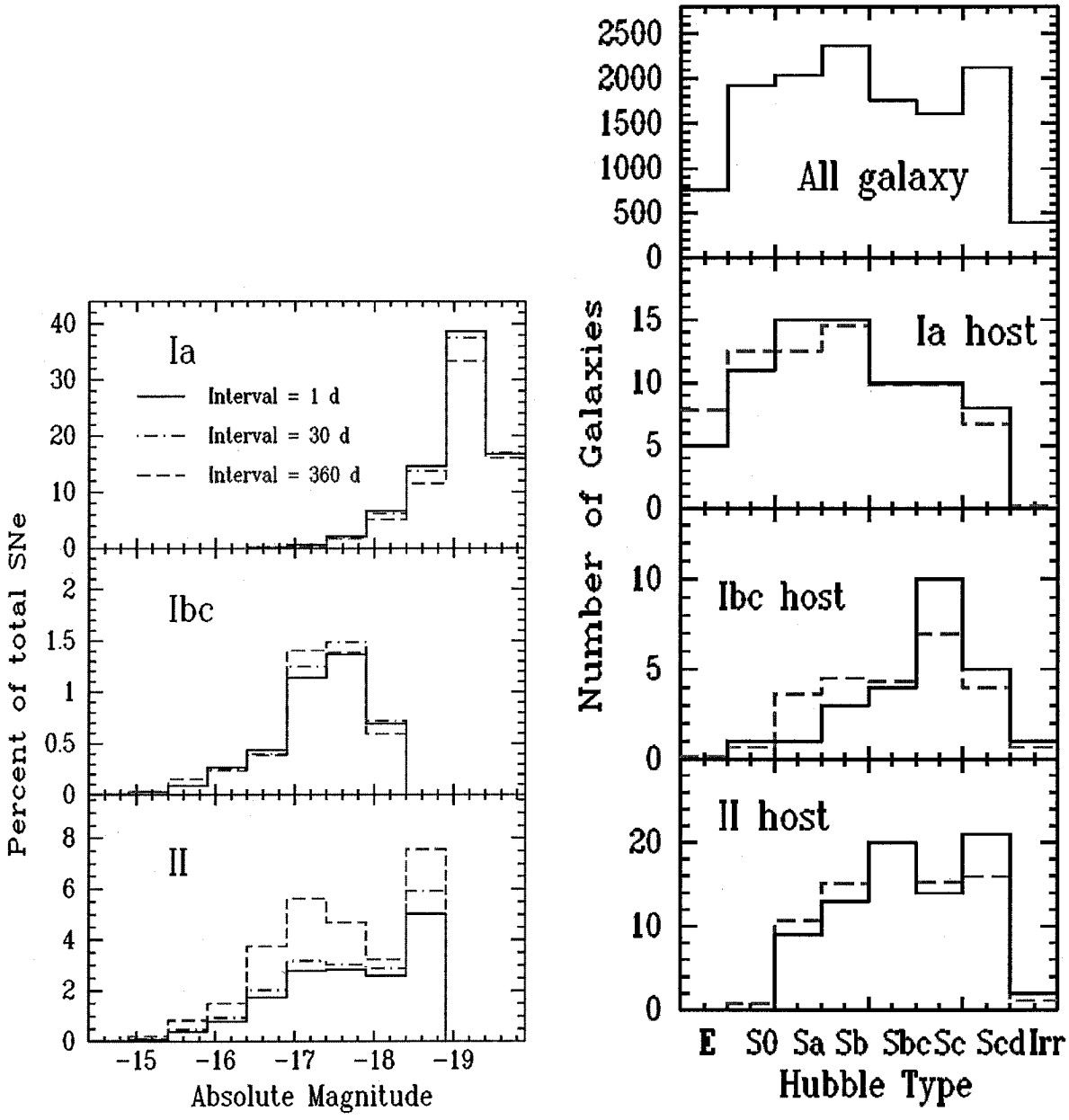

Figure 3: The left panel shows the luminosity functions of SNe Ia, Ib/c and II. The differential lines are reflected by differential surveys frequency. Fraction of the absolute magnitudes of SNe Ia peaked at ~ -19.1 mag. SNe II and Ib/c exhibit relatively large variations. The right panel shows the galaxy types for each type of SNe. SNe Ia occur in both spiral (S) and elliptical (E) galaxies; however, SNe II and Ib/c do only in spiral galaxies. Both panels are cited from Li et al. (2010)

of ^{56}Ni is 8.8 days. The emitted γ-rays are scattered by Compton scattering in the ejecta and is converted to lower energy photons. This process is the main energy source for the early phase SNe radiation. The Compton scattered photons escape from the ejecta as X-ray continuum or are absorbed by the ejecta material via the photoelectric effect. As the photosphere expands, the column density of the ejecta decreases as t^{-2}. As a result, the photospheric radiation peaked at the optical wavelength (Truran et al. 1967; Colgate & McKee 1969).

In explosion of a compact star as SNe Ia and Ib/c, the timescale of light curve around peak luminosity is derived from the ^{56}Ni decay and its diffusion timescale. Since the ^{56}Ni decay timescale is constant, the light-curve timescale depends on diffusion timescale which is a function of total ejected mass (M_{ej}), its kinetic energy (E_K) and optical depth (κ). According to Arnett (1982), we can write it as

$$\tau \propto \kappa^{1/2} M_{ej}^{3/4} E_K^{-1/4}. \tag{2}$$

Assuming that the optical depth is almost constant (Arnett 1982), the diffusion timescale depends on the total ejected mass and the kinetic energy of the ejecta. A simple model successfully reproduces the light curves of typical SNe Ia and a considerable part of SNe Ib/c and some of SNe Ibc (Arnett 1982). Fitting the analytic light curves to observational ones, we can estimate the ^{56}Ni mass, the ejected mass and kinetic energy.

Next, ^{56}Co transform into a stable isotope ^{56}Fe via electron capture decay (81%) or positron decay (β^+) (19 %) as

$$^{56}\mathrm{Co} \longrightarrow \begin{cases} ^{56}\mathrm{Fe} + \gamma + \nu_e & , \\ ^{56}\mathrm{Fe} + e^+ + \gamma + \nu_e & . \end{cases} \tag{3}$$

The decay timescale of ^{56}Co is 111 days. The positrons interact with the ejected matter and lose their kinetic energy. Annihilating with the electron produces the 0.511MeV γ-ray photon. Production rate of this γ-ray is 38% versus whole ^{56}Co decay. Combined with the γ-ray photon in electron capture decay, the total emitted energy of γ-ray photon is estimated to be 3.61MeV (Junde et al. 1987). However, the mean free path of the γ-rays increase as the ejecta expands. Then the ejecta becomes optically thin and and transparent to the γ-ray photon at this phase (a few months after the explosion date). Instead of the γ-ray, the kinetic energy of the positrons becomes dominant for the radiation energy source at this phase. Its total energy is estimated to be 0.12MeV by Junde et al. (1987). If the positron energy is completely converted to radiation, the decline rate of the bolometric magnitude equals to +0.98 mag per 100 days (e.g., Cappellaro et al. 1997). Late-phase luminosity is thus a good indicator of the produced ^{56}Ni mass, complementary to the peak luminosity.

1.2 Type Ia Supernovae

SNe Ia is widely believed to occur when a white dwarf reaches near the Chandrasekhar-limiting mass due to accretion from its companion star, e.g., red giant or main sequence (Whelan & Iben 1973). Since SNe Ia is a main source of iron group elements, it strongly affects the galactic chemical evolution (Pagel 1997). SNe Ia is also used as a strong tool for investigating cosmological parameters due to their good homogeneity of luminosity (Perlmutter et al. 1999; Riess et al. 1998). SNe Ia are used as a good distance indicator, because we can know the absolute luminosity from only their decline rates (Phillips 1993).

SNe Ia are generally divided into three subclasses, normal, luminous and faint ones. The majority of SNe Ia belong to the normal subclass. Although the spectral features are well correlated with the luminosity, the line velocity (which is measured from the Doppler shift and/or broadening of emission lines and indicates the expansion velocity of the line-forming gas) does not depend on the luminosity (Benetti et al. 2005). This indicates that the SNe Ia would have a diversity in progenitors, its circumstellar materials and explosion mechanisms (Mazzali et al. 2007). Thus, the diversity is a important key factor for understanding the basic physics of SNe Ia. The luminous and faint subclasses are relatively small classes. However, their observational properties are basically consistent with the normal SNe Ia, and these subclasses also give us not a little impact in SNe research.

In the following subsection, we also present some results of recent theoretical studies on progenitors and explosion mechanisms of SNe Ia. It is useful for interpreting the observational properties of the main target of this thesis, SN 2009dc.

1.2.1 As a Distance Indicator

Phillips (1993) found the correlation between the decline rate ($\Delta m_{15}(B)$: the difference between the B-band maximum and 15 days after the maximum.) of the light curve and the absolute magnitude of SNe Ia. This is sometimes called as "width-luminosity relation" or "Phillips law". Its calibration method has been developed in this decade and the accuracy of estimation has been rather modified (Phillips et al. 1999; Altavilla et al. 2004; Reindl et al. 2005; Prieto et al. 2006; Jha et al. 2007; Folatelli et al. 2010). We show the width-luminosity relation in figure 4 from Folatelli et al. (2010). The more luminous SN Ia has the more slower decline rate. Thanks to this tight correlation, we can estimate the distance to a SNe Ia by observing its light curve variation (see Appendix A.1; Freedman et al. 2001).

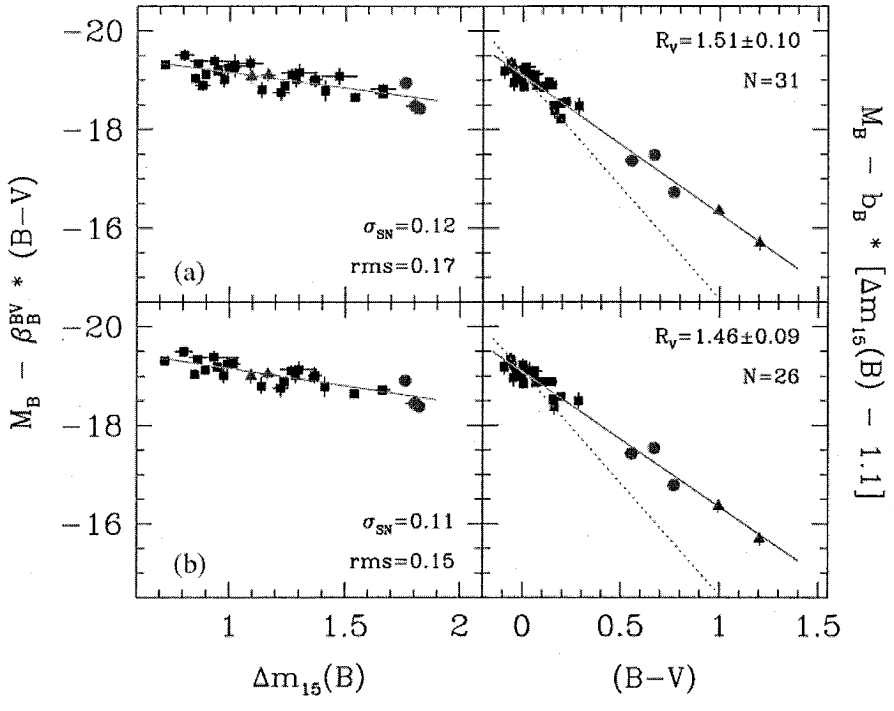

Figure 4: The correlation of M_V with $\Delta m_{15}(B)$, which is difference between the maximum light and 15 days after maximum (in left panels) or $B - V$ (in right panels) in the whole samples (in upper panels) and selected good samples (in lower panels), cited from Folatelli et al. (2010). More luminous objects have slower decline rate and bluer color. Red circles denote fast-expanding SNe Ia and red triangles denote very red SNe Ia 2005A and 2006X. In right panels. the dashed lines mean that the dust extinction coefficient adopt of $R_V = 3.1$ (Cardelli et al. 1989). This indicates that the R_V in SNe Ia extinction should be lower than a typical Galactic value.

1.2.2 Observational Characteristics of SNe Ia

In this section we explain the observational characteristics of SNe Ia.

The peak absolute luminosity and the various spectral features of SNe Ia are correlated with each other (figure 5). A spectrum of a typical Type Ia SN (e.g., $\Delta m_{15}(B)$= 1.32 and $M_V = -19.1$ mag for typical SN 1994D; Patat et al. 1996) exhibits Si II λ6355, S II W-shape features, Fe II multiplet and Ca II IR triplet absorption lines (Branch et al. 1993). Filippenko et al. (1992a,b) performed the spectroscopic observations of two peculiar Type Ia events SNe 1991T and 1991bg, respectively. The former shows higher peak luminosity ($M_V = -19.5$ mag) and slower decline rate of the light curves ($\Delta m_{15}(B)$= 0.99). Its spectrum exhibits very shallow Si II λ6355 and Si II λ5972 absorption lines. Relatively high excitation lines such as Fe III are strong in its spectrum (Branch et al. 2006). The latter shows much lower peak luminosity ($M_V = -16.9$ mag), very fast decline rate ($\Delta m_{15}(B)$= 1.93) and very red color. Its spectrum exhibits asymmetrical absorption of Si II λ6355 and relatively deep Si II λ5972 absorption line. Its spectra also show the Ti II absorption lines (Filippenko et al. 1992b). Branch et al. (1993) investigate many SNe Ia and divided then into three subclasses, which are classified into three groups, which are SN 1991T-like, SN 1991bg-like and normal Type Ia SNe. Li et al. (2001) examine the fraction of these subclasses. They found that their percentages are 20 %, 16 % and 64 % for 91T-like, 91bg-like and normal events, respectively.

The luminosity is well correlated with the line depth ratio of Si II λ5972 to Si II λ6355 (R(Si II); Nugent et al. 1995). The more luminous object shows the lower R(Si II) value. Hachinger et al. (2006) investigate the ratio of the equivalent widths (EWs) of several absorption lines. They found a good correlation between the ratio of EWs of Si IIλ5972 to Si IIλ6355 and $\Delta m_{15}(B)$ (figure 6). In general, SNe Ia with higher luminosity (lower R(Si II) have bluer color (Phillips et al. 1999), which is reproduced by higher photospheric temperature (Nugent et al. 1995). This suggests that these ratios should be a photospheric temperature indicator independently of the color index (Bongard et al. 2006; Blondin et al. 2006).

In this decade, more extensive early-phase photometric and spectroscopic observations of individual SNe Ia have been extensively performed (Patat et al. 1996; Salvo et al. 2001; Benetti et al. 2004; Anupama et al. 2005; Elias-Rosa et al. 2006; Stanishev et al. 2007; Krisciunas et al. 2007; Pastorello et al. 2007; Pignata et al. 2008; Wang et al. 2008, 2009; Yamanaka et al. 2009b, and therein.). With these large samples, the diversity of the line velocities of Si II has been suggested (Hatano et al. 2000). Benetti et al. (2005) collected these well-observed samples and attempted to classify them based on the line velocity, R(Si II) variation and $\Delta m_{15}(B)$ via cluster analysis. As a result, they discovered three groups, which are HVG (High Velocity Gradient),

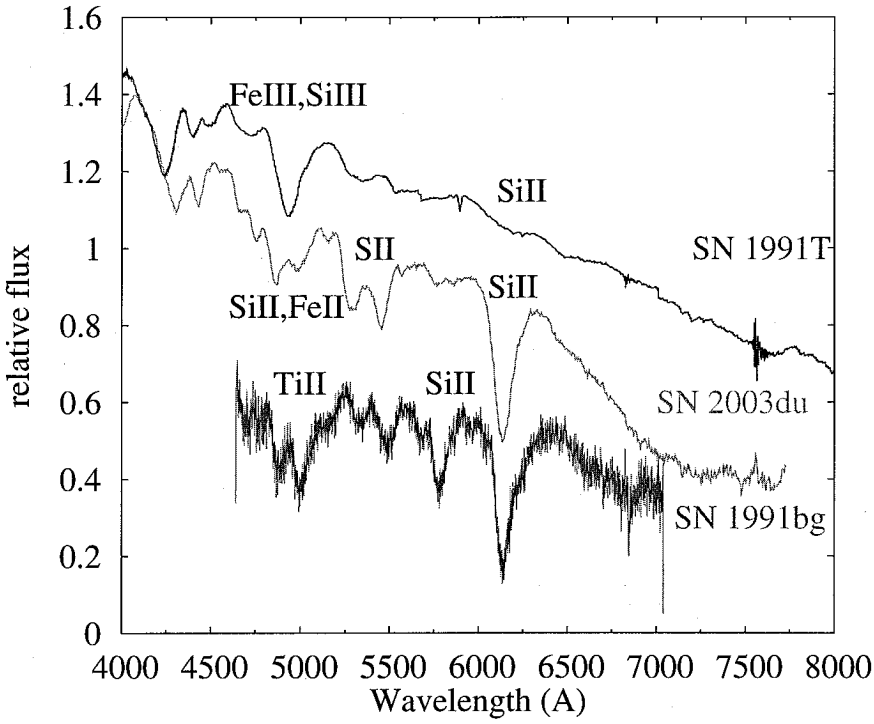

Figure 5: Spectra of luminous Type Ia SN 1991T (Filippenko et al. 1992a), normal Type Ia SN 2003du (Stanishev et al. 2007) and subluminous Type Ia SN 1991bg (Filippenko et al. 1992b). The wavelengths are calibrated to rest frame using the recession velocity of the host galaxy.

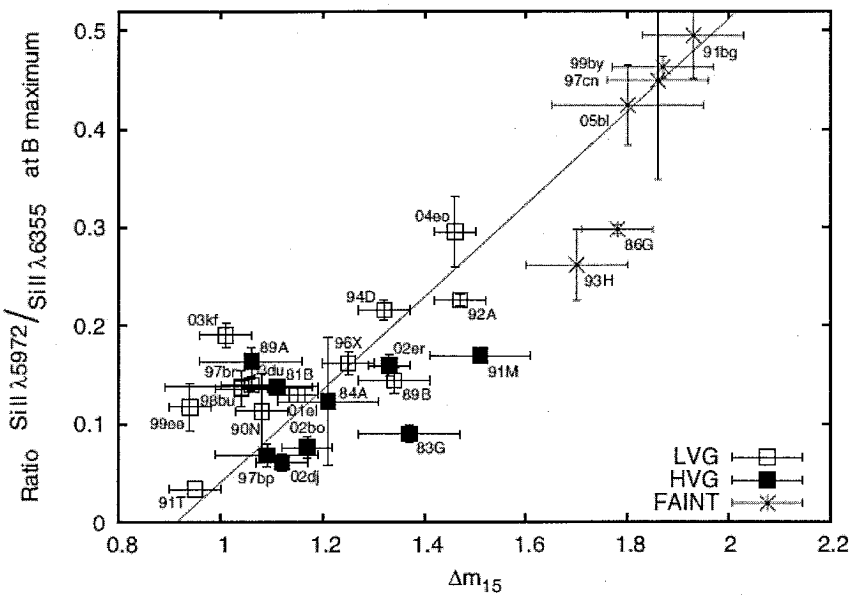

Figure 6: The ratio of equivalent width Si IIλ5972 to Si IIλ6355, R(Si II are plotted versus $\Delta m_{15}(B)$ (Hachinger et al. 2006). There is a good correlation between these two paremeters. More luminous object shows smaller R(Si II) even including the 91bg-like events.

LVG (Low Velocity Grandient) and Faint object. HVG SNe exhibit the very high velocity ($\gtrsim$ 15000km s^{-1}) of line absorption, and the large decline rate of the line velocity and R(Si II) before maximum date. LVG SNe do the relatively low velocity ($\sim$ 12000 km s^{-1}), and low decline rate of the line velocity and almost non-variation of R(Si II). Faint objects do the very slow line velocity ($\sim$ 8000 km s^{-1}) at maximum, and the large decline rate of the line velocity and large R(Si II) value until maximum. Faint objects correspond approximately to SN 1991bg-like objects (Filippenko et al. 1992b; Branch et al. 1993). Interestingly, HVG and LVG SNe include both normal and 91T-like SNe Ia. This fact indicates that the expanding-velocity of SNe Ia is independent on its luminosity and the decline rate of the light curve. Such a diversity might reflect a variety of parameters in explosion models (Mazzali et al. 2007). Alternatively, high-velocity features might be produced by interactions of ejecta with circumstellar material (CSM) (Gerardy et al. 2004; Tanaka et al. 2006).

After a half year from the explosion, the spectra of SNe Ia show nebular emission lines. As ejecta of a SN expands with time, the atmosphere gradually becomes optically-thin. In this phase, the emission lines which are emitted from iron group elements are conspicuous in the SNe Ia spectra (ex.SN 1981B; Branch et al. 1983). The more luminous SNe Ia show the stronger

[Fe II], [Fe III] emission lines (Mazzali et al. 1998). Spectroscopy of another SC SN 2006gz shows only relatively weak or absent [Fe II], [Fe III] emission lines, which is rather similar to the property of faint SNe Ia (Maeda et al. 2009).

1.2.3 Peculiar SNe Ia

Recently, some SNe Ia which show peculiar spectral features have been discovered. SN 2002cx and its subclass are clearly not followed by the width-luminosity relation (Li et al. 2003; Phillips et al. 2007; Sahu et al. 2008; Valenti et al. 2009; Foley et al. 2009, 2010). These objects commonly exhibit much fainter peak luminosity estimated by the width-luminosity relation. Their pre-maximum spectra exhibit highly-excited absorption lines, whose profiles are similar to those of SN 1991T-like SNe. However, their post-maximum spectra exhibit narrow absorption lines similar to those of SN 1991bg-like SNe. On the other hand, the line velocities are much lower ($\lesssim$ 5000 km s^{-1}) than those of SN 1991bg-like SNe, indicating that these objects (SN 2002cx-like SNe) have lower kinetic energy than that of typical SNe Ia (Foley et al. 2009). In these objects, detonations might not occur in outer region because of incomplete deflagration in progenitor white dwarf. If this is the case, the ^{56}Ni mass produced by the deflagration would be small and the peak luminosity of the SNe would be faint. However, this incomplete deflagration model cannot explain the observational fact that absorption lines of carbon, which is an ember element of nuclear deflagration, are not seen in the spectra of SN 2002cs-like SNe.

SN 2002ic is other peculiar object and the observations of this object have given us a very important clue for identifying progenitors of SNe Ia. It had been classified as a normal SN Ia from its early-phase observation. However, in the later phase, its spectrum exhibited narrow ($\sim$500 km s^{-1}) and broad ($\sim$2000 km s^{-1}) emission lines of hydrogen Balmer series. The profiles of these emission lines are typical ones of the emission line spectra of SNe Ia. Hydrogen emission lines are widely seen in the spectra of Type II SN: core-collapse explosion of massive star. The existence of the hydrogen emission lines is a strong evidence that the progenitor is surrounded by self-ejected dense wind (e.g., hydrogen envelope) when the progenitor explodes. It strongly supports that the progenitor could be a single degenerate object, which is composed of a white dwarf and accretion material from the secondary star. In single-degenerate scenario, the secondary star blows hydrogen-dominated wind into the circumstellar space. This is consistent with the observations. However, it is still unknown how dominant single degenerate objects are in SNe Ia progenitors, because SN 2002ic-like objects are statistically very rare.

It strongly supports that the progenitor could be a single degenerate object, which is composed of a white dwarf and accretion material from the secondary star. In single-degenerate

scenario, the secondary star gives off hydrogen-dominated wind into the circumstellar field. This is consistent with the observations. However, it is a problematic material that SN 2002ic-like objects are statistically very rare.

1.2.4 Explosion models

In this section, we describe the historical developments of theoretical models of SN explosion mechanisms. Recent studies have suggested that multi-dimensional delayed detonation models successfully reproduce the observational characteristics — the color index, luminosity, and light curve — of SNe Ia. The delayed detonation models are constructed as a combination of nuclear deflagration of white dwarf and later detonation. The detonation occurs when the deflagration burning front reaches to the outer layer where density is sufficiently low. We here present the basic scheme of the multi-dimensional delayed detonation model (see Hillebrandt & Niemeyer 2000).

Type Ia SNe synthesize much larger ^{56}Ni mass ($0.6M_{\odot}$ in typical) than core collapse SNe. In order to reproduce such large ^{56}Ni mass, a thermonuclear explosion in a degenerate star (white dwarf) is required. Arnett (1969) constructs a simple detonation explosion model in which the burning front is assumed to propagate in a supersonic speed. Because the detonation instantly drives the explosive synthesis of whole white dwarf materials into iron group elements until it propagates to outermost region, this model fails to produce an expanding photosphere. As a result, SNe Ia cannot be exploded by this model. It also makes too much ^{56}Ni to fit the observed light curve and spectral line features of intermediate mass elements (IMEs) such as Si, Ca and S.

A deflagration model successfully reproduce the most parts of observational features of SNe Ia (Nomoto et al. 1984). In a standard deflagration model, the ignition propagates in a subsonic speed in white dwarf materials. This model realizes that the ejecta expands during the propagation of burning front. However, some of observational results are not explained only by deflagration. For example, high-velocity features seen in HVG SNe or in outer atmosphere of normal SNe Ia cannot be reproduced by this model (Mazzali et al. 2005b,a; Tanaka et al. 2006). Relatively large ^{56}Ni mass (expected in luminous subclasses) also cannot be synthesized. In order to produce the large ^{56}Ni mass and the highly-expanding velocity, it is necessary that a detonation wave become supersonic in some points. Recently developed two- or three-dimensions deflagration models leave large amounts of unburnt materials as carbon and oxygen. However, no carbon feature is typically seen in spectra of normal, 91T-like and even 91bg-like Type Ia SNe (except for SN 2006D; Thomas et al. 2007).

Recent studies of hydrodynamic and radiative transfer models successfully reproduce the large ^{56}Ni and IMEs masses and high-velocity features based on delayed detonation. In these models, a detonation explosion occurs when the burning front driven by deflagration reaches a critical density (Khokhlov 1991). The deflagration synthesizes large amount of ^{56}Ni and accelerates the ejecta to high speed in outer region. It also produces much IMEs. These can reproduce the early-phase spectra of SNe Ia, indicating the structures in outer region. Alternatively, in inner-regions, these models also predict electron-capture synthesized elements such as ^{58}Fe and hole structure of IMEs elements. IMEs features are seen as flat calcium lines in late-phase near-infrared spectra (Motohara et al. 2006; Leloudas et al. 2009).

The mixing rate of the materials in ejecta is dependent on the relative intensity of deflagration burning. The stronger deflagration predicts the stronger mixing in the ejecta (Bravo & García-Senz 2008). If the mixing is strong, the light elements like Si, Ca and S could distribute in inner-part ejecta. This is not consistent with the hole-like structure expected from flat calcium lines. If the detonation wave is stronger, the ejecta would become rather stratified strcuture (Maeda et al. 2010c).

Currently, the above models — the multi-dimensional delayed detonation models — are widely accepted as suitable models of explosion mechanism of SNe Ia. Note that there is a common assumption in these models. The assumption is that the mass of progenitor white dwarf is almost equal to (or slightly less than) the Chandrasekhar-limiting mass ($\approx$ 1.4 $M_{\odot}$.) Here we call these SNe Ia "Chandrasekhar-limiting mass SNe Ia".

1.2.5 Progenitor System Candidates

White dwarf in close binary systems are widely believed as progenitor systems of SNe Ia. The following three kinds of systems have been proposed for SNe Ia progenitors. (1) Single degenerate (SD) system. It is a close binary system which is comprised of a white dwarf and a red giant or main sequence star whose surface layer is accreting on to the surface of the white dwarf (Whelan & Iben 1973). (2) Double degenerate (DD) system. It is a white dwarf - white dwarf binary system and the two white dwarfs merge and explode (Webbink 1984; Iben & Tutukov 1984). (3) Sub-Chandrasekhar-limiting mass system. The configuration of this system is the same as (1), but thick helium layer is built up on the surface of the primary white dwarf (Woosley & Weaver 1986).

In the single degenerate scenario, the primary white dwarf gradually becomes massive by mass accretion from the companion star. Its accretion rate is estimated to be from 10^{-7} to 10^{-8} $M_{\odot}$ yr^{-1} in numerical calculations of a binary system (Nomoto 1982). After the mass

of the white dwarf exceeds some mass threshold, the binary system enters in the supersoft X-ray (SSXS) phase in which steady hydrogen burning occurs on the white dwarf surface (van den Heuvel et al. 1992). The total number of SSXS is estimated to be an order of 1000 per galaxy. Recent X-ray observations suggest that the upper-limit of supersoft X-ray luminosity of extragalaxies is lower than that expected from the SSXS phase of white dwarfs (Gilfanov & Bogdán 2010). However, Hachisu et al. (2010) illustrated that optically thick wind from the SSCS phase white dwarf can prevent us from observing the object in supersoft X-ray band. One of the strong points of single degenerate scenario is that recent three-dimensional explosion models with Chandrasekhar-limiting mass white dwarf successfully reproduce the observational width-luminosity relation (Kasen et al. 2009).

In the double degenerate scenario, a less massive WD is disrupted by tidal force by the mass of more massive primary WD (Benz et al. 1990). Non-explosive burning occur on the surface of the WD. It convects onto surface of O-Ne (oxygen and neon) material. This results in the rather accretion-induced collapse evolving to a black hole or a neutron stars rather than explosions as SNe Ia (Saio & Nomoto 1985). The simulation of merger model for double WDs is calculated in equal masses of $0.9M_{\odot}$ (Pakmor et al. 2010). This model successfully reproduce the observational light curves and spectrum of rather faint SN 1991bg-like object, though more luminous SNe Ia occur in rare.

In sub-Chandrasekhar scenarios, a primary WD forms a helium layer by accreting from the helium rich donor or hydrogen burning to helium. When the layer reach a critical density, a detonation occur and the burning front propagates into the central region of WD. This drives secondary detonation, which does not synthesize iron-peak elements of the entire star because the white dwarf has relatively lower density. The strong point of sub-Chandrasekhar model is that it does not need the artificial transition of deflagration to detonation. The progenitor mass would fall in a narrow range of 0.9-1.1 $M_{\odot}$ in order to reproduce the iron-peak elements.

In this thesis, we focus on the super-Chandrasekhar-limiting mass SNe Ia, whose progenitors are possibly speculate to be a rapidly-rotating WD with single degenerate or merger of double WDs due to its large total ejected mass.

1.2.6 Super-Chandrasekhar-limiting Mass SNe Ia and SN 2009dc

Recently, two extremely luminous SNe Ia, 2003fg and 2006gz, have been discovered (Howell et al. 2006; Hicken et al. 2007). Their absolute maximum magnitudes are $M_V = -19.94 \pm 0.06$ mag for SN 2003fg and -19.74 ± 0.16 mag for SN 2006gz. Both SNe show very slow luminosity

evolution. These high peak luminosities indicate the very high mass of ^{56}Ni. These two SNe commonly show carbon absorption lines, which are unseen in the spectra of normal SNe Ia.

The extreme brightness and the presence of carbon in ejecta suggests that their progenitors' masses exceeded the Chandrasekhar limiting mass if the progenitors were not rapidly rotating ("super-Chandrasekhar mass WD; SC WD"). This type of SNe has been called as "super-Chandrasekhar mass type Ia supernova explosions" (hereafter we referred as to "SC SNe Ia"). However, it is very unclear how progenitors evolve to super-Chandrasekhar mass WD. Its explosion models are also need to develop to explain their extremely high luminosities and carbon features seen in spectra.

For SN 2006gz, late-phase spectroscopy was performed using 8.2m Subaru telescope attached with FOCAS at 338 days after the B-band maximum (Maeda et al. 2009). This spectrum exhibits much weaker emission lines of [Fe II] and Fe III] among 4000-5500 Å than that of normal SNe Ia in similar phase. It indicates that the spectra of SC SNe Ia resemble that of a subluminous Type Ia SN, i.e a SN 1991bg-like event. In addition, the visual magnitude of this SNe at around 300 days after the maximum was much lower than the value expected from its early-phase light curve, and was even lower than that of normal SNe Ia. These observational results suggest a low ^{56}Ni mass for SN 2006gz. It contradicts the very high ^{56}Ni mass derived from the early-phase observations. It is thus still quite controversial whether SC SNe Ia including SN 2006gz really have super-Chandrasekhar-limiting mass ejecta.

Another SC SNe Ia candidates, SN 2009dc was discovered on 2009 Apr 9.31 UT (-16.7 days after the B-band maximum; see §3.1) at non-filter magnitude of 16.5 mag near the outer edge of an S0 galaxy UGC 10064 (Puckett et al. 2009), $\mu = 34.88 \pm 0.15$ from the NED database (Falco et al. 1999). A follow-up observation on Apr 16.22 (-9.7 days) revealed spectroscopic similarity with SN 2006gz before the B-band maximum, including the existence of conspicuous C II features (Harutyunyan et al. 2009). The expansion velocity deduced from the Si II λ6355 line is about 8700 km s $^{-1}$ at -9.7 days (Harutyunyan et al. 2009), which is slower than that of SN 2006gz (Hicken et al. 2007), but comparable to that of SN 2003fg (Howell et al. 2006).

1.3 Goal of this thesis

In this thesis, we show our photometric and spectroscopic observations of this latest SC SNe Ia candidate SN 2009dc from -8.1 days to $+383.4$ days after the B-band maximum. Because the observational samples of SC SNe Ia are still very poor and the past candidates are rather faint (i.e., appeared in somewhat distant galaxies), our data of SN 2009dc would be the best observed sample among those of SC SNe Ia. We derive the maximum bolometric luminosity, which is

comparable to or larger than those of SN 2003fg and SN 2006gz. The luminosity requires that the mass of the heating source, ^{56}Ni, is comparable to or even exceeding the Chandrasekhar mass (of non-rotating white dwarf), thus suggesting that it is a SC SN Ia. Such a result gives a large impact in modern astronomy since the presence of SC SNe Ia could be a risk in using as the distance indicator. We also present some peculiar properties of SN 2009dc compared with other SC SNe Ia candidates. This result has already been published as the first paper (Yamanaka et al. 2009a).

After the publication of our first paper, we performed late-phase observations of SN 2009dc, which allows us to study the peculiarity of inner-region of SC SNe Ia. We find the discrepancy between the late-phase luminosity and that expected from the early-phase observations. We will present that the discrepancy could be explained by very large ^{56}Ni mass and dust formation. We discuss the physics of the SC SNe Ia by comparing the observational results with recent hydrodynamical explosion models. We also discuss the ejecta structure and distributions of the materials. Finally, we finally conclude that the peculiarity seen in SN 2009dc would be consistently explained by super-Chandrasekhar white dwarf.

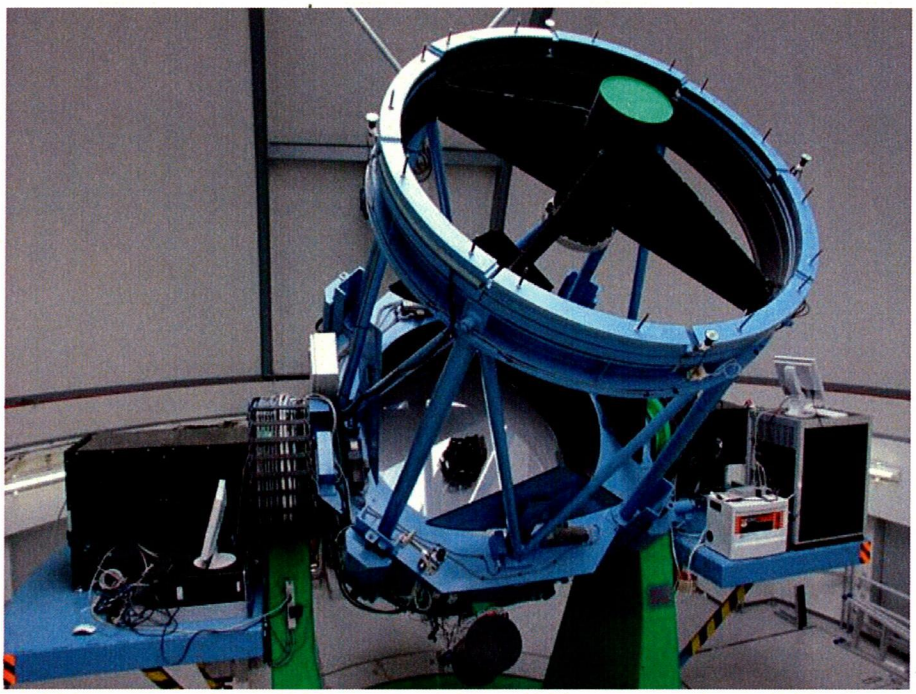

Figure 7: 1.5-m Kanata telescope

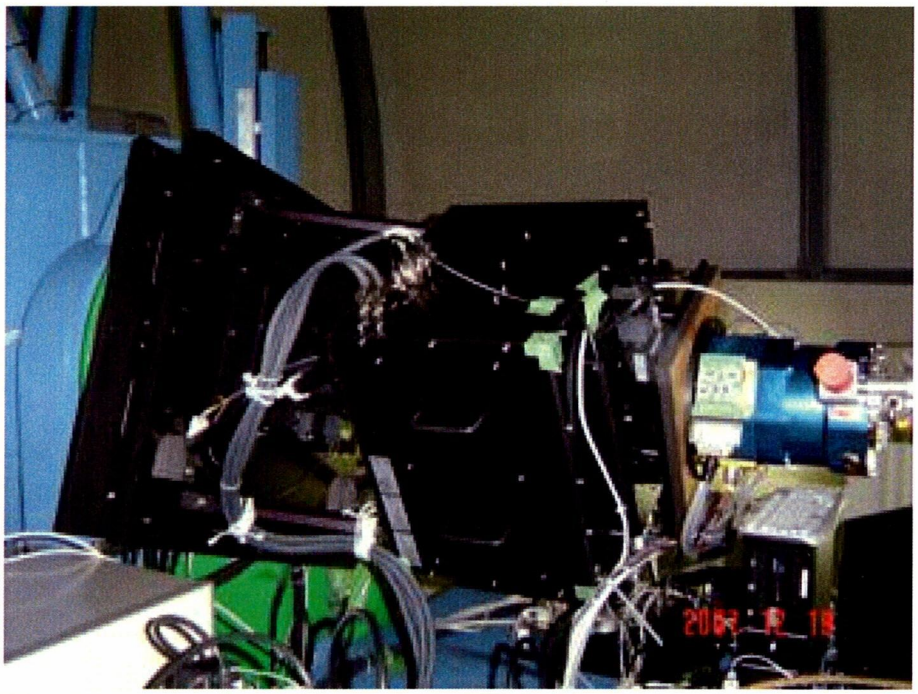

Figure 8: HOWPol

2 Observations

2.1 Telescopes and Instruments Used

We performed photometric and spectroscopic observations of SN 2009dc in optical and near-infrared regions. These extensive observations are successfully performed thanks to using six various telescopes and instruments. we briefly describe each observational instruments below.

2.1.1 Higashi-Hiroshima Astronomical Observatory

Higashi-Hiroshima Astronomical Observatory (HHAO) is located at Higashi- Hiroshima, Hiroshima. The scientific observations started using 1.5m "Kanata" telescope in Oct. in 2006 (figure 7). The main scientific aim of this observatory is investigation of various transient astronomical objects with flexible and dynamic observation in optical and near-infrared wavelengths (Uemura et al. 2007). In particular, multi-wavelength observations in collaboration with *Fermi* γ-ray space telescope are being conducted intensively for γ-ray transients like blazars, X-ray binaries and gamma ray bursts (GRBs). For investigating SNe, systematic multi-band photometric and spectroscopic observations have been performed since 2008. The fraction of clear night is about a 60%. The average seeing size is estimated to be 1.2" $\pm$0.2 (Chiyonobu 2004).

2.1.2 1.5m-Kanata telescope

Kanata telescope is a Ritchey-Chretien reflecting telescope. The effective diameter of the primary mirror is 1.54m. The telescope can rapidly move with speeds of 5 degs s^{-1} and 2 degs s^{-1} around the azimuth axis and elevation axis, respectively. It is much more rapid comparing to similar sized telescopes.

Kanata telescope is equipped with three unique instruments, "TRISPEC"[1], "HIgh-Speed Camera"[2], and "HOWPol". We mainly used HOWPol (figure 8) as an optical imager for observations of SN 2009dc. The specifications of HOWPol are described in the next section.

[1]TRISPEC is an optical and near-infrared three color camera and spectrograph. This instrument was developed by the Z-laboratory of Nagoya University. We can choose four observational modes, imaging, spectroscopy, polarimetry and spectropolarimetry.

[2]"HIgh-Speed Camera" was developed by Kyoto University. It has capabilities of very high speed imaging and spectroscopy. Minimum exposure time of the camera is 0.03 second.

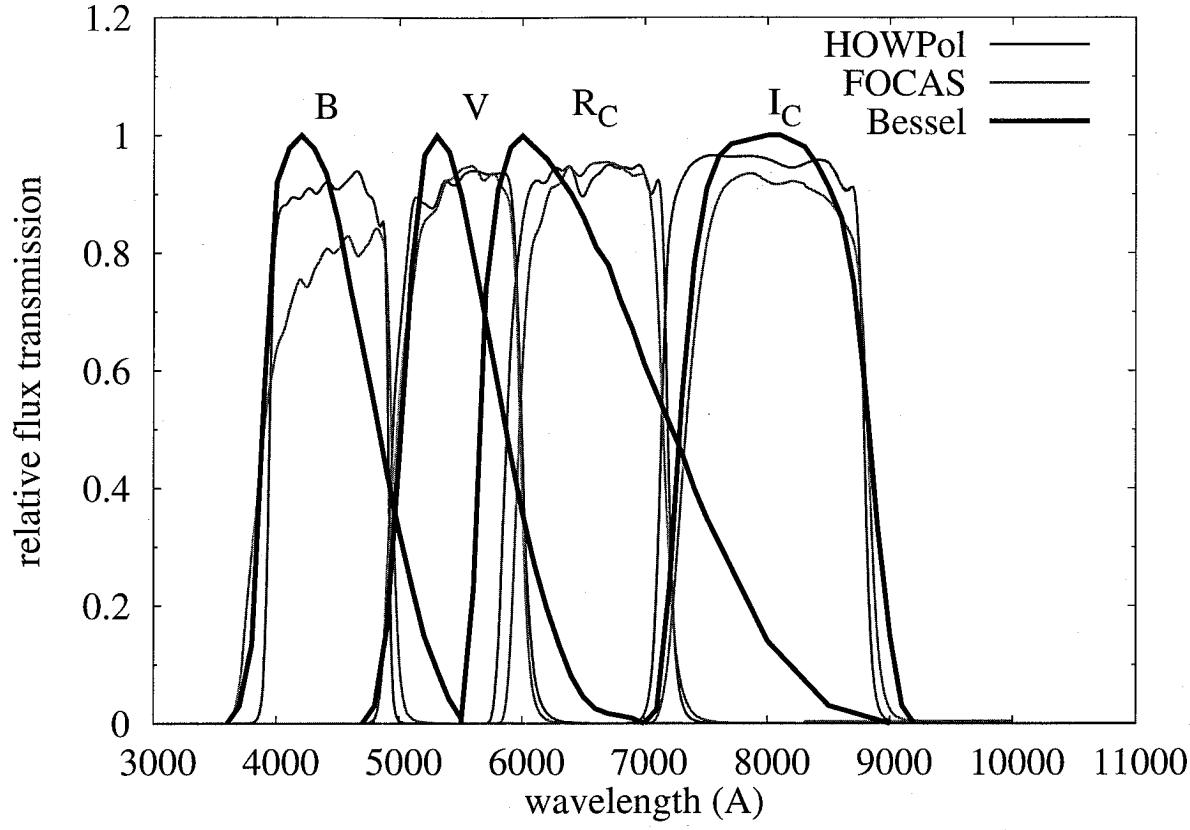

Figure 9: Filter passbands of B,V,R_C and I_C-bands for HOWPol and FOCAS.

2.1.3 HOWPol

"HOWPol (Hiroshima One-shot Wide-field Polarimeter; Kawabata et al. 2008)" has four observational modes, imaging, spectroscopy, narrow and wide field imaging polarimetry. HOWPol has two 2048 $\times$ 4096 CCDs with a pixel size of 15 μm. The CCD is a full depletion type one which was developed by Hamamatsu Photonics, Co.. The pixel scale and the field of view of HOWPol are 0.3" and 15', respectively, when attached to Kanata telescope.

The field of view of HOWPol is a circle whose diameter is 15'. We can select one filter from B, V, R_C, I_C, $z' + Y$-bands. B, V, R_C, I_C filters are designed based on Johnson-Kron/Cousin system (Bessell 1990). The transmission curves of these filters are shown in figure 9. The 3σ limiting magnitude for 300 sec exposure is estimated to be $\sim$20 mag in R_C-band. This high performance allows us to make photometric monitoring of bright SNe whose peak R_C band magnitudes are 16-17 mag for more than a month [3].

[3]The recent preliminary photometric results of novae, supernovae, dwarf novae, X-ray binaries, blazars and so

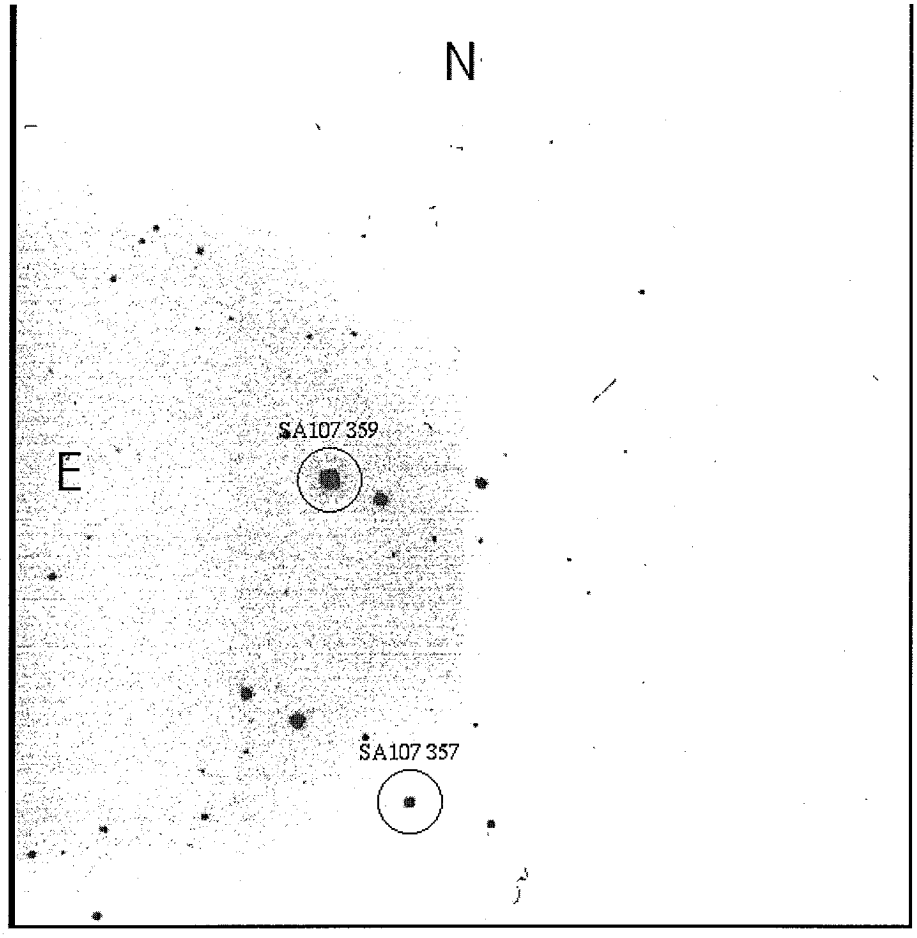

Figure 10: Finding chart of photometric standard star SA107 obtained by HOWPol.

2.1.4 1.5-m telescope at Gunma Astronomical Observatory

Gunma Astronomical Observatory (GAO) is designed for both astronomical research and public use, established in April 1999 by Gunma prefecture. The scientific observations have been started using 1.5m reflector since 2000 (figure 11). This telescope was constructed based on the design of the Infrared Simulator in the Mitaka campus of National Astronomical Observatory (it is the previous incarnation of Kanata telescope). This telescope is equipped with three instruments, which are near-infrared camera "GIRCS", Echelle spectrograph "GAOES" and low resolutions spectrograph "GLOWS".

2.1.5 GLOWS

GLOWS (Gunma LOW resolution Spectroscopy) is used for immediate optical imaging and spectroscopy of the optical transients, like novae, SNe and GRBs (e.g.; Early-phase spectroscopy of highly energetic Type Ic SN 2002ap; Kinugasa et al. 2002). This instrument is installed to the Bent Cassegrain positions of the 1.5-m telescope. The CCDs of GLOWS have a pixel scale of 0.6" pix and a field of view of 10' in the optics of 1.5m telescope. Its CCD is be refrigerated for a flexible observations at any time. We used this instrument for low resolutions spectroscopy of SN 2009dc. For spectroscopy, the slit-width equals to 1.8", corresponding to 3 pix. The wavelength resolving power is estimated to be $\lambda/\Delta\lambda$ ~330 at 6000 Å. The wavelength coverage is 4200 – 8000 Å. This configuration allow us to obtain the important physical information of compositions and velocity of expanding atmosphere of SNe.

2.1.6 8.2-m Subaru telescope, NAOJ

8.2-m Subaru telescope was constructed at the summit of Mauna Kea, Hawaii (figure 12). The diameter of the primary mirror is 8.2m, which is one of the largest monolithic mirrors in the world. It is a very strong point for observing faint object, for example, SNe at a year after discovery. Combined with 1m-class telescope, it becomes a strong tool for exploring the physical properties of inner-part ejecta. Scientific observations of Subaru telescope started in 2000.

2.1.7 FOCAS

The Faint Object Camera and Spectrograph (FOCAS; Kashikawa et al. 2002) is attached to the Cassegrain focus of Subaru Telescope. We can select various observational modes: narrow-

on are introduced in "Kanata obslog" (http://kanatatmp.g.hatena.ne.jp/kanataobslog/)

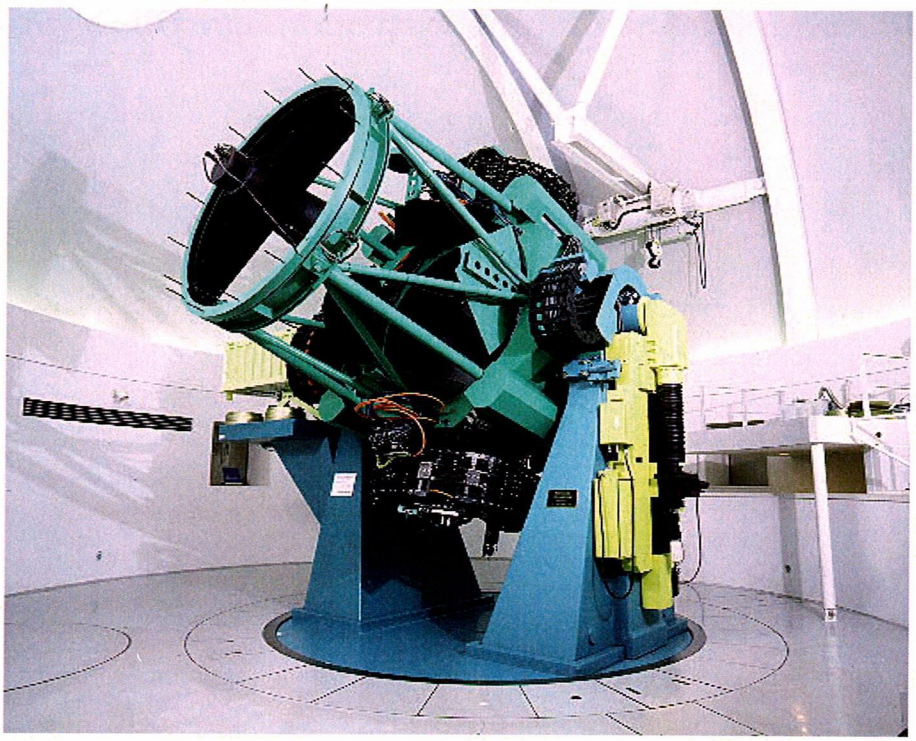

Figure 11: 1.5m telescope in Gunma Astronomical Observatory.

and broad-band imaging, low- and middle- resolution spectroscopy, multi-slit spectroscopy, polarimetry and spectropolarimetry in optical wavelength. The pixel scale and the field of view of FOCAS are 0.1"/pix and 6' in diameter, respectively. We can select applicable combination of a grating with a filter, giving the wavelength resolving power among $\lambda/\Delta\lambda \sim 250 - 7500$. For observations of SN 2009dc, We used the grating of 300R and O-58 filter, which gives a wavelength coverage of 5800 – 10200 Å. We also used used B300 grism with no filter, which gives that of 3800 – 7000 Å. The spectral resolving power of both gratings is $\lambda/\Delta\lambda \sim$500.

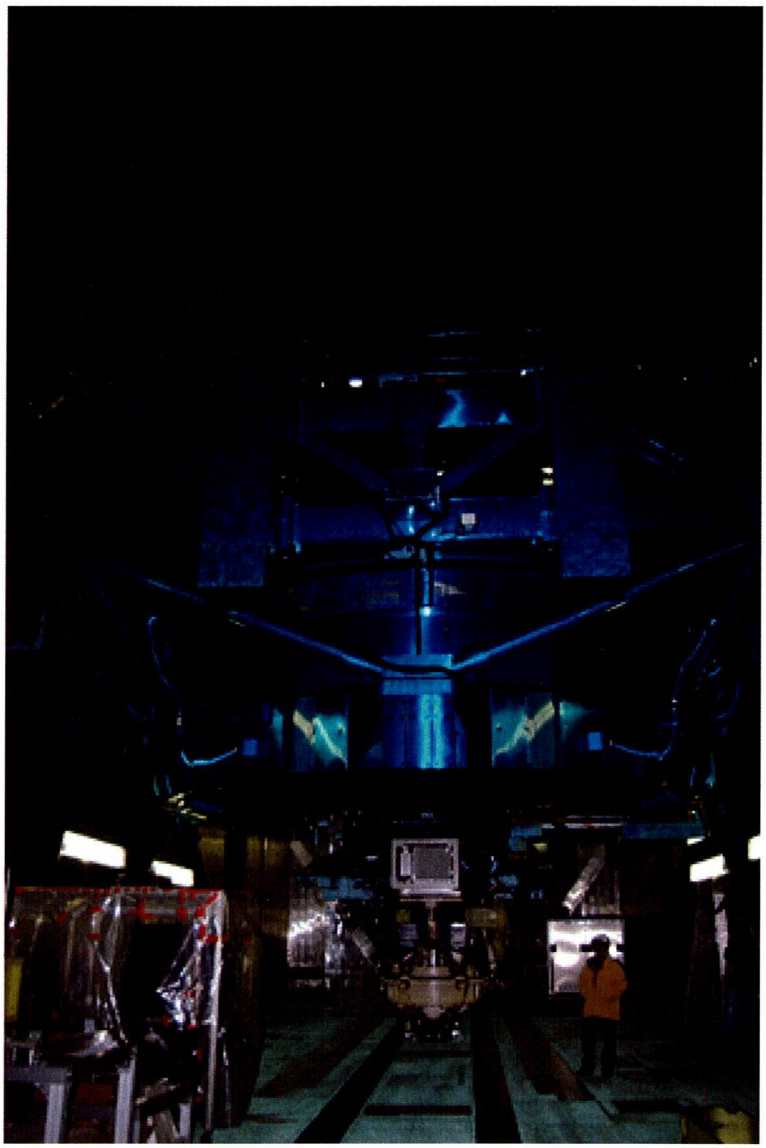

Figure 12: 8.2m Subaru telescope

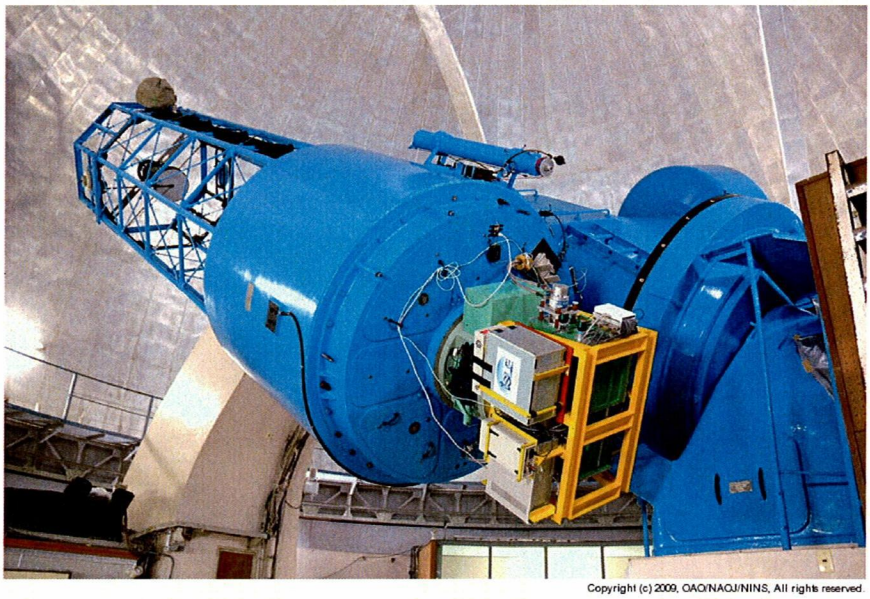

Figure 13: 1.88m telescope and ISLE

2.1.8 1.88-m telescope at Okayama Astronomical Observatory

The 1.88-m telescope at Okayama Astronomical Observatory (OAO) was constructed in 1960. Since then, it has been used as an open use telescope among Japanese optical-infrared astronomy community.

2.1.9 ISLE

ISLE (near-infrared imager and spectrograph; Yanagisawa et al. 2006) is attached to the Cassegrain focus of the 1.88m telescope (figure 13). We can select two observational modes, imaging or spectroscopy in near-infrared wavelength ($1.0 - 2.5$ μm). The detector is a 1024×1024 HAWAII array. The pixel scale and the field of view of ISLE are 0.25"/pix and 4.3' $\times$ 4.3' square, respectively. We can select J, H, K, K_S band filters for imaging observations.

We used the imaging mode for photometry of SN 2009dc in J, H, K_S-bands. Quantifying the synthesized ^{56}Ni mass in SN 2009dc is one of the most important goal for our study. ^{56}Ni mass is derived from the quasi-bolometric luminosity. For typical Type Ia supernovae, the fractions of optical flux is around 60%, however, we need to investigate the intrinsic flux distributions in SN 2009dc. We can estimate the more precise bolometric luminosity of SNe than using only optical photometry.

Table 1: Summary of telescopes and instruments

Observatory	Telescope	Instruments	Mode	Region	N Obs.[a]
HHAO	1.5m Kanata	HOWPol	Imaging	B,V,$R_{\rm C}$,$I_{\rm C}$	30
OAO	0.5m MITSuME	CCD Camera	Imaging	g',$R_{\rm C}$,$I_{\rm C}$	10
GAO	1.5m telescope	GLOWS	Spectroscopy	Optical	6
NAOJ	8.2m Subaru	FOCAS	Imaging	B,V,$R_{\rm C}$,$I_{\rm C}$	1
NAOJ	8.2m Subaru	FOCAS	Spectroscopy	Optical	3
OAO	1.88m telescope	ISLE	Imaging	J,H,$K_{\rm S}$	5
Kagoshima	1.0m telescope	Near-infrared camera	Imaging	J	2

[a]Observational numbers of nights

2.1.10 0.5-m MITSuME telescope

MITSuME (Multicolor Imaging Telescopes for Survey and Monstrous Explosion) telescope is generic name of three robotic observational instruments ,which are two 0.5m telescopes and a 0.91m telescope. These telescopes are designed for the instantaneously multi-color photometric observations of GRBs. These cameras have g', $R_{\rm C}$ and $I_{\rm C}$-band filters. We used the a 0.5m telescope in OAO for photometry of SN 2009dc.

2.1.11 1.0-m telescope at Kagoshima University

We also used the 1.0m-telescope at Kagoshima University. This telescope is constructed in order to plan the project to determine the pulsation period of Mira-type star with radio observations. The near-infrared camera is attached to this telescope. The detector of this camera is HAWAII-array. The format is 512 × 512 pix for its detector. The array of near-infrared camera has pixel scale of 0.64" pix and a field of view of 5.5' × 5.5' square in the optics of 1.0m telescope. This camera is installed to the J,H,$K_{\rm S}$-bands.

2.2 Optical Imaging

We performed BVR_cI_c-band photometry of SN 2009dc on 30 nights from 2009 Apr 17.8 UT ($-$8.1 days after B-band maximum light) through Jul 14.5 (+80.5 days) using HOWPol. We also obtained the images of photometric standard stars for photometric calibrations in photometric nights. We observed the SA107 from Landolt standard star catalog (Landolt 1992) located around R.A.=$15^h39^m08.9^s.90$, Decl.= $00°35'48.8''$. The observed filed is shown in figure 10.

Additionally, we obtained $g'R_cI_c$-band photometric data on 10 nights from $-$1.7 to +19.3

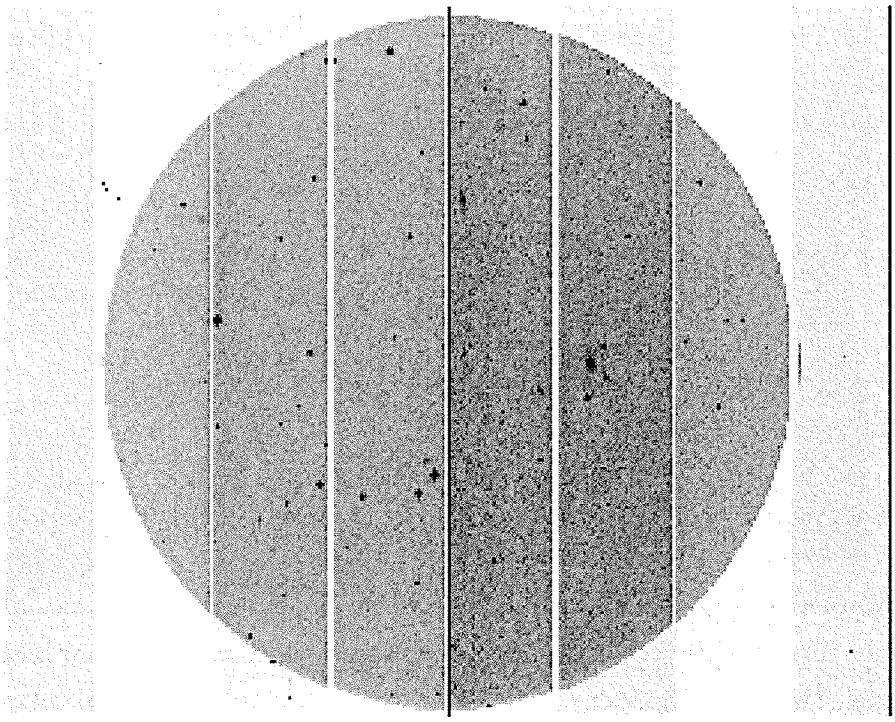

Figure 14: Raw image of SN 2009dc obtained by HOWPol. This images are composed of two different CCDs, which format is 2048 × 4096 pix. The diameter of field of view is 15' × 15' and the pixel scale is 0.3". The overscan regions are seen as three vertical lines in each CCD. These are used for the bias-subtraction.

days, using MITSuME 0.5 m telescope (Multicolor Imaging Telescopes for Survey and Monstrous Explosions).

We also performed late-phase photometric observations of SN 2009dc using FOCAS on 2010 May 13. We took images with exposure time of 240s, 120s, 60s, 60s, in the Johnson/Kron-Cousins B, V, $R_{\rm C}$, $I_{\rm C}$-bands, respectively (figure 14). We also took images of the photometric standard star PG 1525 (Landolt 1992) in same night.

2.3 Optical Spectroscopy

The optical spectra were obtained using GLOWS on six nights from −3.3 through +53.7 days. We also obtained the spectra of spectroscopic standard star in same nights. We also take the comparison lamp and flat spectrum. The observational log is summarized in table (table 2).

Spectropolarimetric observations were performed in ToO programs (S09A) on May 1.5 (+5.6 days) and July 24.4 (89.5 days) in 2009 (Tanaka et al. 2010b). We used spectra of SN 2009dc obtained in their observations.

Table 2: Log of spectroscopic observations of SN 2009dc

MJD[a]	Phase	Exposure [s]	Instrument[a]	Coverage[Å]	Res. [Å]
54943.6	−3.3	1800	GLOWS	4200 – 8000	18
54944.6	−2.3	2700	GLOWS	4200 – 8000	18
54948.7	1.8	720	GLOWS	4200 – 8000	18
54949.7	2.8	2800	GLOWS	4200 – 8000	18
54952.5	5.6	10,800	FOCAS	4400 – 9000	9
54964.6	17.7	480	GLOWS	4200 – 7500	18
54971.5	24.6	2520	GLOWS	4200 – 8000	18
55000.6	53.7	1800	GLOWS	4200 – 8000	18
55036.4	89.5	9600	FOCAS	4400 – 9000	9
55330.4	383.5	3600	FOCAS	3800 – 9500	6

[a]Modified Julian Date

We also performed late-phase spectroscopic observations of SN 2009dc using FOCAS on 2010 May 13 (383.4 days). We used 0".8-wide slit and the R300 grism with the O-58 filter, which gives a wavelength coverage of 5800 – 10200 Å. We also used B300 grism with no filter, which gives that of 3800 – 7000 Å. The spectral resolution is estimated to be 12 Å at 6000 Å. To carry out the wavelength calibration, we obtained spectra of a comparison lamp. We also observed a standard star Feige 34 on the same night for flux calibration.

2.4 Near-Infrared Imaging

Our near-infrared (NIR) photometric data were obtained in JHK_S-bands from −2.8 through +44.0 days using 1.88-m telescope with ISLE at OAO. We also performed the J-band imaging observations at 2 nights, 6.5 and 43.1 days after B-band maximum using 1.0-m telescope in Kagoshima University.

3 Data Reductions

We have obtained various observational material using six different telescopes and instruments. We must calibrate and combine them properly for later analysis. We need to convert the raw data into calibrated ones through the reduction because the raw data involve unnecessary and sometimes harmful components, for example, the bias count, flat-field, and so on. Here, we introduce our reduction procedure, which is different in optical and near-infrared imaging and spectroscopy due to large difference in the background component versus the target count level. The data reduction was mainly performed using IRAF [4].

3.1 Optical Imaging Data

When we obtain an astronomical image using a CCD, the image generally includes both bias and dark components. These must be removed. For CCDs we used, they are sufficiently cooled and the dark components are negligible (a few counts pixel^{-1} hr^{-1}). Therefore, we removed only the bias component.

In the following, we describe the reduction procedure for HOWPol and FOCAS, which is basically consistent with the standard one. We used overscan regions in CCDs for the estimation of the bias count level (figure 14). We performed the bias estimation and subtraction simultaneously with the IRAF task `background`. Then we performed binning (combined each neighboring pixels) of 3×3 pixels and shrinked the image size. For FOCAS data, we simply averaged the bias images (taken with zero second exposure with the shutter closed) and subtracted it from the target and other frames.

In both HOWPol and FOCAS data, we adopt the dome flat-field data for correction of relative sensitivity within the field of view. Flat-fielding is strongly dependent on sensitivity of each filter. Dome flat is taken using artificial lamp irradiating a board on the dome. The dome flat-field image is taken for the dome screen illuminated by artificial lamps. Since the flat-field screen image is highly out of focus, the data can be considered to be an image taken for the light source of which the spatial distribution is flat. Since the pattern of the flat-field image depends on wavelength, i.e., the band filter used, we made flat-field image for each band.

We combined using IRAF task to averaged images from the multiple ones. We combined multiple frames taken with the same filter to make a flat-field image with higher S/N ratio.

[4]IRAF is distributed by the National Optical Astronomy Observatory, which is operated by the Association of Universities for Research in Astronomy (AURA) under cooperative agreement with the National Science Foundation.

Each averaged image is then normalized, i.e., divided by the peak count.

Then, the bias-subtracted targets frames are divided by the corresponding normalized flat-field image. We show the sample flat-fielded images of HOWPol and FOCAS in figures 15 and 16, respectively.

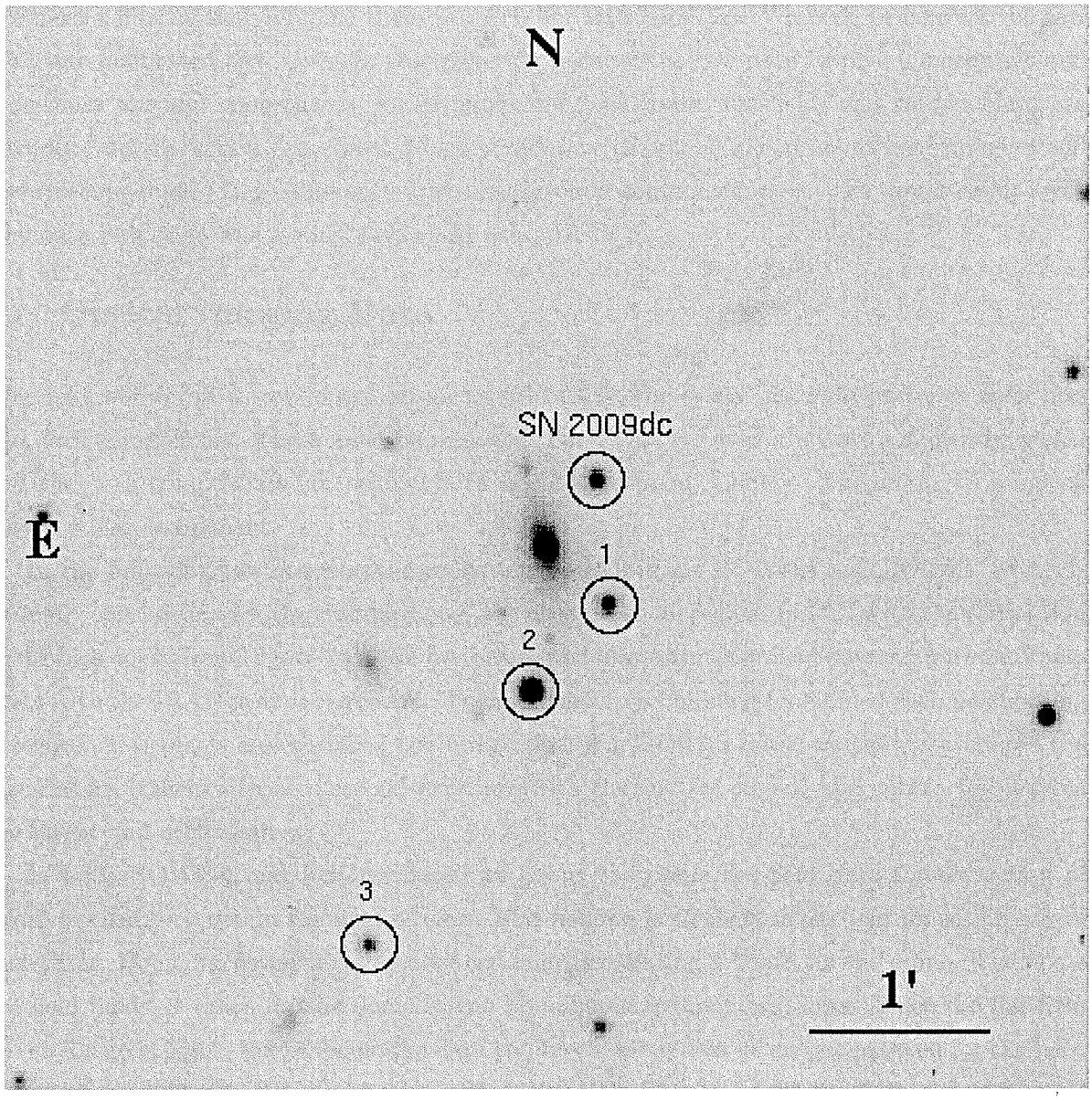

Figure 15: A sample flat-fielded R_C-band image obtained using 1.5-m Kanata telescope with HOWPol.

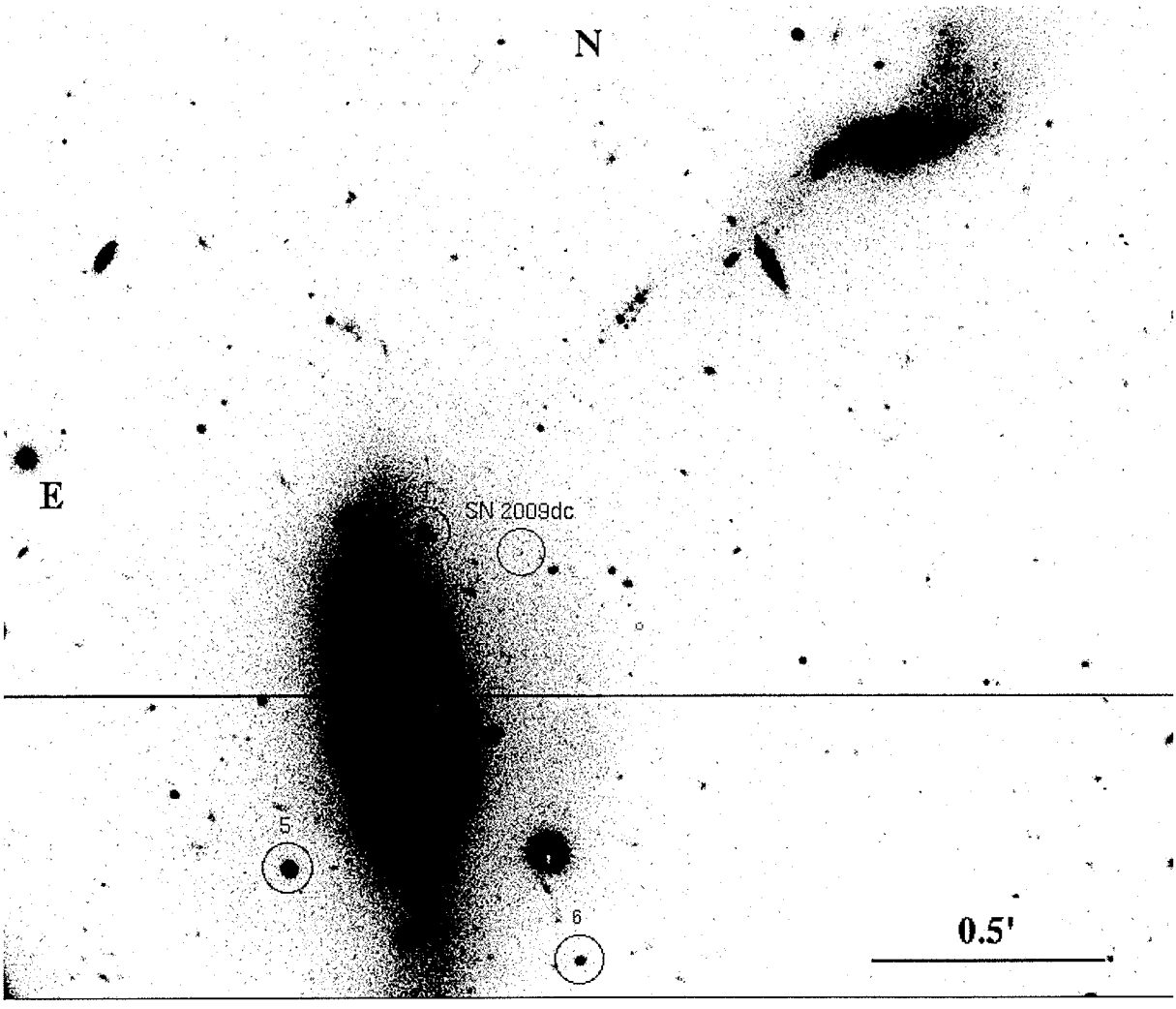

Figure 16: A sample flat-fielded R_C-band Image obtained using 8.2-m Subaru telescope with FOCAS.

3.2 Near-infrared Imaging Data

We obtained near-infrared images using 1.88-m telescope at OAO and the 1.0-m telescope at Kagoshima. For these images the data reduction were carried out by one of our collaborator, Dr. A. Imada. We describe only the outline of data reduction specific for near-infrared data.

The near-infrared data are characterized by large background counts (thermal radiation from the instruments and the sky, and thermal noise inside the detector itself) and worse cosmetics of the array (i.e., existence of more bad pixels). Therefore, we usually take the target images with so-called 'dithering' technique, in which we move the telescope with small offsets frame to frame, and combine them after the flat-fielding. We also take the dark images with the shutter

closed and the same exposure time as the target frames. The flat-field images were obtained in a similar way to the optical imaging data.

3.3 Photometry

Photometry is a process to measure the stellar flux component from the obtained image. Mainly, there are two methods; one is the aperture photometry and the other the point-spread function (PSF) photometry. In aperture photometry, the signal from the object is integrated within an aperture. Usually, the aperture size is fixed to be $2-3\times$FWHMs of the stellar image size. The sky region is fixed as a doughnut-like region encircling the stellar aperture, of which the inner radius is as 2-pixel large as the radius of the stellar aperture. The level of the sky count is derived from the average count in this region. However, it is not favored in crowded star regions like a galaxy, a cluster and a nebular object because the sky region is contaminated by other stars. In these cases, the PSF photometry is better. For SN 2009dc, the contamination of the host galaxy is not completely negligible, we adopt PSF photometry.

3.3.1 PSF Photometry using DAOPHOT

The basic of PSF photometry using using the package `DAOPHOT` in IRAF is introduced in Stetson (1987). This method has a merit in the photometry for the objects locating in a crowded cluster or near the bright galaxy/nebular component. In principal, the image profile (i.e., distribution of the surface brightness) is represented by a Gaussian or a Gaussian-like function, which is called as point-spread function. Thus, we can derive accurate stellar count by fitting the PSF function to the image profile. We make the PSF model function using the non-contaminated stars taken in the same frame. We write down the procedure of the PSF fitting photometry. There are many parameters and options for PSF photometry, e.g., function type, initial value of the function, pixel range used for the fit, etc. We outline the following procedure in Appendix.

Table 3: Standard magnitudes of comparison stars

star ID	R.A.	Decl.	B	err_B	V	err_V	R_C	$\mathrm{err}_{R_\mathrm{C}}$	I_C	$\mathrm{err}_{I_\mathrm{C}}$
1	15:51:11.82	+25:41:47.8	16.628	0.091	15.728	0.083	15.239	0.061	14.877	0.082
2	15:51:13.58	+25:41:20.9	15.341	0.085	14.319	0.086	13.771	0.061	13.363	0.083
3	15:51:17.43	+25:39:59.6	17.139	0.081	16.415	0.079	16.009	0.060	15.703	0.079
4	15:51:13.03	+25:42:31.1	21.937	0.112	20.721	0.068	19.916	0.040	19.231	0.049
5	15:51:14.37	+25:41:46.5	20.356	0.110	19.135	0.059	18.326	0.039	17.627	0.049
6	15:51:11.50	+25:41:33.8	21.262	0.111	20.718	0.064	20.378	0.037	20.124	0.060

3.3.2 Photometric Calibration

For magnitude calibration, we adopted a relative photometry in which we derive object magnitude relative to the comparison star taken in the same frame. (We checked the constancy of the comparison star's magnitude by adopting secondary and partially comparison stars and checking the differential magnitude between them.) We calibrate the magnitude of the comparison star using photometric standard stars in the Landolt catalog (Landolt 1992).

Most of these standard stars are located along celestial equator. We chose the sky region SA 107 because it locates near the right ascension of SN 2009dc. However, since the declination is different, the latitude at observation is generally different between SN 2009dc and SA 107. Since the extinction by the atmosphere (or the amount of the airmass) changes greatly with the latitude and the wavelength (or band), we adopted the airmass-latitude-band relation shown in Chronological Scientific Tables 2004 (2003). Since the linearity of the detector sensitivity, i.e., the relation between the amount of illumination and the obtained count, is quite good as far as we use them below the linearity-breaking count, the obtained counts per a second is simply proportional to the flux of the star.

We can derive the magnitude from the obtained count as

$$m_1 = m_0 + 2.5 \log N, \tag{4}$$

where m_1 the magnitude of object, m_0 is a constant for the observation system which can be calculated for magnitude-known star (i.e., standard star), and N is the obtained counts per a second.

When we calculate the magnitudes of comparison stars from standard stars, we also correct for the color term. Since the sensitivity function (a product of filter transmission and detector's sensitivity function) is generally different from the standard system (Bessell 1990), the magnitude in a broad-band is slightly affected by the flux distribution versus the wavelength. We usually correct it using a linear term of the magnitude against the color index (or indices). We obtained the color terms for standard star observations and then corrected for them in each instrument. Finally, we obtain the magnitudes in $BVR_{\rm C}I_{\rm C}$-bands of comparison stars, which are summarized in table 3. These magnitudes are consistent with those of both Taubenberger et al. (2010) and Silverman et al. (2010) within 2 σ error.

In near-infrared images, there is no star catalog of standard magnitudes. Their magnitudes were calibrated with nearby stars in 2MASS catalog. For near-infrared images, we calibrated the magnitude using nearby stars listed in 2MASS catalog which are taken in the same frame. The maximum error is expected to be 0.1 mag. The maximum error in this calibration method

Figure 17: Two-dimensional spectral image of SN 2009dc obtained on 2010 Apr 22 by the 1.5-m telescope at GAO and GLOWS. The bias-subtraction and flat-fielding have been done. The horizontal axis corresponds to wavelength direction (left is shorter wavelength) and the vertical one denotes the slit (i.e., spatial) direction. Thick horizontal line is the continuum spectrum of the supernova and several vertical lines are sky emission lines.

is expected to be 0.1 mag, which is a typical one for calibration with 2MASS stars.

3.4 Spectroscopy

We describe our spectroscopic reduction procedure for GLOWS and FOCAS data. The bias subtraction and the flat-fielding were performed in the same manner as the photometric reduction. We also removed the cosmic ray events and made cleaned images. We used task `cosmicray` and `fixpix` on IRAF. These tasks are performed on the interactive mode.

We show the two-dimensional spectral image obtained by GLOWS in figure 17. The position of the supernova spectral image sightly warped with wavelengths because of the aberration of the optics in the instrument. We fit the vertical position of the spectrum against wavelength using two- or three-order *Legendre* function. Once we derive the function, we can trace the object position along the dispersion direction and extract it properly. We also determine the size of aperture and sky regions. We show the one-dimensional spectrum of extracted aperture region for supernova and standard star in figure 18.

For the late-phase spectroscopy with FOCAS on 2010 May 13, we cannot detect any spectrum of SN 2009dc because it has declined below the limiting magnitude. The spectrum of SNe and standard star were taken in the same position in CCD. Assuming the distortion (a kind of aberration) is constant, it is acceptable that we obtain the trace function using bright stars and then apply it for faint star data. Finally, we subtracted the sky background component and integrate the stellar component along the slit direction. Then, we obtained the one-dimensional supernova spectrum.

3.4.1 Wavelength Calibration

We present the procedure of wavelength calibration for data obtained by GLOWS and FOCAS. We show the comparison lamp spectrum obtained by GLOWS in figure 20. This spectrum

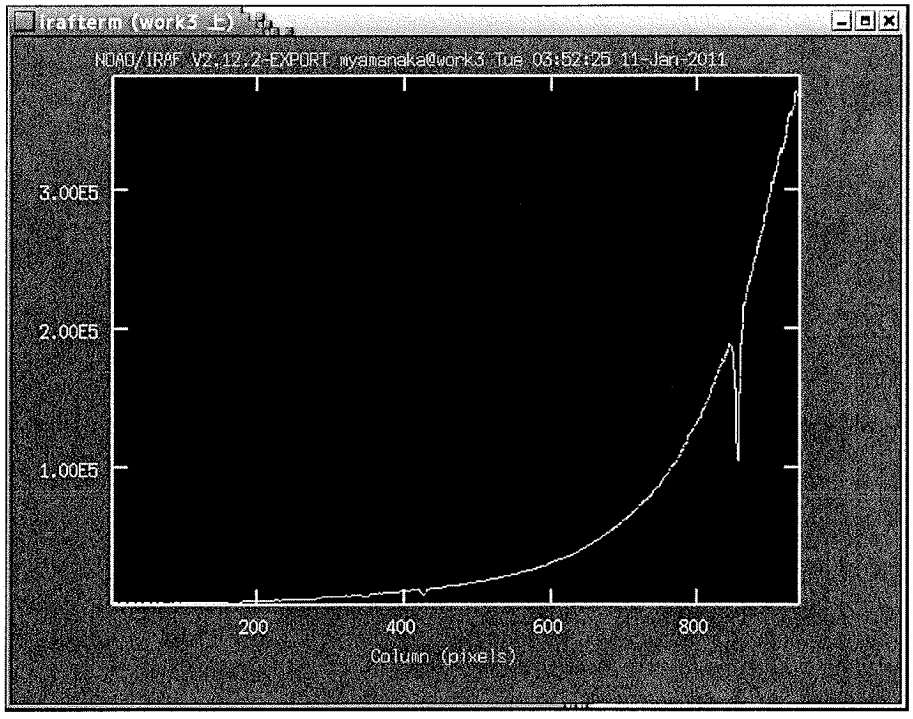

Figure 18: The spectrum of HR4963 obtained by GLOWS. This spectrum was traced using the Legendre function of a few orders.

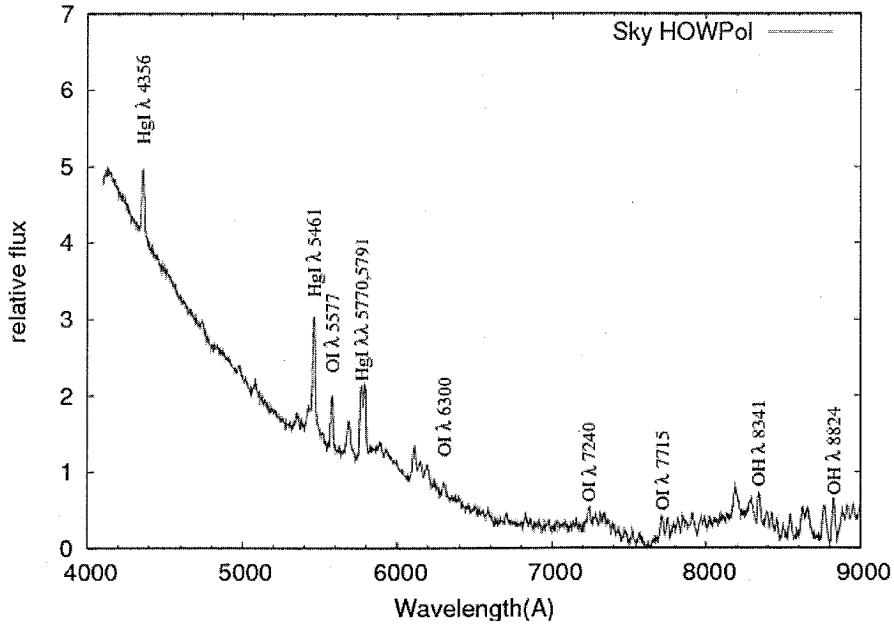

Figure 19: The sky spectrum obtained by HOWPol with 1.5-m Kanata telescope. The spectrum exhibits the Hg I, O I, Na I and telluric lines. These line features are used for wavelength calibration.

exhibits the Fe, Ne and Ar emission lines. We identified each line compared with a reference spectrum using task `identify` associated in a package `onedspec`. We fitted more than three-order Legendre function to the combination of the wavelength and the pixel position of each emission line.

However, this fit is insufficient due to the mechanical shift of the spectrum for GLOWS. This is caused by a flexure which is different between in object and comparison lamp observations. In order to correct for this shift, we used the sky spectrum (as a reference, we show the sky line obtained by HOWPol in figure 19). Sky spectrum exhibits the Hg I, O I, Na I and telluric lines. We identified these emission lines and fitted a linear function, and then re-calibrated the wavelength in the spectrum. Finally, we get the wavelength-calibrated spectrum within an error of RMS$\sim$1.0 Å.

3.4.2 Flux Calibration

We explain the procedure of flux calibration, which was commonly performed for both GLOWS and FOCAS data. The flux calibration were performed with the IRAF package `onedspec`. We removed absorption lines seen in spectra of standard star and make a file using command `standard`.

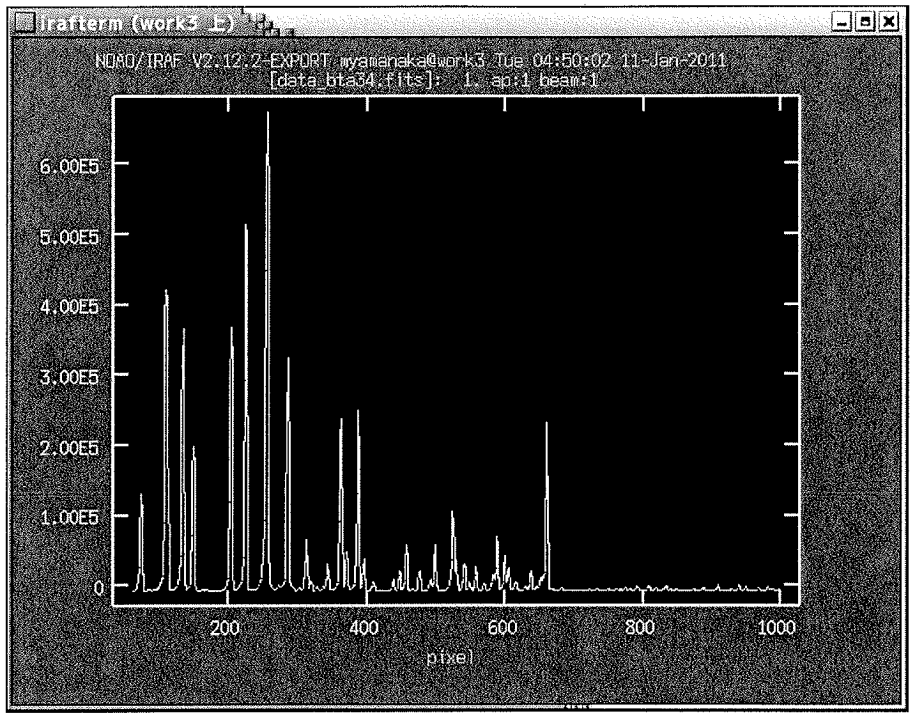

Figure 20: The spectrum of a comparison lamp obtained by GLOWS at GAO. The emission lines are of Fe, Ar and Ne. These features are used for wavelength calibrations of the spectrum.

First we prepared a one-dimensional, wavelength-calibrated spectrum of a spectrophotometric standard star and registered the calibration data using the IRAF task `standard`. We fitted a high-order function to the continuum spectrum of the standard star using task `sensfunc`. Using its fitting results of sensitive function for standard star, we calibrated the spectrum of object. Finally, we checked the consistency between the flux level in the spectra and the photometric results. We also have removed the strong telluric absorption features from the object spectra using the standard star spectra.

For the late-phase data obtained on 2010 May 13, the flux level of the spectrum was only 30 % of the photometric results. This would be caused by a loss of illumination on the narrow slit due to guiding error and/or the bad seeing. Therefore, we re-scaled the spectrum to be consistent with the photometric result on the same night.

4 Results

4.1 Light Curves

We show optical and NIR light curves of SN 2009dc in figures 21 and 23. The data have been corrected for the Galactic extinction of $E(B-V) = 0.071$ mag and $R_V = 3.1$ (see §3.3). We derive the B-band maximum magnitude of 15.19 ± 0.16 mag and its date of 54946.9 ± 0.2 MJD[5] (Apr 25.9±0.2 UT) by fitting of the third-order polynomial to the light curve. We also derived the B-band maximum of 54948.3 ± 0.3 MJD by fitting the SALT2 model curve (Guy et al. 2007), which is 1.43 days later than that of the polynomial fitting. Since the light curves of SN 2009dc is atypical, we should be careful for the result of the SALT2 model. Since the density of our data points is likely sufficient for polynomial fitting, we adopt the B-band maximum day of 54946.9 ± 1.4 MJD (Apr 25.9 ± 1.4) in this thesis.

In figure 21, we compare SN 2009dc with the super-Chandrasekhar SN Ia 2006gz (Hicken et al. 2007, ;$\Delta m_{15}(B) = 0.69$) and a normal SN Ia 2003du (Stanishev et al. 2007, ; $\Delta m_{15} = 1.02$)). We notice that the brightness evolution of SN 2009dc across the maximum is slower than those of SNe 2003du in all bands. We derive the decline rate of $\Delta m_{15}(B) = 0.65 \pm 0.03$ for SN 2009dc, which is similar to $\Delta m_{15}(B) = 0.69 \pm 0.04$ of SN 2006gz (Hicken et al. 2007). The decline rate of SN 2009dc is one of the slowest ones among SNe Ia which have ever been published (figure 27). It indicates that SN 2009dc is extremely bright at the peak. In fact, even if the extinction within the host galaxy is negligible, the absolute maximum magnitude is estimated to be $M_V = -19.90 \pm 0.15$ mag from the peak apparent magnitude of $V = 14.98$ and the distance modulus of $\mu = 34.88$. It indicates that SN 2009dc is one of the most luminous SNe Ia ever discovered (see §5.3). It is important result that the SN 2009dc is consistent with the width-luminosity relation.

[5]Modified Julian Date

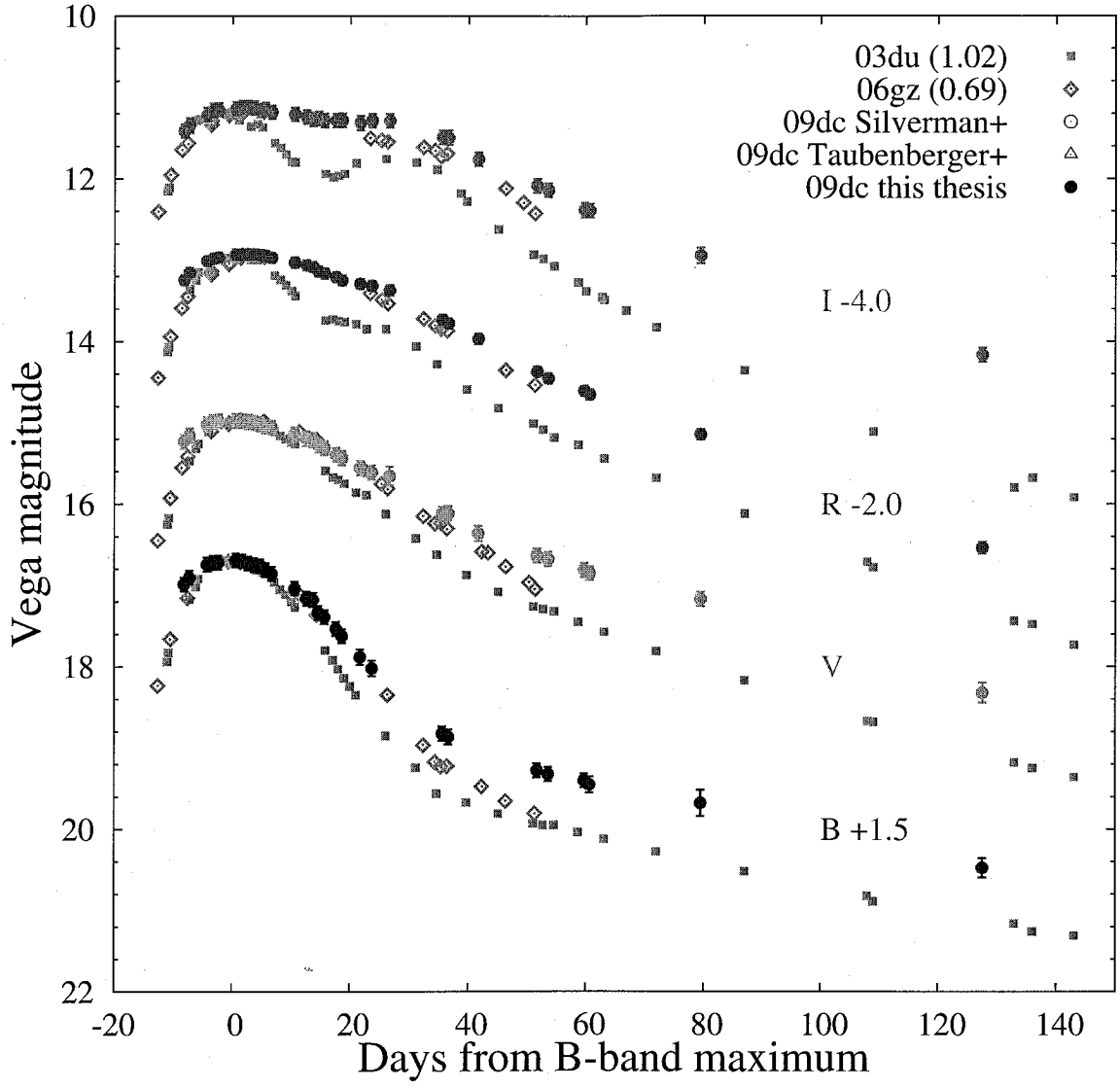

Figure 21: Light curves of SN 2009dc, compared with a super-Chandrasekhar SNe Ia 2006gz (Hicken et al. 2007) and a normal SN 2003du (Stanishev et al. 2007). The Galactic extinction has been corrected for in SN 2009dc. For other SNe, the extinction of both our galaxy and the host galaxy have been corrected for ($E(B-V) = 0.12$ for SN 2006gz). Parenthetic numbers mean the $\Delta m_{15}(B)$ of each SN Ia.

The J-band light curve shows a significant dip between the first and second maximum compared with the optical light curve (figure 23). The H and K-band magnitudes suggest the existence of more luminous secondary peak than the first one. These characteristics are likely typical for SNe Ia (Krisciunas et al. 2004; Wang et al. 2009). These are the first NIR photometry of super-Chandrasekhar SNe Ia ever published.

In figure 22, we plot $BVR_{\rm C}I_{\rm C}$-bands photometric data of SN 2009dc up to $\sim$ 400 days after B-band maximum. We also plot the late-phase data from Silverman et al. (2010) and Taubenberger et al. (2010). In $R_{\rm C}$-band, our photometric point are slightly fainter than that of Silverman et al. (2010). We also plot the photometric points of SNe 2003du and 2006gz as comparisons. The decline rates of SN 2009dc become larger than those in previous phase in $BVR_{\rm C}$-bands. In $I_{\rm C}$ band, that is comparable to the slope of the linear decline at 50—150 days.

At 250 – 300 days, the magnitude decreases relative to the B-band maximum are similar to those of SNe 1991T and 2003du in $VR_{\rm C}I_{\rm C}$-bands, while that is larger in B-band (Silverman et al. 2010; Taubenberger et al. 2010). Thereafter, at 350 – 400 days, the decreases in $BVR_{\rm C}I_{\rm C}$-bands clearly become larger than that of typical SN Ia 2003du. Another SC SN Ia 2006cz was $R_{\rm C} = 25.5$ mag at +367 days (Maeda et al. 2009). Interestingly, the decreased magnitude relative to maximum is well consistent with that of SN 2009dc. This facts mean that the late-phase light curves in both SNe 2006gz and 2009dc exhibit a rapid decline. Thus, the rapid decline might be a common property in SC SNe Ia.

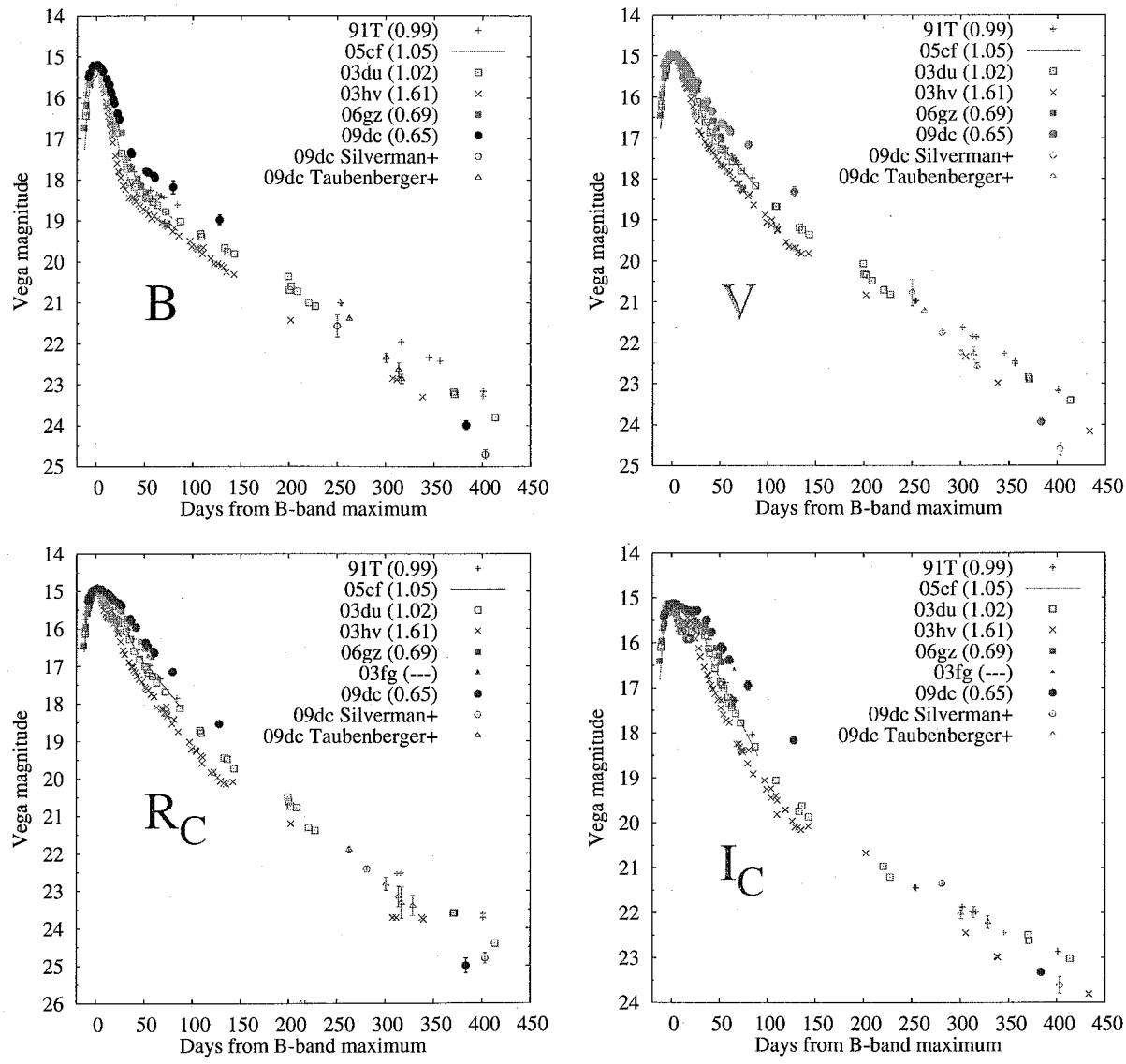

Figure 22: Light curves of SN 2009dc compared with luminous Type Ia SN 1991T (Lira et al. 1998), normal Type Ia SNe 2005cf (Wang et al. 2009), 2003du (Stanishev et al. 2007), 2003hv (Leloudas et al. 2009), SC SN Ia 2003fg (Howell et al. 2006) and another SC SN 2006gz (Hicken et al. 2007) until 400 days after B-band maximum. These magnitudes are artificially shifted so that the maximum magnitude of every SN matches that of SN 2009dc for comparison. The colors are in the same manner as in figure 21. The photometric data of SN 2009dc obtained by Silverman et al. (2010) and Taubenberger et al. (2010) are also plotted. Parenthetic numbers mean the $\Delta m_{15}(B)$ of each SN Ia.

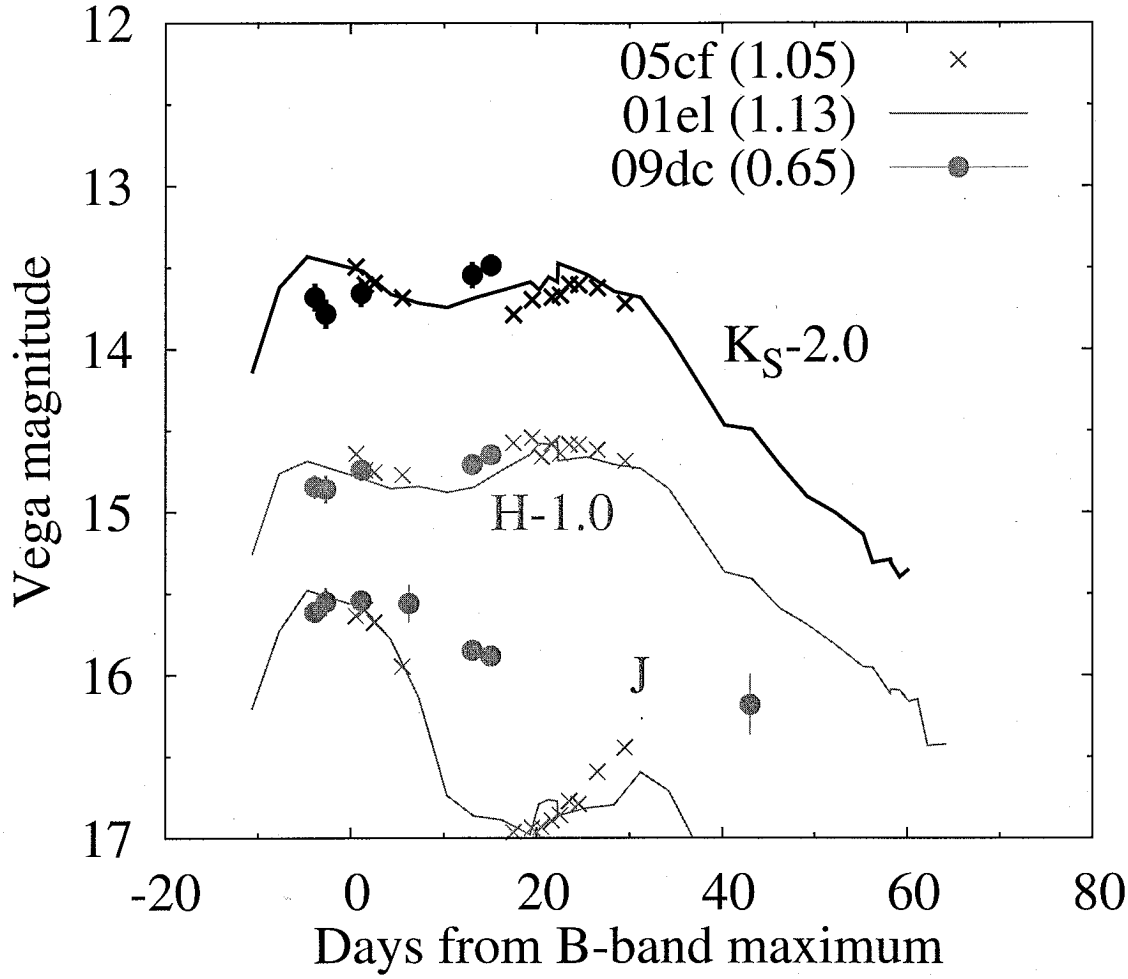

Figure 23: The J,H and K_S-bands light curves of SN 2009dc comparing with those of typical SNe Ia 2005cf (Wang et al. 2009) and 2001el (Krisciunas et al. 2004). In this splot the light curves of SNe 2005cf and 2001el are artificially shifted to match SN 2009dc at peak. The Galactic extinction have been corrected for.

4.2 Color Evolution

We show the evolution of color indices of SN 2009dc in figure 24, together with those of SNe 1991T, 2005cf and 2006gz for comparison. The data of SN 2009dc have been corrected for only the Galactic extinction ($E(B-V) = 0.071$ mag and $R_V = 3.1$), while those of other comparison SNe Ia have been corrected for both our Galaxy and host galaxies. The evolution of $B-V$ of SN 2009dc is similar to those of SNe 1991T, 2005cf and 2006gz. This suggests that the Lira-Phillips relation (homogeneous $B-V$ evolution at 30–90 days, (Phillips et al. 1999) also holds for SN 2009dc, which will be discussed in §4.3. On the other hand, the evolutions of $V-R$, $R-I$ and $V-I$ colors in SN 2009dc are somewhat different from those of SNe 1991T and 2005cf. The color indices of SN 2009dc become redder monotonically, while the other SNe Ia (except for SN 2006gz) have small troughs at 10–15 days after the B-band maximum. SN 2006gz shows color evolution similar to SN 2009dc, while SN 2006gz keeps bluer at -8 through $+60$ days and shows relatively large troughs in the $R-I$ and $V-I$ curves.

We plotted the $B-V$ and $V-I_C$ color curves together with those of typical Type Ia SN 2003du including late-phase date and another SC SN 2006gz in figure 25. The evolution to bluer color proceeds more slowly until 120 days compared with the typical Type Ia SN 2003du (Yamanaka et al. 2009a; Silverman et al. 2010; Taubenberger et al. 2010). Silverman et al. (2010) point out that the decline rate is especially slow in V and I_C bands in this phase. For the reddening in $V-I_C$ after 250 days, a contribution of an additional flux in not V but I_C should be discussed. In spectra at 50 – 100 days, there is no strong emission line above 7000 Å (Tanaka et al. 2010b; Silverman et al. 2010; Taubenberger et al. 2010). The higher flux in I_C-band might be caused by a combination of many unresolved emission lines. After 200 days, the blueing tendency in $B-V$ continues until 400 days, and it finally becomes comparable to that of SN 2003du around 350–400 days. On the other hand, the difference in $V-I_C$ between SC Ia SNe and SN 2003du becomes larger and larger in the late phase On the other hand, $V-I_C$ evolves to red color and reach $V-I_C \sim 0.5$ in contrasting to that of SN 2003du, whose $V-I_C$ evolves to rather blue color.

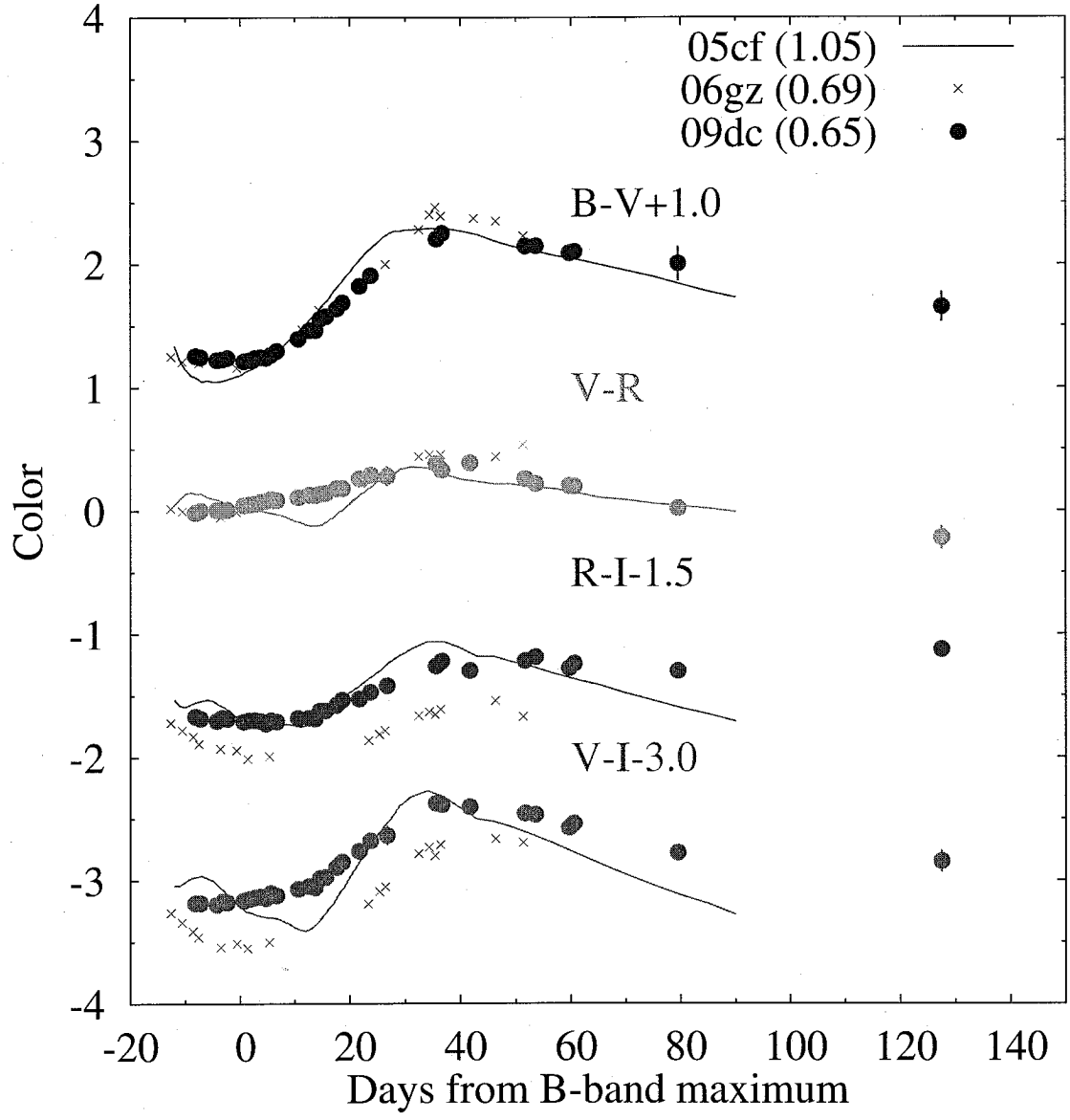

Figure 24: $B-V$, $V-Rc$, $Rc-Ic$, $V-Ic$ color evolutions, compared with those of 2005cf and 2006gz. In SN 2009dc, only Galactic extinction ($E(B-V) = 0.071$ mag and $R_V = 3.1$) is corrected for. In other SNe Ia, the extinctions in both our and host galaxies are corrected for (0.12 for SN 2005cf, 0.12 for SN 2006gz). The color evolution of SN 2009dc is unique compared with those of the other SNe Ia.

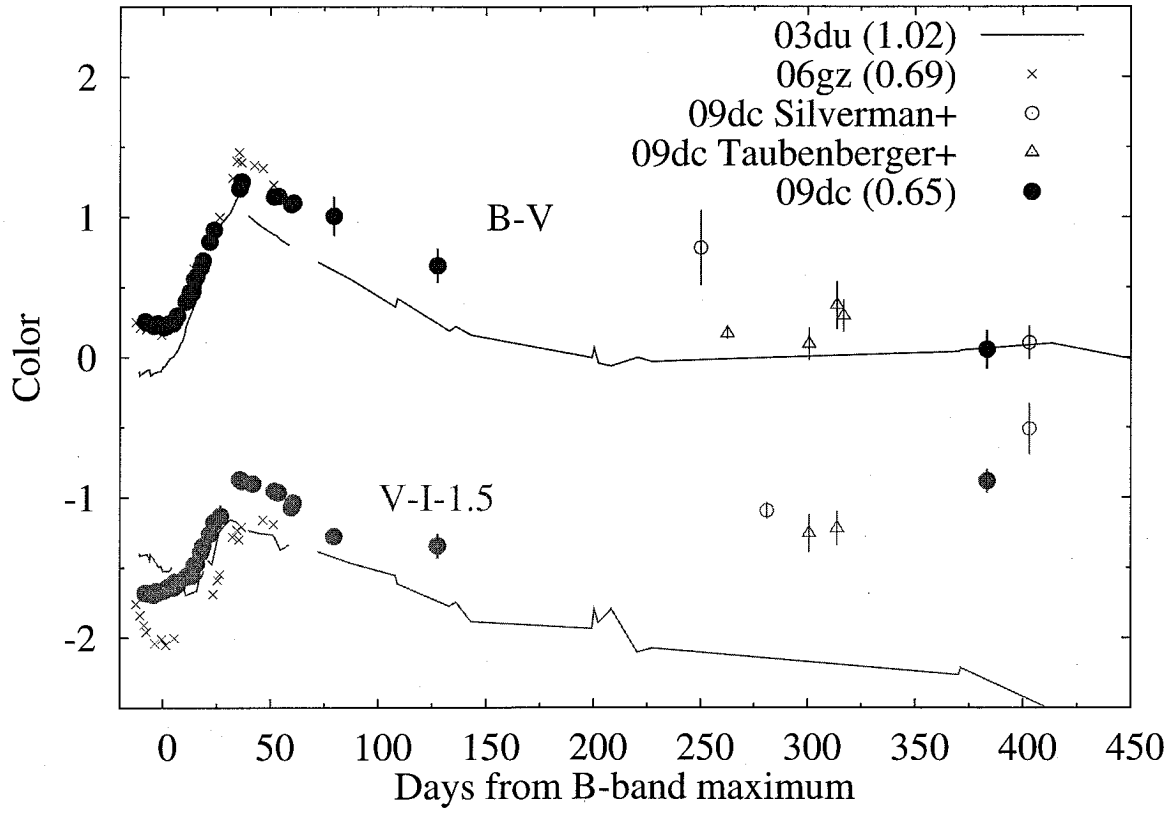

Figure 25: Longer-term $\tilde{B} - V$ and $V - I_C$ variations of SN 2009dc comparing with those of typical Type Ia SN 2003du (Stanishev et al. 2007) and another SC SN Ia 2006gz (Hicken et al. 2007). The Galactic color excesses are corrected for using the extinction map in Schlegel et al. (1998). The host galactic extinction has not been corrected for in SN 2009dc. Photometric data from Silverman et al. (2010) and Taubenberger et al. (2010) are also plotted.

Table 4: Estimated maximum absolute magnitude, luminosity and the ^{56}Ni mass in some extinction models

Model	E($B-V$) Galactic	E($B-V$) host	host A_V (mag)	R_V	$M_{V,\max}$ (mag)	$L_{\max}$ (erg s^{-1})	^{56}Ni mass ($M_\odot$)
1	0.07	0	–	3.1	-19.90 ± 0.15	$(2.1 \pm 0.5) \times 10^{43}$	1.3 ± 0.3
2	0.07	0.14	0.29	2.1	-20.19 ± 0.19	$(2.9 \pm 0.8) \times 10^{43}$	1.8 ± 0.4
3	0.07	0.14	0.43	3.1	-20.32 ± 0.19	$(3.3 \pm 0.9) \times 10^{43}$	2.0 ± 0.5

4.3 Host Galaxy Extinction and Absolute Magnitude

To derive the accurate luminosity of SN 2009dc, we should carefully determine the total extinction toward this SN.

The Galactic color excess toward the SN is estimated to be $E(B-V) = 0.071$ mag (Schlegel et al. 1998), corresponding to an extinction of $A_V = 0.22$ mag within our Galaxy (a typical selective extinction $R_V = 3.1$ is assumed). On the other hand, the extinction within the host galaxy is somewhat uncertain. If the Lira-Phillips relation holds for SN 2009dc, it predicts a reddening of $E(B-V) = 0.37 \pm 0.08$ mag. However, this is likely an overestimation because the equivalent width (EW) of the Na I D absorption line in the host galaxy (1.0 Å) is only twice the EW of Na I D in our Galaxy (0.5 Å; Tanaka et al. 2010b), showing in figure 26. If we assume that the extinction is simply proportional to the EW, $E(B-V) = 0.14$ mag is plausible for the host extinction. Additionally, the empirical relation between the color excess and the EW of Na I D (Turatto et al. 2003, ; we adopt their lower extinction case) predicts $E(B-V) = 0.15$ mag. These two values are consistent. This also suggests that the relation is consistent with the combination of our Galaxy's values $E(B-V) = 0.071$ mag and the EW of Na I D line of $= 0.5$ Å. There is an another uncertainty due to the diversity of R_V (Wang et al. 2006; Krisciunas et al. 2006; Elias-Rosa et al. 2006). In the following discussion, we adopt two cases; $R_V = 2.1$ and 3.1 as plausible values for the host galaxies (Hicken et al. 2007). In Table 1 we summarize our absolute magnitude estimation for various cases of extinction parameters.

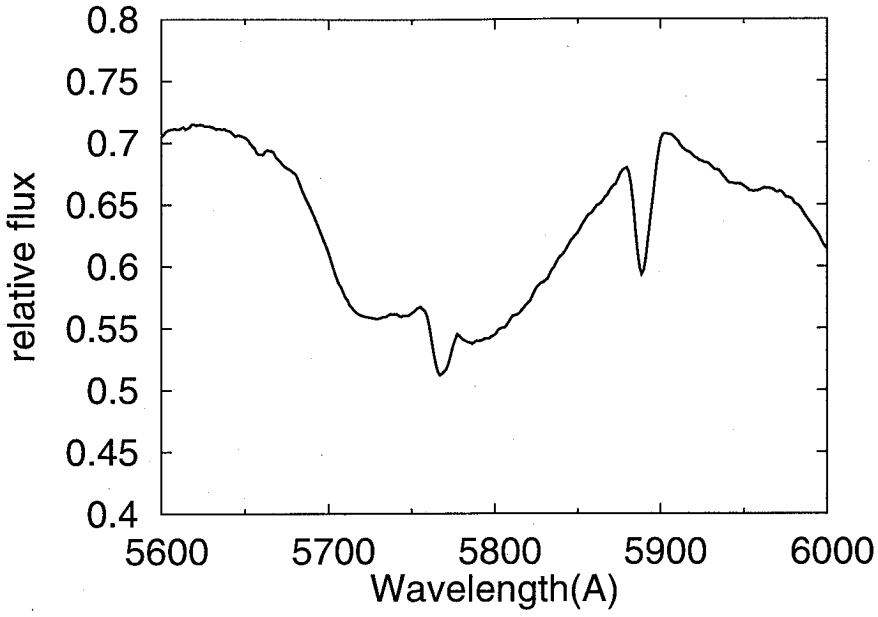

Figure 26: A magnified spectrum around Na I D lines. These lines are formed by interstellar medium within our galaxy and the host one. The width of these two lines correspond to the recession velocity of host galaxy. The line absorption at shorter wavelength is originated from our Galaxy, and that at longer wavelength is from the host galaxy. Deeper absorptions indicate that SN 2009dc is suffered from larger host galactic extinction ($A_V = 0.43$) comparing to that of Galaxy ($A_V = 0.22$).

Krisciunas et al. (2004) pointed out that the absolute maximum magnitude in NIR bands does not depend on the decline rate (except for faint SNe Ia) and derived the mean values of $M_J = -18.6$ mag, $M_H = -18.2$ mag and $M_{Ks} = -18.4$ mag at maximum. Our observation for SN 2009dc show $M_J = -19.20 \pm 0.16$ mag, $M_H = -19.00 \pm 0.17$ mag and $M_{Ks} = -19.19 \pm 0.17$ mag for zero host extinction case (extinction model 1), which suggests that SN 2009dc is exceptionally luminous even in NIR wavelengths.

It is interesting to examine whether the M_V - $\Delta m_{15}(B)$ relation (Altavilla et al. 2004) holds for this brightest SN Ia figure 27. If the SN suffers from host extinction (model 3), the absolute V magnitude derived from our observations is roughly consistent with the relation, i.e., the difference is less than $\sim 1\sigma - 2\sigma$. On the other hand, it becomes much fainter (by $3\sigma - 4\sigma$) than the prediction of this relation in case of no extinction model 1 (figure 27). However, it is still unclear whether SN 2009dc is physically apart from the relation because we do not have little samples for short $\Delta m_{15}(B)$.

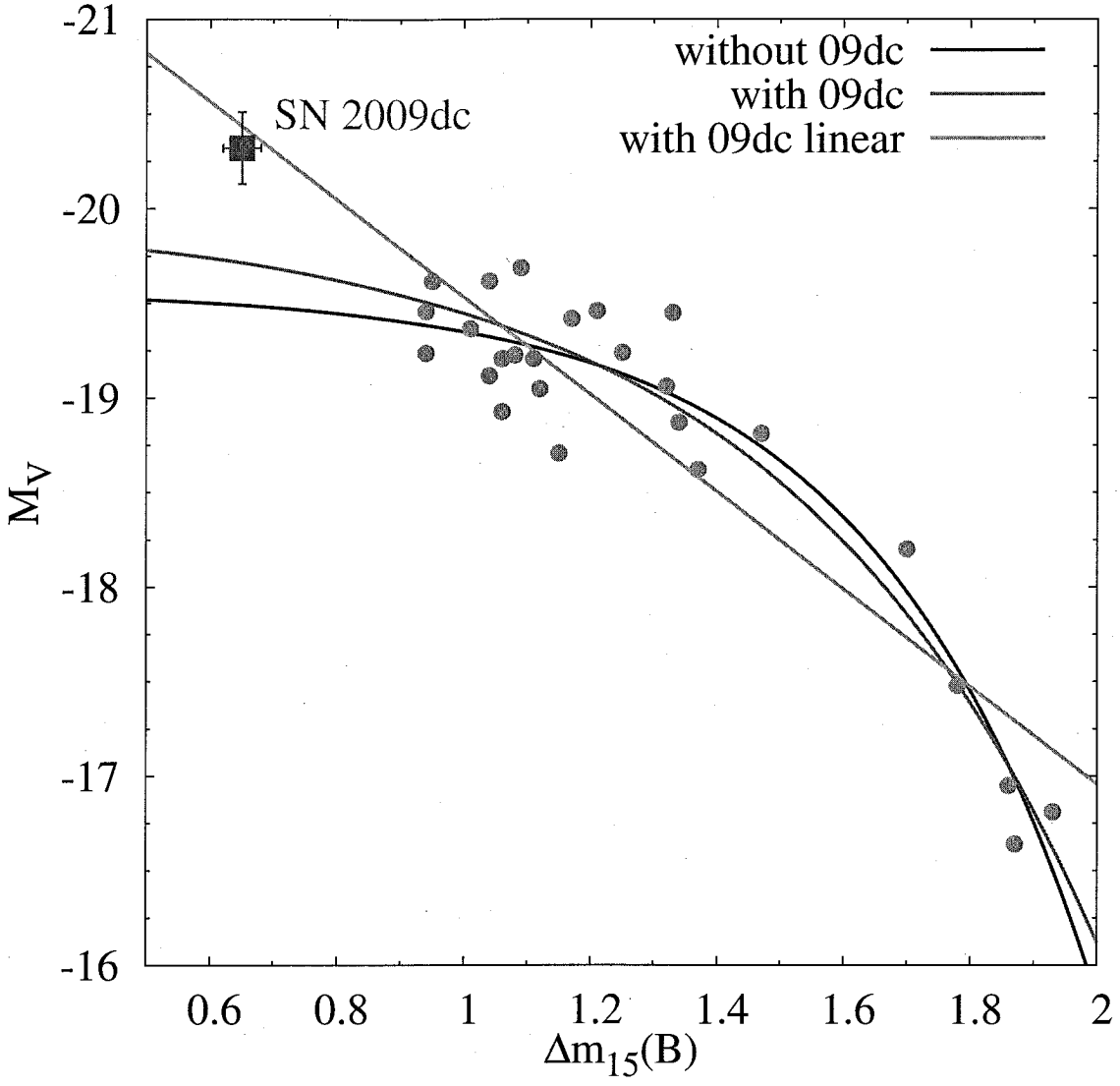

Figure 27: The correlation between between the absolute magnitudes and the decline rate ($\Delta m_{15}(B)$) is shown. Small gray points are from Altavilla et al. (2004). The red square denotes SN 2009dc (in the extinction model 3) from our observation. If we neglected the SN 2009dc data point, the other data are well represented by exponential function as the blue curve. The pink curve denotes the fitted curve including the SN 2009dc data point. Although SN 2009dc seems apart from the exponential relation, we should carefully discuss it because (1) it is marginally consistent with the pink curve within 3σ and (2) other data points are lacking below $\Delta m_{15}(B)$ $\lesssim 0.9$ and also it is unclear whether the exponential law is physically applicable for this width-luminosity relation. For example, SN 2009dc seems rather consistent if we adopt a linear law (green line).

4.4 Bolometric Light Curve

We obtain quasi-bolometric luminosity of SN 2009dc using our BVR_cI_c-band data, assuming that the optical luminosity occupies about 60% of the bolometric one around maximum brightness (Wang et al. 2009). Because of the uncertainty involved in this assumption, we consider that this bolometric luminosity may have a somewhat large systematic error ($\sim$ 20%) in this thesis. To confirm the reliability, we also calculate the quasi-bolometric luminosity from $BVRI$+$JHKs$ data at -3 days and check the consistency under the assumption that the integrated $BVRIJHKs$ luminosity is 80% of the total (Wang et al. 2009). They agree within an error of $\sim$ 12%, which is less than 20 % We must fix the extinction for the estimation of the intrinsic luminosity. Here we consider the smallest and largest cases for the extinction, i.e., the extinction model 1 and 3.

The obtained quasi-bolometric light curves are shown in figure 28. Even if we assume that the host extinction is zero, the maximum bolometric luminosity is $L_{\rm max} = (2.1 \pm 0.5) \times 10^{43}$erg s^{-1}, which is comparable to that of SN 2006gz, $(2.18 \pm 0.39) \times 10^{43}$ erg s^{-1} for $E(B-V) = 0.18$ mag (Hicken et al. 2007). When we adopt the host extinction of $E(B-V) = 0.14$ mag and $R_V = 3.1$, $L_{\rm max}$ reaches $(3.3 \pm 0.9) \times 10^{43}$erg s^{-1}, likely to exceed even that of SN 2003fg ($\sim (2.5-2.8) \times 10^{43}$ erg s^{-1}; Howell et al. 2006).

Leloudas et al. (2009) studied a fractional variability of optical and near-infrared wavelengths against the *uvoir* (UV – optical – infrared) bolometric luminosity over a year (see also Sollerman et al. 2004; Stritzinger & Sollerman 2007). Taubenberger et al. (2010) present the near-infrared contribution against the *uvoir* curves for 400 days in their figure 7. The fraction increases up to 30 % from 10% among 0 – 30 days. At a year after the B-band maximum, it becomes around 30%, again. Therefore, the uncertainty of $\sim$ 20% that we assumed above would not be so bad. We also present the quasi-bolometric light curve of SN 2009dc at late phase in figure 28, respectively. The late-phase luminosity is estimated to be $L_{\rm bol} = 9.0 \times 10^{39} \pm 0.5$ erg s^{-1} for the extinction case 3. As comparisons, another SC SN 2006gz (Hicken et al. 2007; Maeda et al. 2009), the typical SNe Ia, SN 2003du (Stanishev et al. 2007) and 2003hv (Leloudas et al. 2009) are also plotted. For these SNe, the extinctions are already corrected by using the value estimated by each study. For SN 2006gz, the peak luminosity is comparable to that of SN 2009dc with no extinction model (i.e., extinction case 1). If the extinction is corrected for SN 2009dc, the peak luminosity is clearly higher than that of SN 2006gz (Hicken et al. 2007; Yamanaka et al. 2009a; Silverman et al. 2010; Taubenberger et al. 2010).

In contrast to extremely high luminosity of SN 2009dc at the early phase, the luminosity at late-phase is rather comparable to those of SN 2003du. In SN 2006gz, we can convert the

magnitude of 25.5 in $R_{\rm C}$ to the quasi-bolometric luminosity of $L_{\rm bol} = 3.4 \times 10^{39}$ erg s^{-1} with the assumption that $R_{\rm C}$-band fraction is 11 % against the bolometric luminosity in this phase. The estimated luminosity of SN 2006gz is a bit dimmer than that of SN 2009dc in the no host extinction case.

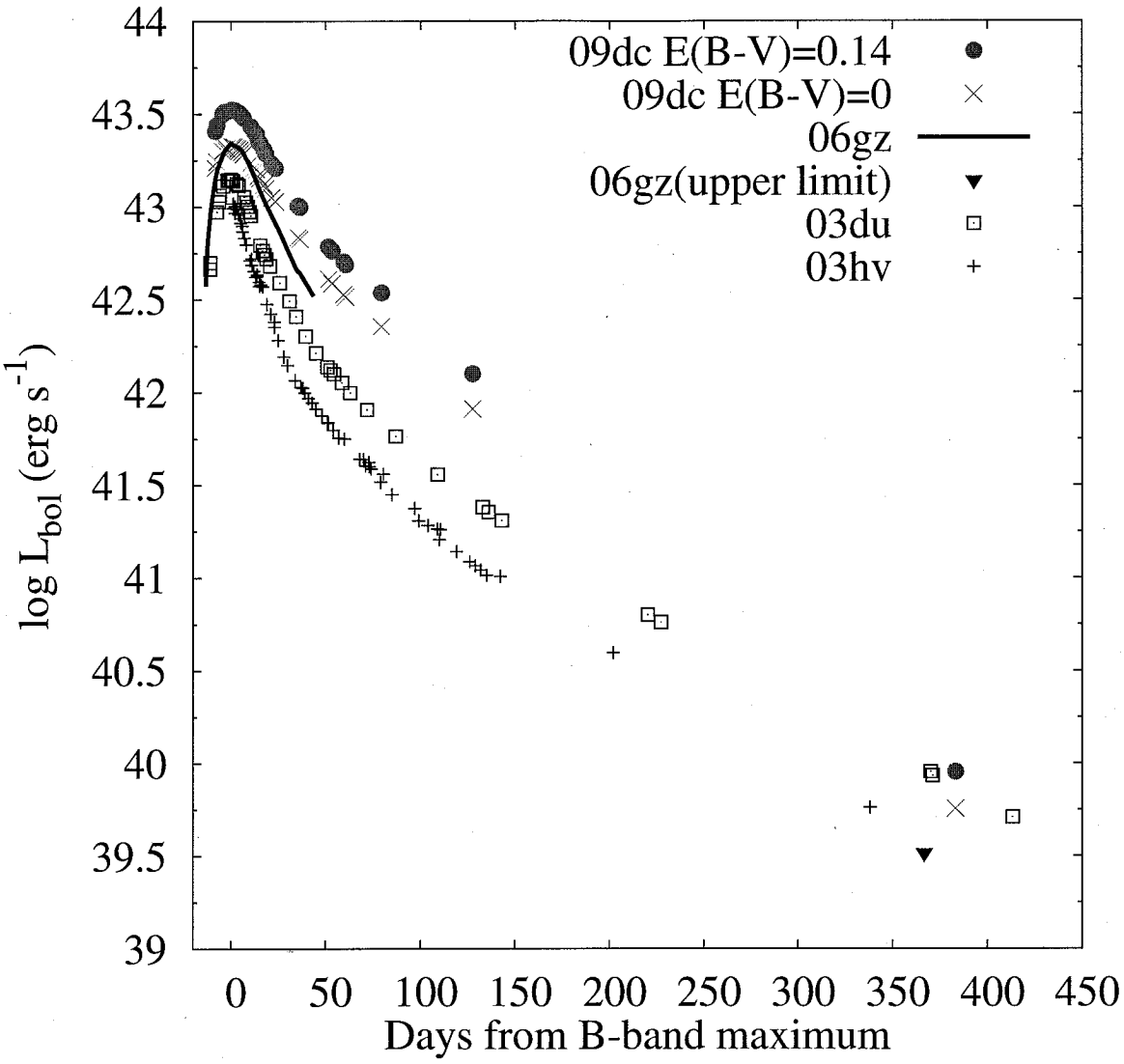

Figure 28: Bolometric light curve of SN 2009dc. Filled circles show the cases of the host extinction $E(B-V) = 0.14$ mag with $R_V = 3.1$ (extinction case 3). The asterisk shows the case with no host extinction (extinction model 1). The bolometric light curves of the normal SNe Ia 2003du (open square; Stanishev et al. 2007), 2003hv (cross mark Leloudas et al. 2009) and the super-Chandrasekhar SN 2006gz (thick line; Hicken et al. 2007) are shown for comparison.

4.5 Spectral Evolution

We present spectral evolution of SN 2009dc in figure 29. Their wavelength are already corrected for the recession velocity of host galaxy UGC 10063.

In figure 30, we compare the spectra of SN 2009dc with those of the super-Chandrasekhar SN 2006gz at -14 days and $+5$ days (Hicken et al. 2007) and the typical SN 2003du (Stanishev et al. 2007) around maximum. The spectra of SN 2009dc near the maximum show Si II λ6355 absorption, a W-shape S II absorption feature and Fe-group multiple absorptions. These features are consistent with the classification as the SNe Ia. Additionally, the absorption line of C II λ6580 is seen, even a few days after the maximum. This feature is seen only in a small fraction of SNe Ia at their earliest epochs (Tanaka et al. 2008). In the super-Chandrasekhar SN 2006gz, the carbon feature also exists; however, the feature is significant only in the earliest stages ($\lesssim -10$ days; Hicken et al. 2007). In another, more distant super-Chandrasekhar SN 2003fg, the C II λ6580 feature is not significant at $+2$ days, while there is a possible carbon feature around 4150 Å at the same epoch. The persistence of the strong carbon feature in SN 2009dc indicates that a massive C+O layer exists in the atmosphere. The Fe multiplet features seen around 5000 Å are slightly different between SN 2009dc and SN 2006gz. The spectral evolution is slow between $+25$ and $+90$ days (figures 31 and 32), being consistent with the slow decline of the light curve.

In figure 33, we show the line velocity of Si II λ6355 together with those in other SNe Ia. The Si II line velocity of SN 2009dc is $\sim$ 8000 km s^{-1} at -4 days and then decreases to $\sim$ 6000 km s^{-1} by $+24$ days. This indicates that SN 2009dc is one of the most slowly expanding SNe Ia (except for faint SNe Ia). The line velocity is much lower than that of SN 2006gz, but comparable with that of another SC SNe Ia, SN 2003fg. (8000 ± 500 km s^{-1} at $+2$ days; Howell et al. 2006). The velocity of the C II λ6580 line in SN 2009dc is a similar to or slightly less than of the Si II line (figure 33). This implies that the Si layer and the C+O layer partly co-exist.

We present the spectrum of SN 2009dc obtained at 383.4 days in figure 35. It is compared with those of SC SNe Ia, SN 2006gz (Maeda et al. 2009) and typical SNe Ia, SN 2003du (Stanishev et al. 2007) at the comparable phase. The spectrum of SN 2009dc exhibits the nebular emission lines of [Fe II] and [Fe III] at 4000 – 5500 Å. The relative strength of this region is much weaker than that of typical SNe Ia, SN 2003du. In SN 2009dc, there is little feature at 5500 – 7000 Å , while SN 2003du shows marginal [Co III] emission lines at 5800 Å and 6400 Å .

In the late-phase spectrum, the double-peaked emission features are seen at 7200 – 7500 Å. We enlarged the spectra in this region in figure 36. The two emission-peaks are located at 7140 Å and 7310 Å, respectively. In most SNe Ia, these features are identified as [Fe II] λ7155 and [Ni II] λ7378 (Elias-Rosa et al. 2006; Kotak et al. 2005; Stanishev et al. 2007; Pignata et al.

2008; Wang et al. 2008). They are possible indicators of geometric structure in the inner part of the ejecta (Maeda et al. 2010b,c).

In SN 2006gz a possibility of blending from [Ca II] to these features is discussed as the case of core collapse SNe (Maeda et al. 2009). In SN 2009dc, we measured the blueshifted velocity of -619 km s^{-1} from the peak at 7140 Å, assuming the emission is [Fe II] λ7155. We can consider the emissions with shoulder structure around 7310Å as a blend of, at least, two emission lines. Assuming these two features are [Ni II] λ7378 and [Ca II] λ7299, we attempt to perform the Gaussian fitting to distinguish these emission lines. First, we fit [Fe II] λ7155 to the emission at 7140 Å and derived the velocity of -600km s^{-1}. Then, using these same velocity and parameters, we successfully fit to the position near the rest of [Ni II] λ7378. This consistency gives us the reasonably identification of these features. We also fit [Ca II] λ7299 to the peak at 7310 Å. This corresponds to the slightly redshifted velocity of -300 km s^{-1}. These results allow us to discuss the difference in the distribution of calcium and iron/nickel in the inner-part of the ejecta.

Recently, Yuan et al. (2010) reported that SN 2007if is another candidate of SC SNe Ia and showed a nebular-phase spectrum at 339 days. The authors suggest that the broad line emission is marginally detected above 7000 Å. This emission line is clearly weaker than that of SN 2009dc. It is rather comparable with that of SN 2006gz (Maeda et al. 2009). Maeda et al. (2009) discussed that [Ca II] is unseen in typical SNe Ia ($\Delta m_{15}(B) \lesssim 1.4$), while this might be a common feature in SC SNe Ia.

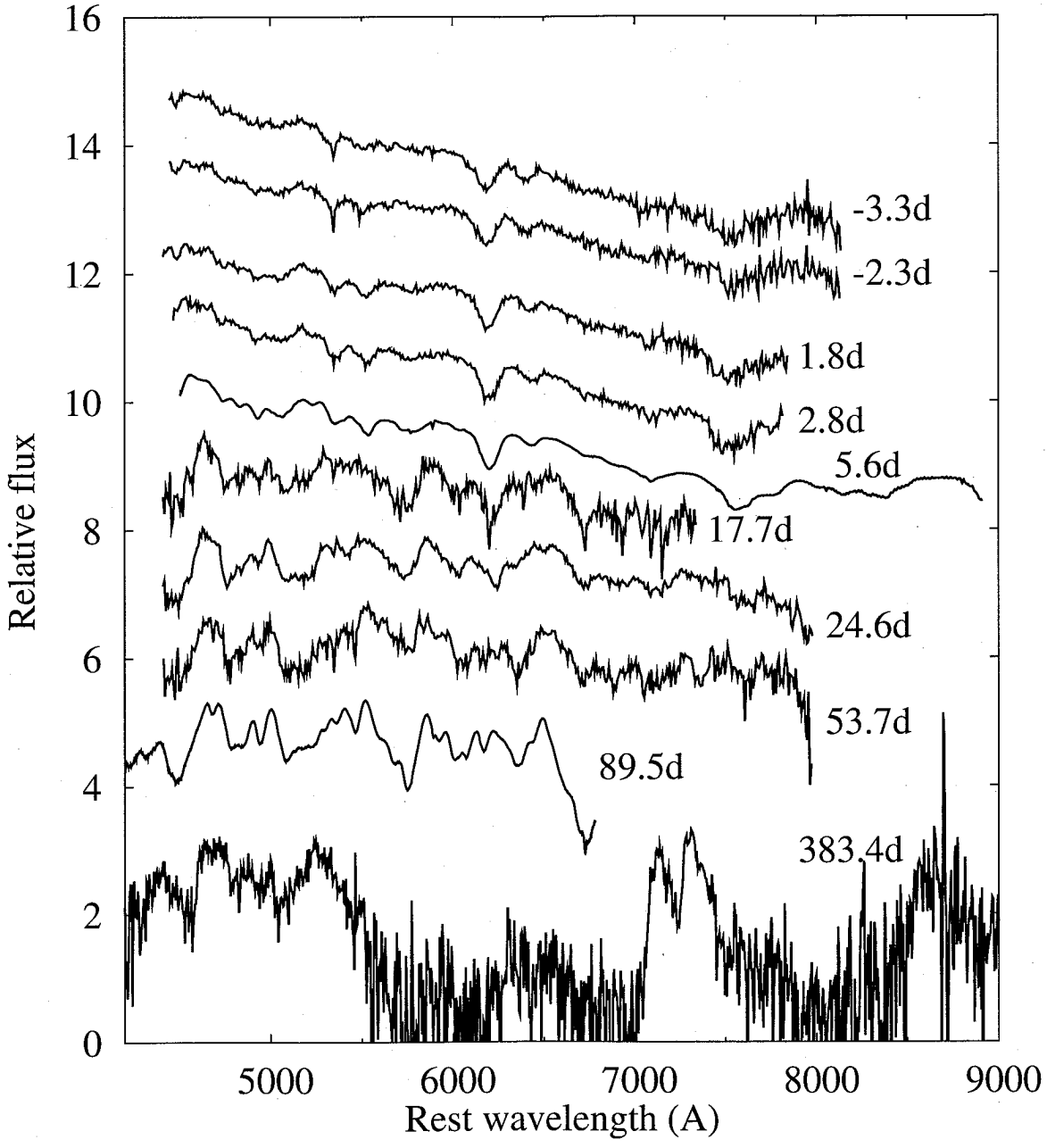

Figure 29: Summary of spectra obtained for SN 2009dc.

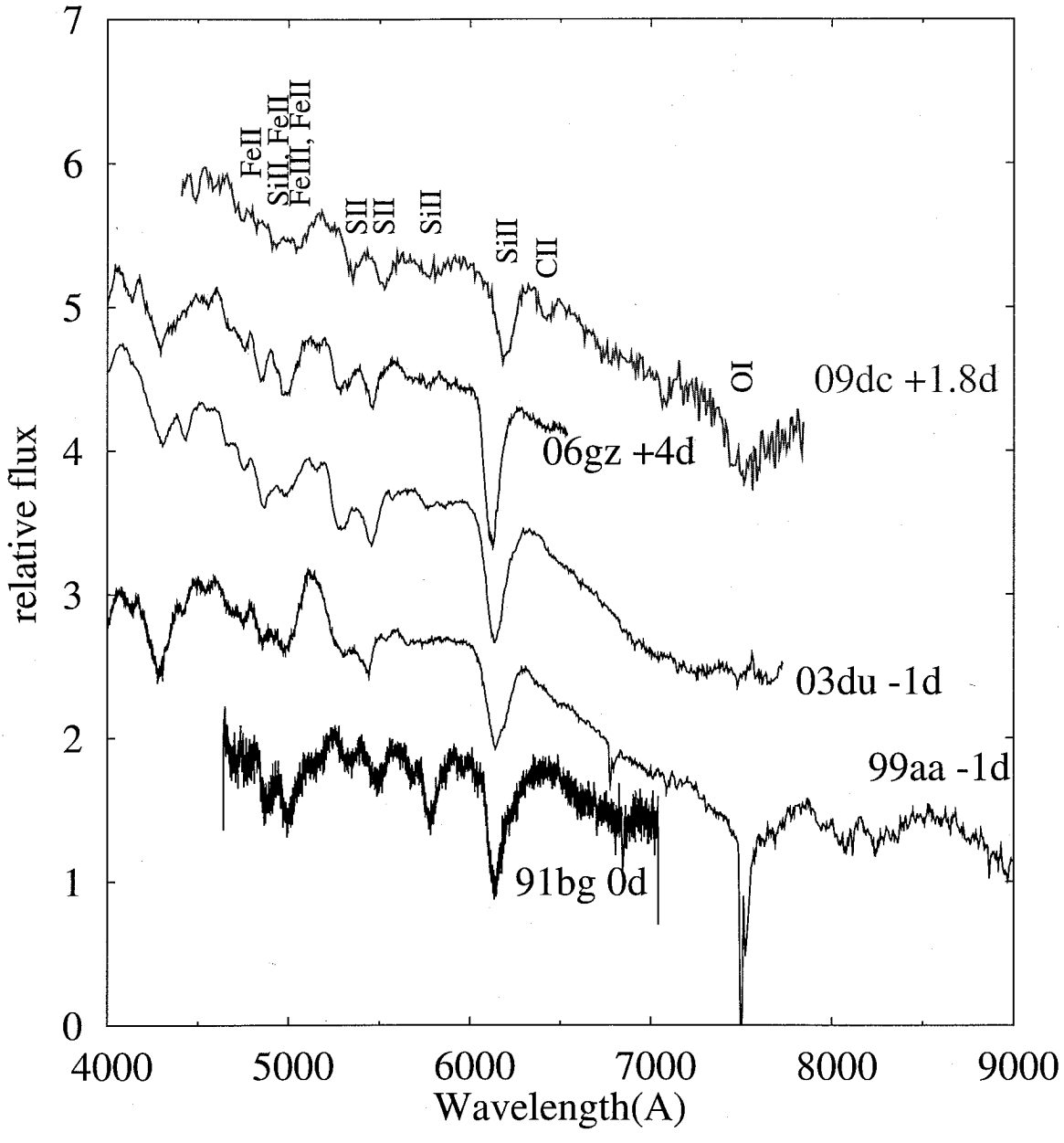

Figure 30: Spectra of SN 2009dc around maximum light compared with those of other SNe Ia; a typical SN Ia 2003du and the super-Chandrasekhar SN Ia 2006gz. The spectrum of SN 2009dc at +5.5 days is from (Tanaka et al. 2010b). The telluric absorption features have been removed for SN 2009dc. The species of each absorption line component is indicated. The existence of carbon feature (CII) is unique for super-Chandrasekhar SNe Ia.

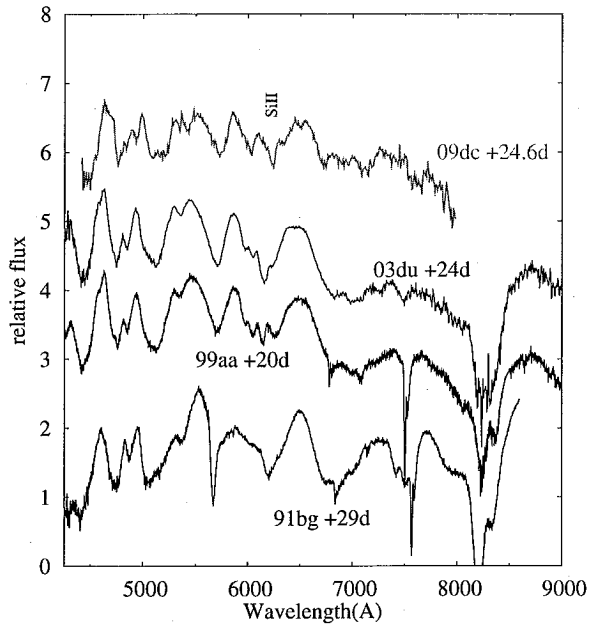

Figure 31: Spectra around +25 days shown in the same manner as figure 30.

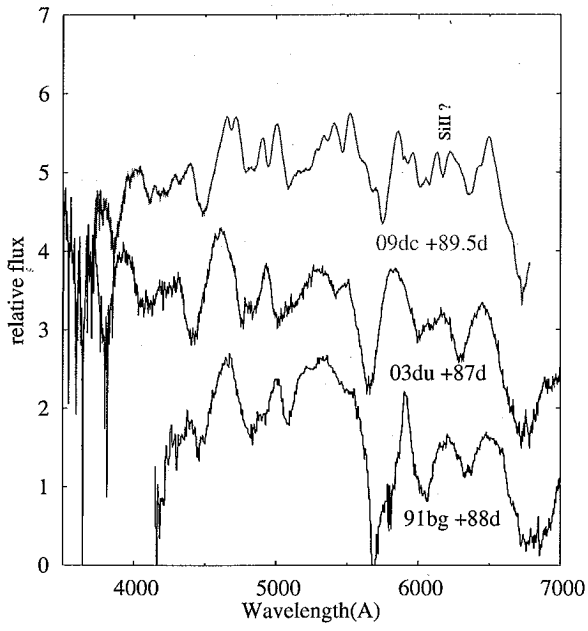

Figure 32: Spectra around +90 days shown in the same manner as figure 30.

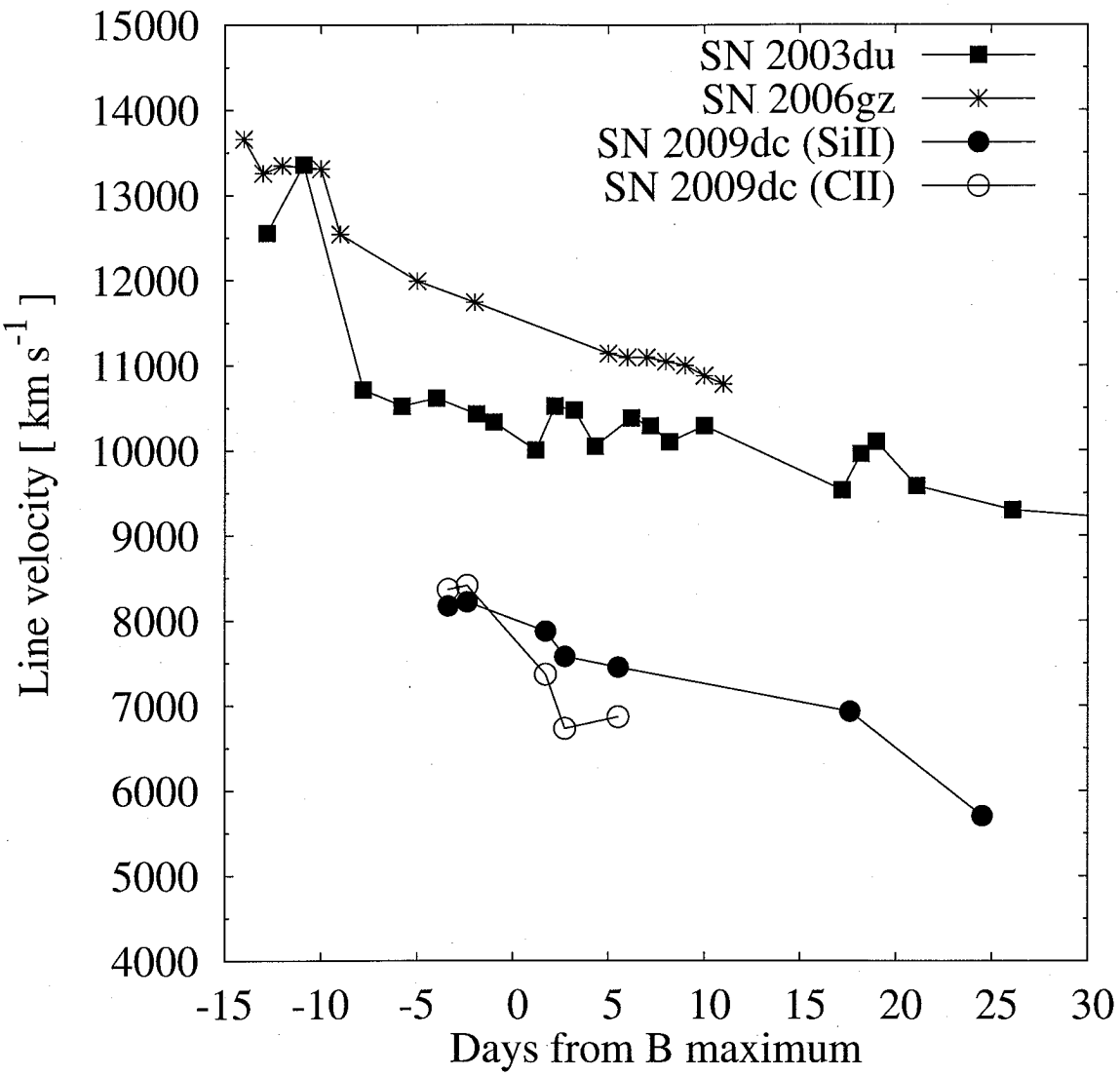

Figure 33: Si II λ6355 line velocity evolution of SN 2009dc and comparative SNe Ia, 2006gz (Hicken et al. 2007), 2003du (Stanishev et al. 2007). We also show the C II λ6580 line velocity of SN 2009dc with black open circles. The low expansion velocity of SN 2009dc is remarkable.

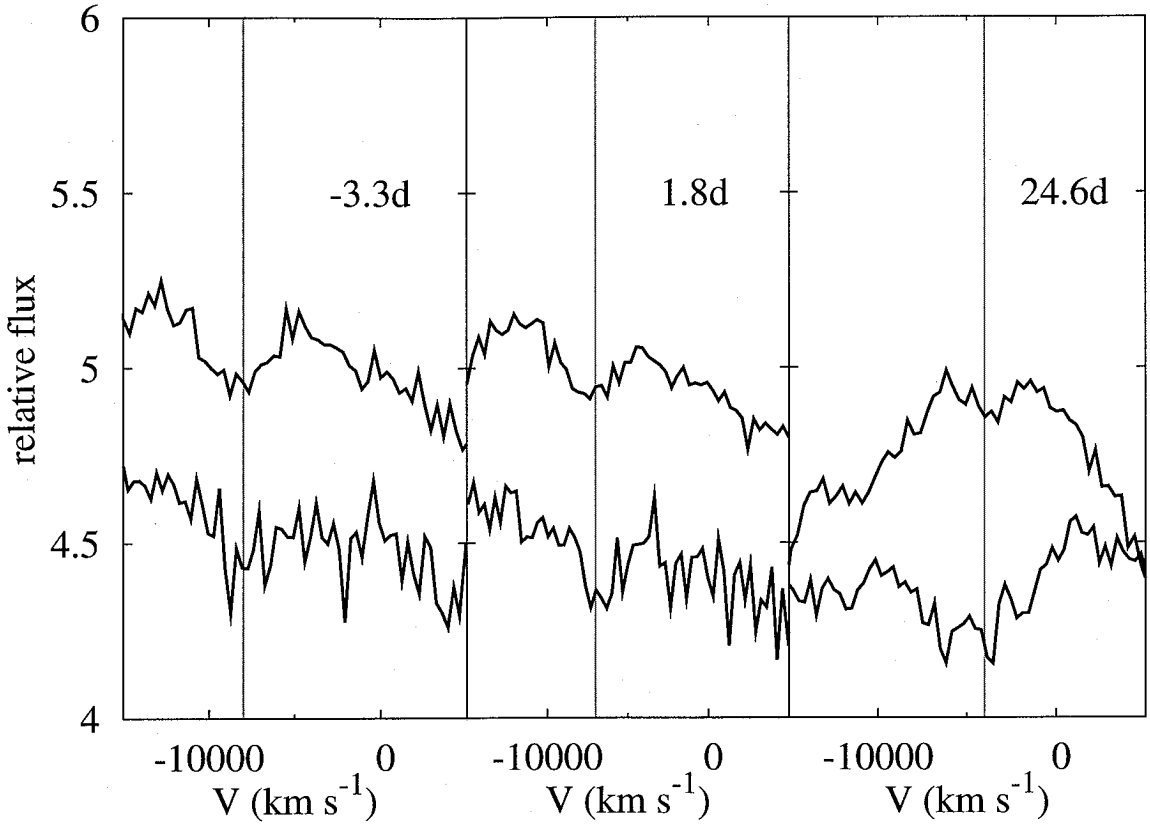

Figure 34: Early variation of C II λ6580 and λ7234 features in SN2009dc. The wavelength has been converted to the Doppler velocity. The negative velocity denotes the blueshift (i.e., approaching us). This figure indicates that the line velocity of these two carbon lines are consistent. This supports that the relatively low-S/N feature around 7230 Å is also really due to carbon.

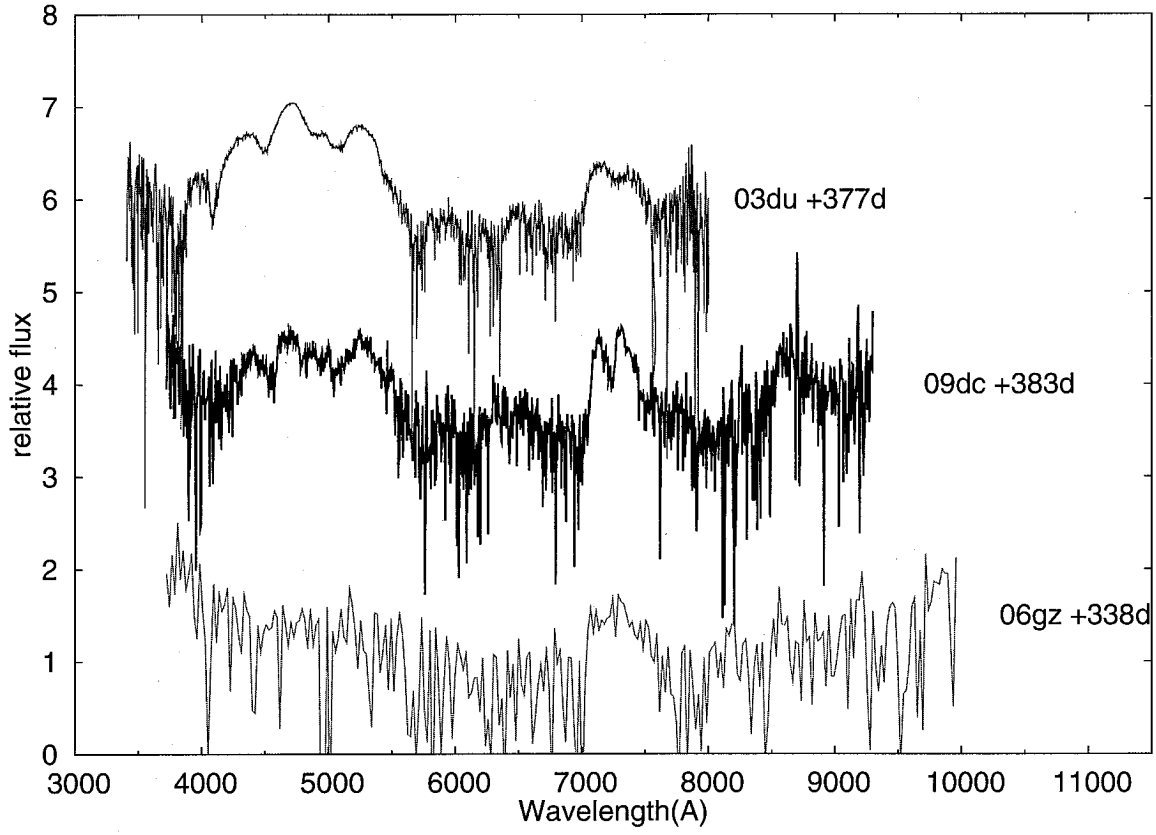

Figure 35: Spectrum obtained at 383.4 days compared with those of typical SN Ia 2003du (Stanishev et al. 2007) and SC SN Ia 2006gz (Maeda et al. 2009). The epochs are determined based on Anupama et al. (2005) and Hicken et al. (2007) for SNe 2003du and 2006gz, respectively. The horizontal axis denotes the rest wavelength. The recession velocity of the host galaxies are from NED (http://nedwww.ipac.caltech.edu/).

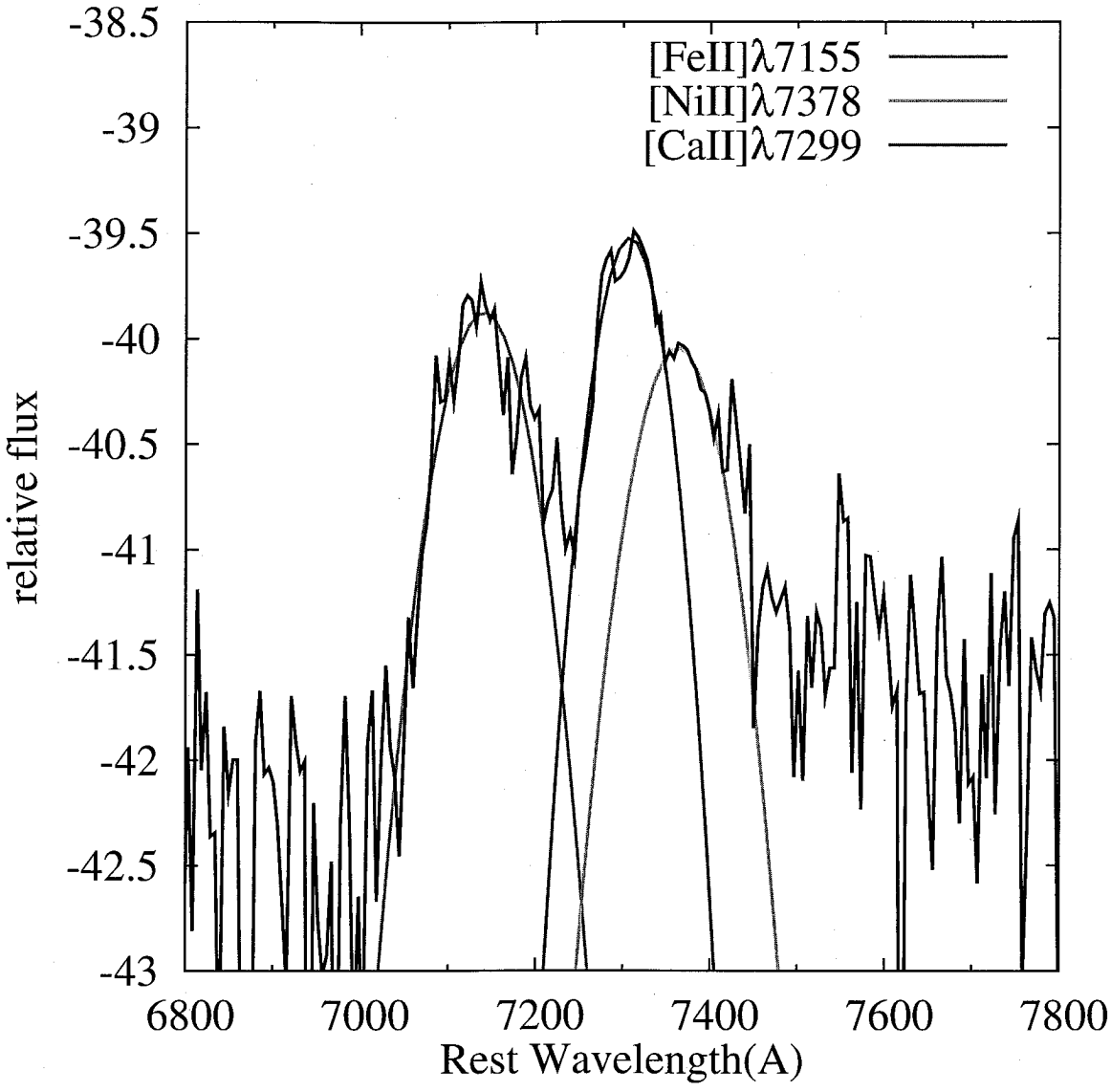

Figure 36: The double-peaked features at 7200 – 7500 Å deblended by three Gaussian functions. Since the red peak has a shoulder in the red wing of the profile, we performed deblending with three components. We identified them as [Fe II] λ7155 (red), [Ca II] λ7299 (blue) and [Ni II] λ7378 (green). Their center wavelength suggest that the iron-group features, [Fe II] λ7155 and [Ni II] λ7378 both show line velocity of -600 km s^{-1}. On the contrary, the intermediate-mass element [Ca II] λ7299 shows a positive velocity, $+300$ km s^{-1}.

5 Discussion

We have obtained a comprehensive data set of SN 2009dc. Those data has a much better quality and quantity among the ever-discovered super-Chandrasekhar mass SNe Ia. Here we discuss the observational aspects and the progenitor candidate, mainly on the large luminosity in early phase and rather normal one in the phase, combined with the spectral properties.

5.1 Peak Luminosity and ^{56}Ni mass

The luminosity of a SNe Ia is originated from γ-rays and positrons from the decay chain $^{56}\mathrm{Ni} \rightarrow {}^{56}\mathrm{Co} \rightarrow {}^{56}\mathrm{Fe}$ as explained in §1.1.2 Therefore, the mass of ejected ^{56}Ni can be estimated from the peak luminosity (Arnett 1982). Stritzinger & Leibudgut (2005) suggested that the ^{56}Ni mass depends approximately on the peak bolometric luminosity and its rising time (t_r days; the time taken to reach the maximum light from the onset of explosion), as

$$L_{\max} = \left(6.45\ e^{\frac{-t_r}{8.8\mathrm{d}}} + 1.45\ e^{\frac{-t_r}{111.3\mathrm{d}}}\right)\left(\frac{M_{\mathrm{Ni}}}{M_\odot}\right) \times 10^{43}\ \mathrm{erg\ s^{-1}}. \quad (5)$$

The slow evolution of brightness in SN 2009dc around the maximum suggests that the rising time of the bolometric luminosity is comparable to or slightly longer than those of SN 2006gz ($\sim$ 18.5 days; Hicken et al. 2007) or typical SNe Ia ($\sim$ 19 days; e.g., Conley et al. 2006). Assuming $t_r = 23$ days for SN 2009dc (Silverman et al. 2010), we derive the ^{56}Ni mass of $1.3 \pm 0.3\ M_\odot$ for no host extinction case. It reaches $2.0 \pm 0.5\ M_\odot$ if we assume the host extinction of $E(B-V) = 0.14$ mag and $R_V = 3.1$ (extinctions model 3; table 4). Although the derived $L_{\max}$ and the ^{56}Ni mass still include some uncertainties, our observation suggests that the total mass of the progenitor might exceed the Chandrasekhar-limit one.

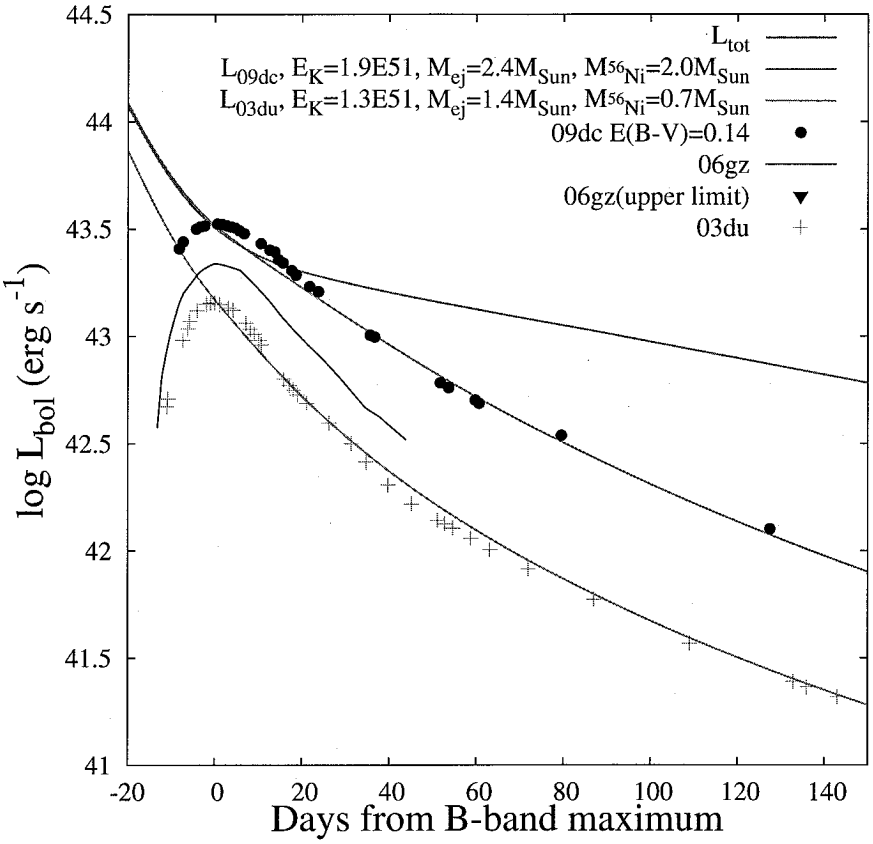

Figure 37: The quasi-bolometric light curve of SN 2009dc compared with those of typical SN Ia 2003du and another SC SN Ia 2006gz until 150 days. These bolometric light curves are calculated only from optical band data (thus, we call 'quasi-bolometric'). It is assumed the optical contributions of constantly 60% against intrinsic bolometric luminosity. It is assumed that the optical light constantly contributes to 60% of the bolometric luminosity. In SN 2009dc, both host galactic extinction corrected and no-corrected light curves are plotted. In SN 2009dc, the data in two extinction models (1 and 3) are plotted. For SN 2006gz, the extinction is corrected for based on the value derived by Hicken et al. (2007). For SN 2003du, the extinction is assumed to be zero. The red line denotes the full γ-ray deposition energy (i.e., total emitted energy) from a decay of the 2.0 $M_{\odot}$ ^{56}Ni mass. Other two curves are an analytic light curve models which are constructed from a model for the total ejected mass of $2.4M_{\odot}$ and kinetic energy of 3.5×10^{51} erg s^{-1} (§5.2.1 for details). The pink curve shows the case that positrons are fully-trapped by the ejecta, which is usually good approximation for SNe. This curve well reproduces the bolometric light curve of SN 2009dc after the maximum. In order to check the application of this analytic model, We also constructed a curve reproducing that of SN 2003du shown in the gray line. These analytic models successfully explain the light curves of both 2009dc and 2003du, at least, until 140 days.

5.1.1 Light Curve Model and Expected Progenitor Model

We construct an analytic light curve based on toy models (Arnett 1982, See also Maeda et al. (2003); Valenti et al. (2008)). The luminosity is expressed as,

$$L(t) = M_{^{56}\mathrm{Ni}}(S_{^{56}\mathrm{Ni}}(t) + S_{^{56}\mathrm{Co}}(t))(1 - e^{\tau} + 0.035 f_{\mathrm{p}}), \tag{6}$$

where the deposition energy of γ-ray from ^{56}Ni and ^{56}Co decays are expressed as

$$S_{^{56}\mathrm{Ni}}(t) = 3.90{\times}10^{10} e^{-t/t_{^{56}\mathrm{Ni}}} \tag{7}$$

$$S_{^{56}\mathrm{Co}}(t) = 7.01{\times}10^{9} (e^{-t/t_{^{56}\mathrm{Co}}} - e^{-t/t_{^{56}\mathrm{Ni}}}). \tag{8}$$

τ is the optical depth of γ-ray against the ejecta. Since it decreases with time, we express as,

$$\tau = 1000 (M_{ej}/M_{\odot})^{2} \cdot E_{\mathrm{K}\cdot 51}^{-1} \cdot t^{-2}. \tag{9}$$

f_{p} is the positron trapping fraction, in which we adopt the $f_{\mathrm{p}} = 1.0$ in full trapping. The lifetimes of a radioactive nickel and cobalt are given as $t_{^{56}\mathrm{Ni}} = 8.8$ and $t_{^{56}\mathrm{Co}} = 113.5$ days, respectively. $E_{\mathrm{K}\cdot 51}$ is the kinetic energy in the unit of 10^{51} erg. First, we attempted to fit this model to normal Type Ia SN. The curve fitted to SN 2003du (Stanishev et al. 2007), with $M_{\mathrm{ej}} = 1.4 M_{\odot}$, $E_{\mathrm{K}} = 1.3 \times 10^{51}$ erg and $M_{^{56}\mathrm{Ni}} = 0.68\ M_{\odot}$ (Tanaka et al. 2010a), is shown in figures 37 and 38. These figure show that this model well represents the observation for a typical SNe Ia. We examine the light curve of SN 2009dc with this model. As a result, we can well fit the analytic light curve to that of SN 2009dc until 150 days after the B-band maximum for $M_{ej} = 2.4 M_{\odot}$ [6], $M_{^{56}Ni} = 2.0 M_{\odot}$ and $E_{\mathrm{K}} = 1.9 \times 10^{51}$ erg. However, after 350 days, this model cannot explain the observation. That is, the luminosity exceeds the conservative lower-limit of luminosity in which the energy source is only the full trap of positrons in ^{56}Co decay (blue line in figure 38).

Scalzo et al. (2010) discussed that the high peak luminosity is possibly caused by circumstellar material (CSM) interaction with its ejecta for another SC SN 2007if. If the ejecta interacts with CSM, strong emission lines should appear in early-phase spectra, as SNe IIn. However, we could not detect any significant emission lines in the spectra of SN 2009dc. We also show that the early-phase light curves could be explained by ^{56}Ni decay using simple light curve fitting model.

Alternatively, we can calculate the kinetic energy from the ejected mass and the expansion velocity. Yamanaka et al. (2009a) found that the line velocities of Si II and C II of SN 2009dc

[6] Kamiya et al. (2010) estimated the ejected mass of $2.4 M_{\odot}$ from the theoretically fitting to multicolor light curves based on their radiative transfer calculation. This mass is upper limit of the total ejected mass under the realistic condition.

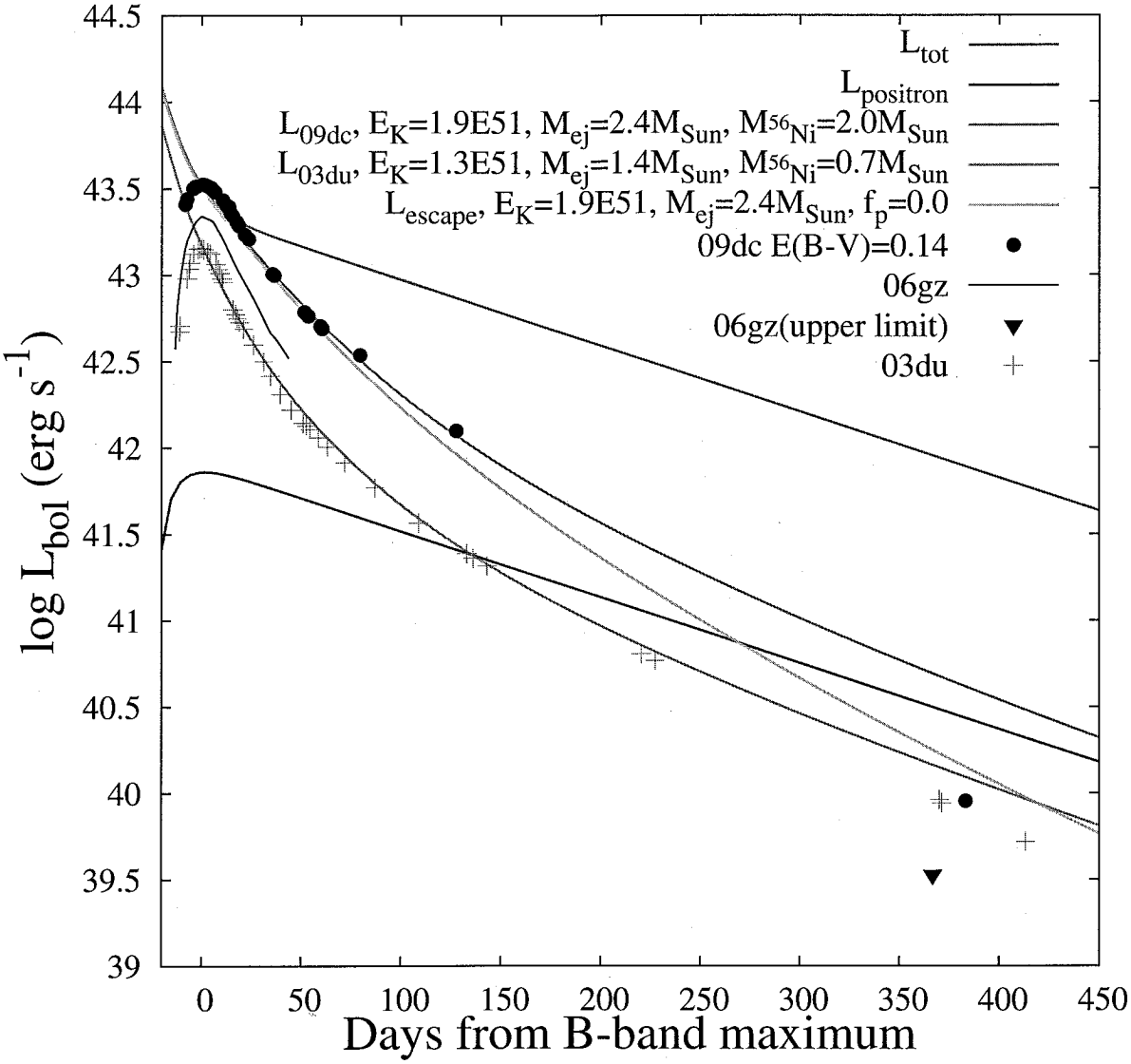

Figure 38: The quasi-bolometric light curve up to 400 days. The symbols are shown in the same manner as figure 37. The red line denotes the full γ-ray deposition from the decay of 2.0 $M_{\odot}$ ^{56}Ni. The blue line shows the luminosity component from the full trap of positrons from ^{56}Co decay, which may indicate the conservative lower-limit of the bolometric luminosity. Analytic light curve models are constructed with the total ejected mass of $2.4M_{\odot}$ and kinetic energy of 3.5×10^{51} erg s^{-1}. The pink curve denotes the case of fully positron trapping and the aqua one the case of no trapping for positron. In order to check the application of analytic fitting, We also constructed the fitting curve to that of typical Ia SN 2003du denotes in gray line. The faint luminosity of SN 2009dc after 350 days cannot be easily explained by our analytic model.

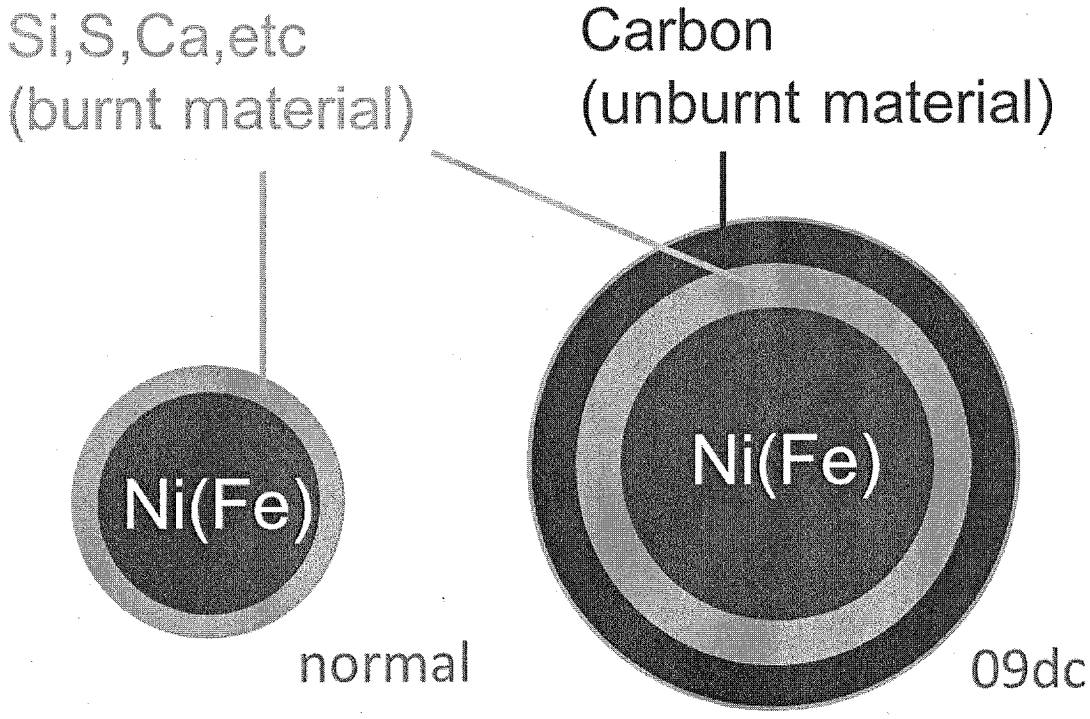

Figure 39: Schematic picture of layered structure of SN2009dc compared with that of a normal SN Ia. SN 2009dc has the large ejected ^{56}Ni mass ($\sim 2.0 M_{\odot}$), thick silicon and carbon layer. A normal SN Ia would not have such a thick carbon layer, as expected from little or no carbon lines seen.

are 8000 km s^{-1} at the maximum. From the $M_{\rm ej} = 2.4 M_{\odot}$ and the expansion velocity of 8000 km s^{-1}, the kinetic energy is calculated as $E_{\rm K} = 1.5 \times 10^{51}$ erg. This value is roughly consistent with that expected from the light curve model. We successfully reproduced the light curve of SN 2009dc up to 150 days with the analytic light curve model for normal SNe Ia; however, the observed luminosity rapidly decreases after 200 days, which cannot be explained by the model. We discuss the origin of this in the next subsection.

These results support that SN 2009dc has large ejected mass ($\sim 2.4 M_{\odot}$), which clearly exceeds the Chandrasekhar-limiting mass of a non-rotating white dwarf. Early-phase spectra exhibit deep carbon features until a week after the B-band maximum, indicating a thick carbon layer existing in the outermost ejecta (see figure 34). Spectropolarimetric observation indicated low polarization degree of the continuum and relatively high polarizations degree of Si II absorption line, which indicates the explosion is nearly spherical in bulk and the silicon layer is inhomogeneous and rather thick (Tanaka et al. 2010b). This excludes the model in which

the explosion is highly aspherical and the observational properties do not necessarily require large ejecta mass. As a consequence, our observation suggests that the progenitor would have extremely large mass compared with that of a SNe Ia (figure 39).

5.2 Origin of Rapid Fading

We observed that the luminosity of SN 2009dc was much fainter at 383 days than that expected from its high peak luminosity. We consider two hypotheses: one is that SN 2009dc is too luminous in early phase and the other is that it is too faint in late phase.

5.2.1 Dust Formation

In §4.2, we noted that SN 2009dc exhibit redder $V - I_C$ color in late-phase compared with a typical SN Ia. Additionally, a rapid drop of the luminosity in optical wavelength is remarkable when we compare it with the analytic light curve model which well reproduces the early-phase light curve. Taubenberger et al. (2010) confirmed the strong C II absorption in their spectra until two weeks after B-band maximum. The existence of strong C II absorption line in the early spectra is one of the characteristics of SN 2009dc (§4.5). Taubenberger et al. (2010) reported that the C II line survived until two weeks after the B-band maximum. The authors also confirmed the CO molecular line at 84.3 days in near-infrared spectra.

We propose the possibility of dust formation. The wavelength-dependent extinction due to dust grains is consistent with the redder color in the late-phase. The carbon-rich atmosphere is likely produce carbonaceous dust grains after the atmosphere is cooled as expansion. The carbon-rich atmosphere is reported in the nearby core-collapse SNe Ic, SN 2007gr, which also shows strong C I and CII features in their early-phase spectra (Valenti et al. 2008). Although Hunter et al. (2009) tried to seek the evidence of dust formation in SN 2007gr, they cannot find any sign. If the dust forms in the ejecta, the emission originated from the inner region and the other side is selectively hidden. Therefore, the emission line is expected to exhibit an asymmetric profile where the red wing component becomes weaker. We show the emission line of SN 2009dc and comparative SNe at 7200–7500 Å (figure 36). The spectra rather exhibit the extended components to red-shifted skirt of the emission line profile for [Fe II] and [Ni II] (strongly contaminated by [Ca II]). This is inconsistent with a model that the dust formation occurred in the inner part. Thus, if the dust formation is really occurred, it should be in the outer ejecta.

The carbon dust is one of the primary components in universe. Though it is unclear where

the dust forms in, supernova is one of the possible candidates for dust formation. Several core collapse SNe products the large amounts of dust, like SN 2006jc (Di Carlo et al. 2008; Nozawa et al. 2008). However, there is still too small rate of events for explaining the amount dust in universe. We confirmed the possibility of carbon dust formations in ejecta of SN 2009dc. Super-Chandraksekhar SNe may become one of the dust formation stations.

We cannot find any evidence of dust formation for SN 2009dc in late-phase spectrum. If the dust formation really occurred, an increase of thermal emission is expected in infrared wavelengths accompanied with optical decline. At this time we do not have any late-phase infrared observation for SN 2009dc. We should test it for next SC SN Ia candidate in the future. In the following, we briefly discuss other possibilities to explain the low luminosity in late-phase.

5.2.2 Positron Escape

We plotted the analytic curves for $M_{ej} = 2.4M_{\odot}$ and $E_K = 1.9 \times 10^{51}$ erg ignoring the positron trapping, assuming $f_{\rm p} = 0.0$ in the equation (6) in figure 38. Our positron escape model predicts a bit luminous than the faint luminosity of SN 2009dc at late-phase. Several authors discussed the positron escape in inner-part ejecta for SNe Ia (Ruiz-Lapuente & Spruit 1998; Milne et al. 1999; Sollerman et al. 2004; Stritzinger & Sollerman 2007; Leloudas et al. 2009). If this is the case, the low luminosity could be marginally explained. Milne et al. (1999) suggests that the SNe Ia except of SN 1991bg do not require the positron escape in inner-part ejecta for the explaining late-phase decline of the light curves.

5.2.3 IR Catastrophe

In the standard theoretical model of SNe Ia (W7 model), the infrared catastrophe (IRC) will occur after 500 days (Nomoto et al. 1984). Once IRC occurs, the peak wavelengths shifts to longer wavelength due to rapid decrease of temperature in ejecta. We should see a rapid drop of the optical flux with the increasing mid-infrared flux. Leloudas et al. (2009) point out that IRC occurs in higher density regions in their clumpy ejecta model.

SN 2009dc exhibits the slower evolution in luminosity and spectral profile, at least, until 120 days (Yamanaka et al. 2009a; Silverman et al. 2010; Tanaka et al. 2010b; Taubenberger et al. 2010). Thus, we can assume that the inner region had higher density than that of a typical SN Ia. This follows IRC occurrence at earlier phase than that predicted in the W7 standard model. If IRC occurs in ejecta of SN 2009dc, the ^{56}Ni mass may be underestimated from only optical late-phase luminosity, because the peak of the spectral energy distribution shifts to longer

wavelength. This will lead to fainter luminosity in the estimated bolometric one, because our assumption of the optical luminosity fraction versus bolometric luminosity breaks.

5.2.4 Explosion Models

We find the blend of [Ni II] and [Ca II] lines at blueshift of 600 km s^{-1} and rest frame, respectively, in the spectrum at 383 days. This indicates that the calcium would distribute in inner regions than iron group elements. Such a situation cannot be reproduced by the recent models which predict rather stratified layer in ejecta of SNe Ia. Mixing into inner layer may occur in the explosion of SN 2009dc. [Ca II] is possibly identified in the spectrum of SN 2006gz. Calcium may commonly distribute in inner-layer than iron group in SC SNe Ia. Since identification of [Ca II] is also discussed for 91bg-like and fainter objects (Maeda et al. 2010c), it may give us a hint to discuss about the explosion pictures of SC SNe Ia. Maeda et al. (2010a) studied a nucleosynthesis of SNe Ia based on the two-dimensional hydrodynamical delayed detonation model. Their off-center ignition model indicates the stratified layer and non-mixing intermediate mass elements (e.g. ^{28}Si, ^{32}S, ^{40}Ca). This does not support the calcium concentration near the core in SN 2009dc. The mixing of synthesized material into inner layer may occur in SN 2009dc unlike stratified structure typically seen in SNe Ia (Stehle et al. 2005; Mazzali et al. 2008; Tanaka et al. 2010a). On the other hand, Bravo & García-Senz (2008) suggested that their three-dimensional delayed detonation model reproduces well mixed material in the whole ejecta; however, synthesized only small amount of ^{56}Ni mass, below 0.7 $M_{\odot}$ because of its relatively stronger deflagration burning than a detonation. From these speculations, deflagration in inner region would be rather stronger than detonation wave for SN 2009dc, though the white dwarf requires larger mass.

On the other hand, we observed a rather flatter secondary maximum in the $I_{\rm C}$-band light curve of SN 2009dc comparing with that of normal SNe Ia. Kasen (2006) indicated that the secondary maximum in $I_{\rm C}$-band in SNe Ia would be correlated to the mass of iron group elements. This indicates that the strong mixing of iron group elements might occur in the outer layer of SN 2009dc. Maeda et al. (2010a) indicates the mixing of C-O material and IMEs into outer layer above 12000 km s^{-1} on their all models. The Si II velocity of SN 2009dc is comparable of that of C II at early phase (Yamanaka et al. 2009a; Taubenberger et al. 2010). This fact may support that the mixing would occur in the outer layer.

5.3 Progenitor Candidates

We suggest that the total ejected mass of SN 2009dc would be more than $2.0M_{\odot}$. This mass is clearly larger than the Chandrasekhar-limiting mass with non-rotating white dwarf. In order to reproduce this large mass in a SN Ia, there are mainly two progenitor models in recent studies.

Rapidly-rotating white dwarf can grow up its mass because the centrifugal force supports the degenerate pressure in inner-part of white dwarf (Uenishi et al. 2003; Yoon & Langer 2005). Yoon & Langer (2005) suggest that its mass should increase up to $2.0M_{\odot}$ until carbon ignition begin in central region. Pfannes et al. (2010) performed the hydrodynamic calculation of thermonuclear detonation using this large white dwarf mass. They indicates that their explosion could reproduce the large ^{56}Ni mass of $1.5M_{\odot}$, which is rather consistent with $1.3M_{\odot}$ derived by our observations in the case of assuming the non-extinction. Moreover, the unburnt carbon material successfully remain in outermost layer. This also supports that the carbon absorption lines are seen in spectra. This model seems to explain observational properties of SN 2009dc. However, it is unknown how process form the extremely rapid rotation of white dwarf in binary evolution. Such objects are still not discovered in our Galaxy.

Another candidate is a double degenerate model (Webbink 1984; Iben & Tutukov 1984). The two white dwarf merges and explode. Saio & Nomoto (1985) indicates that the merger predicts rather accretion induced collapse than thermonuclear runaway. However, recent study suggests that the merger of equal-mass ($\sim 0.9M_{\odot}$) white dwarfs successfully drive the deflagration burning and delayed detonation (Pakmor et al. 2010). This model reproduces the light curves and spectra of subluminous SNe Ia. The ^{56}Ni mass is synthesized as $0.1M_{\odot}$. This is inconsistent with that of SN 2009dc and other luminous SNe Ia. Though there is no merger models to explain the extremely high luminosity, the total mass of two white dwarf easily exceed $1.4M_{\odot}$. Double degenerate systems are certainly found in Galaxy. Future theoretical study may discover the solution to reproduct very large ^{56}Ni mass.

6 Conclusions

We summarize the observational characteristics of the peculiar SN Ia 2009dc at early phase as follows: (1) one of the slowest evolving light curve ($\Delta m_{15}(B) = 0.65 \pm 0.03$), (2) one of the most luminous SNe Ia ($M_V = -19.90 \pm 0.15$ or brighter), (3) a strong carbon feature in the early spectra, and (4) the lowest expansion velocity among extremely luminous SNe Ia. The first three features are similar to another super-Chandrasekhar SNe, SN 2006gz, while the last item is clearly different. Although the detailed data for the distant super-Chandrasekhar candidate SN 2003fg are lacking, the expansion velocity of SN 2003fg is likely comparable with to that of SN 2009dc. If the ejecta is strongly aspherical, the amount of ^{56}Ni could be reduced (e.g., Sim et al. 2007). However, the polarization measurement indicates that the photosphere is almost symmetric along the line of sight (Tanaka et al. 2010b). We also successfully fit an analytic model to bolometric light curve until 150 days. It suggests that the early-phase luminosity is likely originated from the ^{56}Ni decay for the first half year and then declines probably due to an additional cause. Thus, SN 2009dc is much likely a SN Ia explosion with a super-Chandrasekhar mass WD. A super-Chandrasekhar mass WD has been expected for a rapidly-rotating WD (e.g, Kamiya et al. 2010 and references therein).

We also performed late-phase observations of this SN at a year after discovery. We observed rather fainter luminosity than expected from the high luminosity at early-phase. The color index $V - I_C$ also exhibits the much redder color comparing with that of a typical SN Ia. To satisfy these facts, we propose that the opacity of the inner-part ejecta could be increased by formation of dust grains. This scenario is consistent with the carbon-rich atmosphere indicated by the early-phase spectra, because of the carbon is one of the dominant elements in the cosmic dust. However, this is not a unique scenario because there is any direct evidence of dust formation (e.g., brightening in infrared wavelength) so far. We discussed other possible scenarios for the decline in the late-phase. As future works, the near-infrared observations at a year after explosion for super-Chandrasekhar SNe may give us a constraint on the low-temperature radiation by dust. Alternatively, I will perform the optical imaging observations using Subaru telescope with FOCAS at two years after explosion. If the dust clear up at line-of-sight of supernova, the photon flux can be detected in optical wavelength.

We confirmed that the emission line at 7300 Å would be a result of a blend of [Ni II] λ7378 and [Ca II] λ7299. It suggests that the intermediate-mass elements like calcium distribute even in the inner-part of the ejecta. The profile is sharply-peaked and clearly different from the flat-topped profile seen in the near-infrared regions of SN 2003hv (Motohara et al. 2006; Gerardy et al.

2007; Leloudas et al. 2009). This fact indicates that the strong mixing might occur in inner-part ejecta. However, in order to reproduce such situation, the relatively strong deflagration wave is required. Although most of the observational facts on this extremely luminous SN Ia can be explained by super-Chandrasekhar white dwarf, several aspects could not be explained and we should improve the explosion model in the future.

Appendix

A. 1 Type Ia Supernova in Cosmological Study

SNe Ia are used as a powerful tool for cosmological study (Riess et al. 1998; Perlmutter et al. 1999). Its utility is well described in (Howell 2010). When we obtain the light curves of SNe Ia, we can derive the peak magnitude (m), the decline rate ($\Delta m_{15}(B)$) and the color index ($B-V$). From these observational parameters, we construct the equation as below,

$$\mu = m - M + \alpha(1/(\Delta m_{15}(B) - 1.1)) - \beta c. \tag{10}$$

Here, μ means the distance modulus (luminosity distance to host galaxy). α means the slope of the width-luminosity relation. β is the slope of the dust extinction versus color index (as the selective extinction parameter, R_V). M is an absolute magnitude in $\Delta m_{15}(B)$= 1.1, which is a typical value of SNe Ia. It is assumed that the these values and Hubble constant are not variable with time. Finally, we can derive the μ and its observational redshift. We can construct the Hubble diagram to an observationally limiting distance of SNe Ia (Astier et al. 2006; Wood-Vasey et al. 2007, ;see figure 40).

If the universe is "flat", the universe expands homogeneously. However, recent observational study of distant SNe Ia predicts rather the the acceleration of the expansion after a certain redshift, which is explained by fact that the distance modulus to SNe Ia is relatively larger than expected from its redshift in the Hubble diagram (figure 40). This is independently confirmed by the study of the cosmic microwave background (CMB) for 3K black body radiation observations by Wilkinson Microwave Anisotropy Probe (WMAP) (Komatsu et al. 2010).

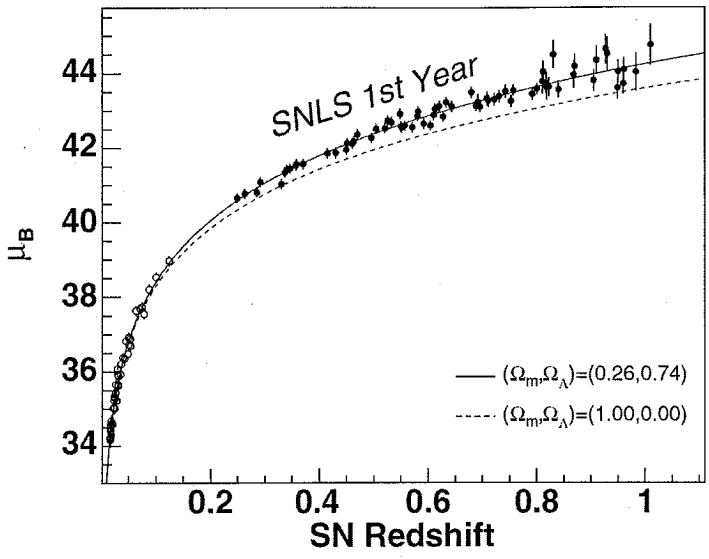

Figure 40: The recent results of diagram from SuperNova Legacy Survey (SNLS) are plotted and cited from Astier et al. (2006). The acceleration expansion of universe significantly seems to be affected at redshit z=0.4. The dashed lines are assumed to be a homogeneity expansion universe.

A. 2 Detailed procedure of PSF photometry

First, we obtain the column and line position of these stars using IRAF task `imexamine` and performed the aperture photometry using `phot` and make *magfile*. We choose the several stars using `psf` command in order to make the PSF function by fitting. The function type is automatically selected from following six ones to make the residual smallest.

- **gauss**, a 2D elliptical Gaussian function aligned along the x and y axes of the image. Gauss is generally the best choice for well-sampled, fwhmpsf $\gtrsim$ 2.5 pixels.
- **moffat25** and **moffat15**, elliptical Moffat functions of beta 2.5 and 1.5, respectively which can be aligned along arbitrary position angle. The Moffat functions are good choices for under-sampled data.
- **lorentz**, an elliptical Lorentz functions which can aligned along an arbitrary position angle. The Lorentz function is a good choice for old space telescope data since it has.
- **penny1**, a two component model consisting of an elliptical Gaussian correction which can be aligned along an arbitrary position angle and lorentzian wings aligned along z and y axes of the image. The Penny1 function is a good choice for a purely analytic psf model.
- **penny2**, a two component model consisting of an elliptical Gaussian correction which can be aligned along an arbitrary position angle and lorentzian wings aligned along an arbitrary position angle which may be different from that of the core. The Penny2 function is a good choice for a purely analytic psf model

After we make the group file using `group` command, we performed the *nstar* task for fitting the PSF model to the object and comparison stars. To check the whether PSF fitting is successfully carried out, it is better to perform the *substar* command. The star subtracted images is made as fits file. If the object and comparison star is unsuccessfully subtracted, we should change the parameters of aperture, FWHM and sky regions size of *psf*.

We check the residual magnitude between aperture and PSF fitting photometry in R_C-band (figure 41). We confirmed that the magnitude measured by aperture photometry is slightly faint comparing with that done PSF fitting. Especially, our measured faintest magnitude (18.7 mag) in aperture photometry is 0.1 mag fainter than that in PSF fitting. This indicates that we possibly overestimate the flux of the sky region around supernova. Since supernova locate near the galaxy, which would contaminate the sky region. Thus, as SN becomes faint, the relatively flux from host galaxy seems to increase. We also check that the comparison stars do not significantly varied the magnitude (figure 42).

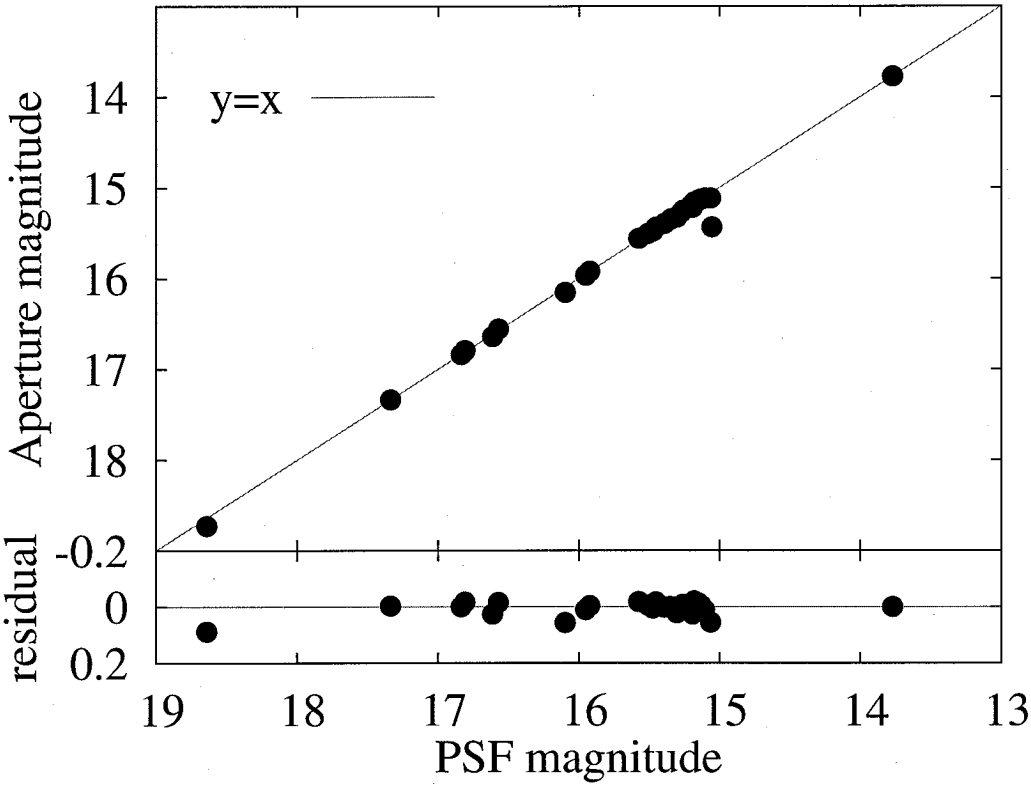

Figure 41: (Upper panel) Comparison of magnitudes measured by aperture photometry and PSF photometry. (Lower panel) The difference of both magnitudes is shown. They are consistent with each other for bright objects, but there is non-negligible difference for faint ones because of contamination of background components (e.g., faint nearby stars) in the aperture photometry.

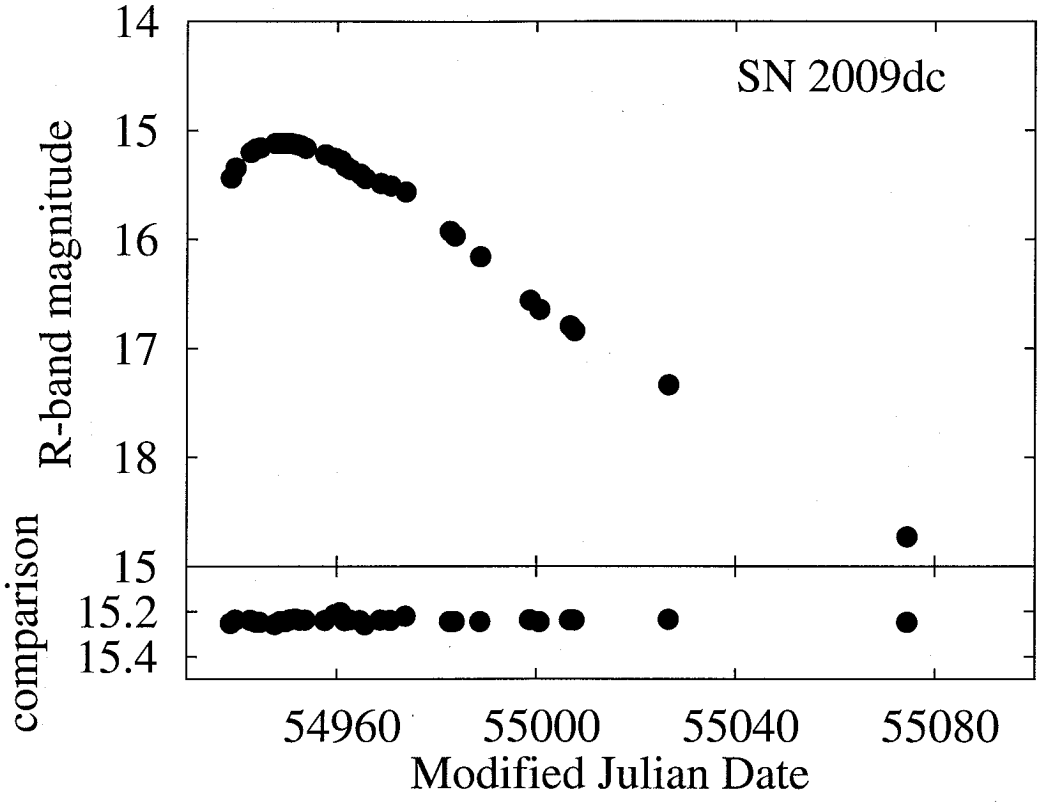

Figure 42: (Upper) Sample result of R-band light curve of an object measured relatively to a primary comparison star. (Lower) Magnitude of the primary comparison star derived relatively to a secondary comparison star. The constancy suggests these two comparison stars are not variable stars.

A. 3 Observational Logs of SN 2009dc

Table 5: Photometric data of SN 2009dc obtained by HOWPol

MJD	B	err_B	V	err_V	R_C	$\mathrm{err}_{R_\mathrm{C}}$	I_C	$\mathrm{err}_{I_\mathrm{C}}$
54938.80	15.793	0.003	15.465	0.011	15.434	0.011	15.549	0.018
54939.70	15.710	0.010	15.393	0.006	15.345	0.005	15.477	0.005
54942.70	15.549	0.017	15.254	0.012	15.200	0.006	15.350	0.015
54943.70	15.527	0.007	15.226	0.006	15.170	0.002	15.296	0.005
54944.60	15.525	0.018	15.213	0.005	15.157	0.011	15.291	0.010
54947.60	15.496	0.008	15.210	0.007	15.118	0.009	15.275	0.008
54948.70	15.508	0.006	15.214	0.001	15.116	0.004	15.263	0.005
54949.70	15.535	0.007	15.223	0.010	15.117	0.014	15.262	0.011
54950.70	15.555	0.007	15.237	0.004	15.118	0.003	15.269	0.007
54951.70	15.567	0.005	15.254	0.009	15.125	0.006	15.299	0.010
54952.60	15.618	0.007	15.280	0.003	15.137	0.012	15.282	0.007
54953.70	15.664	0.008	15.295	0.004	15.161	0.009	15.318	0.005
54957.60	15.845	0.006	15.377	0.001	15.219	0.018	15.346	0.009
54959.60	15.967	0.022	15.430	0.024	15.252	0.016	15.378	0.011
54960.70	15.985	0.009	15.448	0.012	15.274	0.018	15.406	0.010
54961.60	16.142	0.008	15.512	0.006	15.328	0.012	15.395	0.011
54962.60	16.195	0.005	15.546	0.006	15.354	0.007	15.420	0.014
54964.60	16.341	0.015	15.627	0.012	15.398	0.010	15.419	0.005
54965.60	16.430	0.005	15.669	0.007	15.438	0.006	15.418	0.008
54968.70	16.689	0.040	15.792	0.015	15.482	0.008	15.453	0.026
54970.70	16.826	0.045	15.845	0.009	15.506	0.010	15.423	0.008
54973.70	− − −	− − −	15.890	0.078	15.560	0.014	15.424	0.007
54982.60	17.630	0.024	16.355	0.014	15.923	0.006	15.628	0.011
54983.60	17.670	0.036	16.346	0.020	15.966	0.010	15.632	0.032
54988.70	− − −	− − −	16.594	0.036	16.156	0.020	15.898	− − −
54998.70	18.084	0.012	16.867	0.012	16.559	0.009	16.221	0.009
55000.60	18.128	0.023	16.909	0.008	16.642	0.011	16.274	0.010
55006.70	18.207	0.009	17.045	0.007	16.794	0.009	16.517	0.033
55007.60	18.258	0.053	17.084	0.010	16.838	0.011	16.523	0.005
55026.50	18.485	0.139	17.406	0.018	17.336	0.017	17.083	0.048
55074.50	19.281	0.084	18.556	0.087	18.728	0.037	18.303	0.014
55330.30	24.297	0.118	24.170	0.068	25.185	0.195	23.454	0.052

Table 6: Near-infrared photometric data of SN 2009dc obtained by ISLE

MJD	J	err_J	H	err_H	K_s	$\mathrm{err}_{K_\mathrm{s}}$
54943.6	15.675	0.056	15.884	0.072	15.692	0.086
54944.8	15.614	0.087	15.899	0.084	15.795	0.090
54948.6	15.605	0.045	15.778	0.068	15.668	0.082
54953.8	15.622	0.117	– – –	– – –	– – –	– – –
54960.5	15.912	0.047	15.747	0.066	15.555	0.081
54962.5	15.947	0.041	15.687	0.059	15.496	0.067
54990.5	16.246	0.186	– – –	– – –	– – –	– – –

Acknowledgments

I would like to deeply be grateful to Koji Kawabata, who is my adviser. He carefully taught me a lot about the basis of astronomical observations, logically reasonable thinking, grammer and idiom of English and so many on. Thanks to his very careful advise, I successfully finished writing this thesis.

I am grateful to Makoto Uemura. He taught me a lot of interesting astronomical phenomena of variable stars. He also taught importance of observations using small size telescope. I thank Michitoshi Yoshida. He gave me so many useful and helpful comments for this thesis. Thank to his many straight comments, I successfully improve my studies. I am grateful to Takashi Ohsugi for the guidance of my doctoral course in Hiroshima University. He gave me very good research environment. I also thank to Yashushi Fukazawa, Tsunefumi Mizuno, HIideaki Katagiri and Hiromitsu Takahashi. They gave me many helpful comments for my presentation in colloquium.

I deeply thank Masaomi Tanaka, who is one of collaborators. He taught me the basic physics, theoretical and observational studies of supernovae. His working style encourages and affects me well. I'm always looking forward to tell me about his insights to recent study. I thank Keiichi Maeda. He taught me physics of supernovae from theoretical aspects. His advise was very impressive for me and simple to understand. I thank Kenzo Kinugasa for spectropscopy of supernovae using 1.5-m telescope. His data plays a critical role for my thesis. I thank to Akira Imada, one of the collaborators. He performed the observations as prompt action since my sending e-mail.

I thank to Akira Arai, who is my senior. Since I was belong to Osaka Kyoiku University, he taught me many things of observation and study. We also discuss about the many things together more than astronomy. I thank to Osamu Nagae, Hiroyuki Tanaka and Tomoyuki Komatsu for development of HOWPol, which is a very effective instrument for supernovae observation. I thank to Mahito Sasada, Yuki Ikejiri, Kiyoshi Sakimoto, Ryosuke Itoh and Takako Okushima for observations on every night with me. I had a lot of fun with them at Higashi Hiroshima Observatory. I also thank to my many associates, who are students in High Energy Astrophysics groups. I had a very good times with them together despite of my short spending period in this laboratory since doctral course. Thank to them, I always relax to spend in this labolaratory and concentrate on my study.

Finally, I would like to grateful to my parents for their greatful supports about my daily life in Hiroshima. Without their helps, I would be not able to continue the study life until today.

Spectral data of comparison SNe are downloaded from the supernova spectra database SUSPECT (http://suspect.nhn.ou.edu/ suspect/).

References

Altavilla, G., et al. 2004, MNRAS, 349, 1344

Anupama, G. C., Sahu, D. K., & Jose, J. 2005, A&A, 429, 667

Arnett, W. D. 1969, ApJ, 157, 1369

—. 1982, ApJ, 253, 785

Astier, P., et al. 2006, A&A, 447, 31

Benetti, S., et al. 2004, MNRAS, 348, 261

—. 2005, ApJ, 623, 1011

Benz, W., Cameron, A. G. W., Press, W. H., & Bowers, R. L. 1990, ApJ, 348, 647

Bessell, M. S. 1990, PASP, 102, 1181

Blondin, S., et al. 2006, AJ, 131, 1648

Bongard, S., Baron, E., Smadja, G., Branch, D., & Hauschildt, P. H. 2006, ApJ, 647, 513

Branch, D., Fisher, A., & Nugent, P. 1993, AJ, 106, 2383

Branch, D., Lacy, C. H., McCall, M. L., Sutherland, P. G., Uomoto, A., Wheeler, J. C., & Wills, B. J. 1983, ApJ, 270, 123

Branch, D., et al. 2006, PASP, 118, 560

Bravo, E., & García-Senz, D. 2008, A&A, 478, 843

Cappellaro, E., Mazzali, P. A., Benetti, S., Danziger, I. J., Turatto, M., della Valle, M., & Patat, F. 1997, A&A, 328, 203

Cardelli, J. A., Clayton, G. C., & Mathis, J. S. 1989, ApJ, 345, 245

Chandrasekhar, S. 1931, ApJ, 74, 81

Chiyonobu, S. 2004, master thesis in Hiroshima University (in Japanese)

Chronological Scientific Tables 2004. 2003, Atmospheric Extinction, ed. NAOJ., Maruzen Co Ltd.,, 153

Colgate, S. A., & McKee, C. 1969, ApJ, 157, 623

Conley, A., et al. 2006, AJ, 132, 1707

Di Carlo, E., et al. 2008, ApJ, 684, 471

Elias-Rosa, N., et al. 2006, MNRAS, 369, 1880

Falco, E. E., et al. 1999, PASP, 111, 438

Filippenko, A. V. 1997, ARA&A, 35, 309

Filippenko, A. V., et al. 1992a, ApJ, 384, L15

—. 1992b, AJ, 104, 1543

Folatelli, G., et al. 2010, AJ, 139, 120

Foley, R. J., Brown, P. J., Rest, A., Challis, P. J., Kirshner, R. P., & Wood-Vasey, W. M. 2010, ApJ, 708, L61

Foley, R. J., et al. 2009, AJ, 138, 376

Freedman, W. L., et al. 2001, ApJ, 553, 47

Gerardy, C. L., et al. 2004, ApJ, 607, 391

—. 2007, ApJ, 661, 995

Gilfanov, M., & Bogdán, Á. 2010, Nature, 463, 924

Guy, J., et al. 2007, A&A, 466, 11

Hachinger, S., Mazzali, P. A., & Benetti, S. 2006, MNRAS, 370, 299

Hachisu, I., Kato, M., & Nomoto, K. 2010, ApJ, 724, L212

Harutyunyan, A., Elias-Rosa, N., & Benetti, S. 2009, Central Bureau Electronic Telegrams, 1768, 1

Hatano, K., Branch, D., Lentz, E. J., Baron, E., Filippenko, A. V., & Garnavich, P. M. 2000, ApJ, 543, L49

Hicken, M., Garnavich, P. M., Prieto, J. L., Blondin, S., DePoy, D. L., Kirshner, R. P., & Parrent, J. 2007, ApJ, 669, L17

Hillebrandt, W., & Niemeyer, J. C. 2000, ARA&A, 38, 191

Howell, D. A. 2010, ArXiv e-prints

Howell, D. A., et al. 2006, Nature, 443, 308

Hunter, D. J., et al. 2009, A&A, 508, 371

Iben, Jr., I., & Tutukov, A. V. 1984, ApJS, 54, 335

Jha, S., Riess, A. G., & Kirshner, R. P. 2007, ApJ, 659, 122

Junde, H., Dailing, H., Chunmei, Z., Xiaoling, H., Baohua, H., & Yaodong, W. 1987, Nuclear Data Sheets, 51, 1

Kamiya, M., et al. 2010, in preparation

Kasen, D. 2006, ApJ, 649, 939

Kasen, D., Röpke, F. K., & Woosley, S. E. 2009, Nature, 460, 869

Kashikawa, N., et al. 2002, PASJ, 54, 819

Kawabata, K. S., et al. 2008, in Presented at the Society of Photo-Optical Instrumentation Engineers (SPIE) Conference, Vol. 7014, Society of Photo-Optical Instrumentation Engineers (SPIE) Conference Series

Khokhlov, A. M. 1991, A&A, 245, 114

Kinugasa, K., et al. 2002, ApJ, 577, L97

Komatsu, E., et al. 2010, ArXiv e-prints

Kotak, R., et al. 2005, A&A, 436, 1021

Krisciunas, K., Phillips, M. M., & Suntzeff, N. B. 2004, ApJ, 602, L81

Krisciunas, K., Prieto, J. L., Garnavich, P. M., Riley, J., Rest, A., Stubbs, C., & McMillan, R. 2006, AJ, 131, 1639

Krisciunas, K., et al. 2007, AJ, 133, 58

Landolt, A. U. 1992, AJ, 104, 340

Leloudas, G., et al. 2009, A&A, 505, 265

Li, W., Filippenko, A. V., Treffers, R. R., Riess, A. G., Hu, J., & Qiu, Y. 2001, ApJ, 546, 734

Li, W., et al. 2003, PASP, 115, 453

—. 2010, ArXiv e-prints

Lira, P., et al. 1998, AJ, 115, 234

Maeda, K., Kawabata, K., Li, W., Tanaka, M., Mazzali, P. A., Hattori, T., Nomoto, K., & Filippenko, A. V. 2009, ApJ, 690, 1745

Maeda, K., Mazzali, P. A., Deng, J., Nomoto, K., Yoshii, Y., Tomita, H., & Kobayashi, Y. 2003, ApJ, 593, 931

Maeda, K., Röpke, F. K., Fink, M., Hillebrandt, W., Travaglio, C., & Thielemann, F. 2010a, ApJ, 712, 624

Maeda, K., Taubenberger, S., Sollerman, J., Mazzali, P. A., Leloudas, G., Nomoto, K., & Motohara, K. 2010b, ApJ, 708, 1703

Maeda, K., et al. 2010c, Nature, 466, 82

Mazzali, P. A., Benetti, S., Stehle, M., Branch, D., Deng, J., Maeda, K., Nomoto, K., & Hamuy, M. 2005a, MNRAS, 357, 200

Mazzali, P. A., Cappellaro, E., Danziger, I. J., Turatto, M., & Benetti, S. 1998, ApJ, 499, L49+

Mazzali, P. A., Röpke, F. K., Benetti, S., & Hillebrandt, W. 2007, Science, 315, 825

Mazzali, P. A., Sauer, D. N., Pastorello, A., Benetti, S., & Hillebrandt, W. 2008, MNRAS, 386, 1897

Mazzali, P. A., et al. 2005b, ApJ, 623, L37

Milne, P. A., The, L., & Leising, M. D. 1999, ApJS, 124, 503

Motohara, K., et al. 2006, ApJ, 652, L101

Nomoto, K. 1982, ApJ, 253, 798

Nomoto, K., Thielemann, F., & Yokoi, K. 1984, ApJ, 286, 644

Nozawa, T., et al. 2008, ApJ, 684, 1343

Nugent, P., Phillips, M., Baron, E., Branch, D., & Hauschildt, P. 1995, ApJ, 455, L147+

Pagel, B. E. J. 1997, Nucleosynthesis and Chemical Evolution of Galaxies, ed. Pagel, B. E. J.

Pakmor, R., Kromer, M., Röpke, F. K., Sim, S. A., Ruiter, A. J., & Hillebrandt, W. 2010, Nature, 463, 61

Pastorello, A., et al. 2007, MNRAS, 377, 1531

Patat, F., Benetti, S., Cappellaro, E., Danziger, I. J., della Valle, M., Mazzali, P. A., & Turatto, M. 1996, MNRAS, 278, 111

Perlmutter, S., et al. 1999, ApJ, 517, 565

Pfannes, J. M. M., Niemeyer, J. C., & Schmidt, W. 2010, A&A, 509, A75+

Phillips, M. M. 1993, ApJ, 413, L105

Phillips, M. M., Lira, P., Suntzeff, N. B., Schommer, R. A., Hamuy, M., & Maza, J. 1999, AJ, 118, 1766

Phillips, M. M., et al. 2007, PASP, 119, 360

Pignata, G., et al. 2008, MNRAS, 388, 971

Prieto, J. L., Rest, A., & Suntzeff, N. B. 2006, ApJ, 647, 501

Puckett, T., Moore, R., Newton, J., & Orff, T. 2009, Central Bureau Electronic Telegrams, 1762, 1

Reindl, B., Tammann, G. A., Sandage, A., & Saha, A. 2005, ApJ, 624, 532

Riess, A. G., et al. 1998, AJ, 116, 1009

Ruiz-Lapuente, P., & Spruit, H. C. 1998, ApJ, 500, 360

Sahu, D. K., et al. 2008, ApJ, 680, 580

Saio, H., & Nomoto, K. 1985, A&A, 150, L21

Salvo, M. E., Cappellaro, E., Mazzali, P. A., Benetti, S., Danziger, I. J., Patat, F., & Turatto, M. 2001, MNRAS, 321, 254

Scalzo, R. A., et al. 2010, ApJ, 713, 1073

Schlegel, D. J., Finkbeiner, D. P., & Davis, M. 1998, ApJ, 500, 525

Silverman, J. M., Ganeshalingam, M., Li, W., Filippenko, A. V., Miller, A. A., & Poznanski, D. 2010, MNRAS, 1381

Sollerman, J., et al. 2004, A&A, 428, 555

Stanishev, V., et al. 2007, A&A, 469, 645

Stehle, M., Mazzali, P. A., Benetti, S., & Hillebrandt, W. 2005, MNRAS, 360, 1231

Stetson, P. B. 1987, PASP, 99, 191

Stritzinger, M., & Sollerman, J. 2007, A&A, 470, L1

Tanaka, M., Mazzali, P. A., Maeda, K., & Nomoto, K. 2006, ApJ, 645, 470

Tanaka, M., Mazzali, P. A., Stanishev, V., Maurer, I., Kerzendorf, W. E., & Nomoto, K. 2010a, MNRAS, 1494

Tanaka, M., et al. 2008, ApJ, 677, 448

—. 2010b, ApJ, 714, 1209

Taubenberger, S., et al. 2010, ArXiv e-prints

Thomas, R. C., et al. 2007, ApJ, 654, L53

Truran, J. W., Arnett, W. D., & Cameron, A. G. W. 1967, Canadian Journal of Physics, 45, 2315

Turatto, M., Benetti, S., & Cappellaro, E. 2003, in From Twilight to Highlight: The Physics of Supernovae, ed. W. Hillebrandt & B. Leibundgut, 200–+

Uemura, M., et al. 2007, in American Institute of Physics Conference Series, Vol. 921, The First GLAST Symposium, ed. S. Ritz, P. Michelson, & C. A. Meegan, 205–207

Uenishi, T., Nomoto, K., & Hachisu, I. 2003, ApJ, 595, 1094

Valenti, S., et al. 2008, ApJ, 673, L155

—. 2009, Nature, 459, 674

van den Heuvel, E. P. J., Bhattacharya, D., Nomoto, K., & Rappaport, S. A. 1992, A&A, 262, 97

Wang, X., Wang, L., Pain, R., Zhou, X., & Li, Z. 2006, ApJ, 645, 488

Wang, X., et al. 2008, ApJ, 675, 626

—. 2009, ApJ, 697, 380

Webbink, R. F. 1984, ApJ, 277, 355

Whelan, J., & Iben, Jr., I. 1973, ApJ, 186, 1007

Wood-Vasey, W. M., et al. 2007, ApJ, 666, 694

Woosley, S. E., & Weaver, T. A. 1986, ARA&A, 24, 205

Yamanaka, M., et al. 2009a, ApJ, 707, L118

—. 2009b, PASJ, 61, 713

Yanagisawa, K., et al. 2006, in Presented at the Society of Photo-Optical Instrumentation Engineers (SPIE) Conference, Vol. 6269, Society of Photo-Optical Instrumentation Engineers (SPIE) Conference Series

Yoon, S., & Langer, N. 2003, A&A, 412, L53

—. 2005, A&A, 435, 967

Yuan, F., et al. 2010, ApJ, 715, 1338